



UNIVERSIDAD DE CONCEPCIÓN  
FACULTAD DE CIENCIAS FÍSICAS Y MATEMÁTICAS  
MAGÍSTER EN ASTRONOMÍA

---

## **Magnetic Activity in Fully Convective M Dwarf Stars**

*Its possible influence on binary systems*

## **Campos Magnéticos en Estrellas Enanas M**

*Su posible influencia en sistemas binarios*

**Profesor Guía: Dr. Dominik Schleicher**

Departamento de Astronomía  
Facultad de Ciencias Físicas y Matemáticas  
Universidad de Concepción

**Tesis para ser presentada a la Dirección de Postgrado de la Universidad  
de Concepción para optar al grado de Magíster en Astronomía**

---

**CAROLINA ANGÉLICA ORTIZ RODRÍGUEZ**  
MAYO DE 2022  
CONCEPCIÓN, CHILE





©2022, Carolina Ortiz Rodríguez

Se autoriza la reproducción total o parcial, con fines académicos, por cualquier medio o procedimiento, incluyendo la cita bibliográfica del documento.

## Acknowledgements

This project would not have been possible without the support of many people.

First and foremost, I thank my parents, Angélica and Claudio, who have always supported me in every step I have made. I thank my sister Claudia for always encouraging me to pursue my academic aspirations, as well as my younger brother for always being there for me. I would like to express my gratitude to my partner, Mauro, for his patience and unwavering support. A very special thanks to the friends I have made over the years as an undergraduate and graduate student.

Dr. Dominik Schleicher, my supervisor, deserves my sincerest gratitude for his advice, encouragement, and his insightful comments. I would like to express my gratitude to Dr. Petri Käpylä for providing the setup which I worked on my thesis, for making numerous helpful ideas for the project, and for sharing his knowledge. I owe a sincere gratitude to Felipe Navarrete, who helped me since the beginning with the project, to solve code problems and for the fruitful discussions.

Financial support from FONDECYT (project code 1201280) and ANID BASAL project ACE210002 is acknowledged. Part of the simulations were performed using the KULTRUN cluster at the Astronomy Department of the Universidad de Concepción. This thesis was partially supported by the compute time in The North-German Supercomputing Alliance (HLRN).

## Resumen

Los campos magnéticos son omnipresentes en el Universo. Así como el Sol, otras estrellas también tienen fuertes campos magnéticos. Las estrellas enanas M son completamente convectivas con masas inferiores a 0.35 masas solares. Estas estrellas son de interés primordial en la comunidad de investigación del dínano estelar, ya que el funcionamiento de sus campos magnéticos no son completamente entendidos y su estructura interna es diferente a la del Sol porque no tienen zona radiativa, entonces, permiten probar si esto tiene un impacto significativo para el dínamo. En esta tesis, utilicé simulaciones magneto-hidrodinámicas en tres dimensiones para estudiar los campos magnéticos a gran escala de estrellas completamente convectivas en función del número magnético de Prandtl, un parámetro adimensional que describe la relación entre la viscosidad y la resistividad. Estas simulaciones se realizaron con diferentes períodos de rotación en el régimen de rotación lento a intermedio, con períodos de rotación de 43 a 90 días. Encontré diferentes soluciones para el campo magnético a gran escala, ciclos cuasi-periódicos similares a los del Sol, e inversiones irregulares también. Este estudio ha ampliado de manera muy significativa el rango de parámetros investigado para las estrellas enanas M, con número magnético de Prandtl que va desde 0.1 hasta 10.

Las enanas M se encuentran usualmente en binarias con post envoltura comun (PCEBs), que muestran variaciones en sus tiempos de eclipse (ETVs). La viabilidad de que el campo magnético afecte al sistema binario se explora en el contexto del modelo de Applegate. Sin embargo, la tasa de rotación utilizada aquí no es realista para apuntar a tales sistemas. Las enanas M en PCEBs tienen periodos de rotación que van desde horas hasta unos pocos días. El próximo paso obvio será investigar este proceso utilizando simulaciones con tasas de rotación más rápida.

**Keywords** – Campos magnéticos estelares, Enanas M, Número magnético de Prandtl, Post-Common Envelope Binaries.

## Abstract

Magnetic fields are ubiquitous in the universe. As the Sun, other stars also have strong magnetic fields. M dwarf stars are fully convective when having masses below 0.35 solar masses. These stars are of prime interest in the stellar dynamo community, since their magnetic fields are not yet fully understood and they are quite different than the Sun because they do not have a radiative zone, so they allow to probe if this makes a significant difference for the dynamo. In this thesis, using three-dimensional magneto-hydrodynamical simulations I studied the large-scale magnetic structures of fully convective M dwarf stars as a function of the magnetic Prandtl number; an important dimensionless parameter describing the ratio of viscosity and resistivity. These simulations were performed at different rotation periods in the slowly to intermediate rotation regime, with rotation periods from 43 to 90 days. I have found different solutions for the large-scale magnetic field, quasi-periodic cycles similar to those of the Sun, and irregular reversals as well. This study overall has very significantly extended the parameter space probed for M-dwarf stars, with magnetic Prandtl numbers from 0.1 to 10.

M dwarfs are usually found in Post Common Envelope Binaries (PCEBs), which commonly show Eclipsing Time Variations (ETVs). The feasibility of the magnetic field affecting the binary system is explored in the context of the Applegate model. However, the rotation rate used here is not realistic for targeting such systems. M dwarfs in PCEBs have rotation periods that range from hours to a few days. I believe that a logical next step will be to probe this mechanism with rapidly rotating simulations.

*Keywords* – Stellar magnetic fields, M dwarf stars, Magnetic Prandtl number, Post-Common Envelope Binaries

# Contents

<b>ACKNOWLEDGEMENTS</b>	<b>i</b>
<b>Resumen</b>	<b>ii</b>
<b>Abstract</b>	<b>iii</b>
<b>1 Introduction</b>	<b>1</b>
1.1 Context	1
1.2 Previous works with simulations	2
1.3 This work	3
1.3.1 Magnetism in intermediate to slowly rotating M dwarfs	3
1.3.2 Influence of large-scale magnetic fields on binary systems	4
<b>2 Magnetic fields</b>	<b>6</b>
2.1 Stellar magnetism	6
2.1.1 The Sun	7
2.1.2 M dwarf stars	9
2.2 Magneto-hydrodynamics	10
2.2.1 Dimensionless parameters	11
2.2.2 Convection	12
2.2.3 Mixing length theory	12
2.3 Dynamo mechanism	13
2.3.1 Solar dynamo	13
$\Omega$ effect	13
$\alpha$ effect	14
Flux transport dynamos	15
Mean-field dynamo theory	15
2.4 Flow properties	17
2.4.1 Differential rotation	17
2.4.2 Meridional circulation	18
2.4.3 Kinetic helicity	18
<b>3 Computational methods</b>	<b>20</b>
3.1 MESA	20
3.1.1 Files to set in the run directory	20
3.1.2 Output files	21
3.1.3 Structure and composition equations	21

3.2	The Pencil code . . . . .	22
3.2.1	Starting . . . . .	22
3.2.2	Modularity . . . . .	25
3.2.3	Output files . . . . .	26
3.3	The star-in-a-box model with the Pencil Code . . . . .	27
3.3.1	Control parameters and physical units . . . . .	29
<b>4</b>	<b>Three-dimensional MHD simulations with varying magnetic Prandtl number and rotation period</b>	<b>32</b>
4.1	Simulations . . . . .	32
4.2	Results . . . . .	34
4.2.1	Large-scale magnetic fields at different $Pr_M$ . . . . .	34
4.2.1.1	Toroidal magnetic field . . . . .	36
4.2.1.2	Large-scale magnetic fields at different $P_{rot}$ . . . . .	41
4.2.1.3	The magnetic field at different stellar radii (depth) . . . . .	45
4.2.1.4	Radial magnetic field . . . . .	46
4.2.1.5	The Proxima Centauri case . . . . .	46
4.2.2	Large scale flows . . . . .	50
4.2.3	Energies as function of $Pr_M$ . . . . .	56
4.2.4	Spherical harmonic decomposition . . . . .	61
<b>5</b>	<b>Possible impact of large scale magnetic field on binary systems</b>	<b>64</b>
5.1	Eclipsing Time Variations . . . . .	64
5.2	The Applegate mechanism . . . . .	65
5.2.1	Quadrupole moment . . . . .	67
5.2.1.1	Evolution of $Q_{xx}$ . . . . .	68
5.2.2	Period variations and O - C . . . . .	75
5.2.3	Comparison to a real system: HU Aquarii . . . . .	76
<b>6</b>	<b>Summary and discussion</b>	<b>78</b>
	<b>Bibliography</b>	<b>82</b>

## List of Tables

4.1.1	Summary of the simulations. . . . .	35
4.2.1	Complementary table . . . . .	38
4.2.2	Amplitude of the temporally and azimuthally averaged angular velocity $\overline{\Omega}(r, \theta)$ . . . . .	51
4.2.3	Energy densities measured for each simulation . . . . .	58
4.2.4	Table that indicates the total magnetic energy density $E_{\text{mag}}^{\text{tot}}$ in $10^5 \text{ J m}^{-3}$ . The magnetic energy density of the modes $m = 0, 1, 2$ , and the magnetic energy density considering $l, m > 10$ . . . . .	63
5.2.1	The amplitude of the variations of $Q_{xx}$ and the correlation coefficient between $Q_{xx}$ and $E_{\text{mag}}$ . . . . .	75
5.2.2	Variation of the orbital period during a cycle of the binary for the different binary periods $a_1 = 0.6$ , $a_2 = 0.8$ , $a_3 = 1.4$ and $a_1 = 1.7 R_{\odot}$ . . . . .	76
5.2.3	The modulation period $P_{\text{mod}}$ (in years), and the O - C values (in seconds) for $a_1 = 0.6$ , $a_2 = 0.8$ , $a_3 = 1.4$ and $a_1 = 1.7$ , in unit of the solar radius, $R_{\odot}$ . . . . .	76

# List of Figures

2.1.1	Internal structures of main-sequence stars. . . . .	7
2.1.2	Sunspot image taken on January 28, 2020 by DKIST. Credit: NSO/NSF/AURA. . . . .	8
2.1.3	Longitudinally averaged magnetic field at the surface of the Sun for the four last sunspots cycles. . . . .	9
2.3.1	Schematic representation of the solar differential rotation and the $\Omega$ effect . . . . .	14
2.4.1	Rotation rate of the Sun at different latitudes as a function of depth. . . . .	19
4.2.1	Time evolution of volume averaged rms magnetic field of simulations A5, A13 and A15. . . . .	36
4.2.2	Time evolution of the azimuthally averaged toroidal magnetic field $\bar{B}_\phi$ near the surface of the star for simulations A1-A5. The colorbar is cut at $\pm 8$ kG. Figure for simulation A3 is presented as simulation A2 in Ortiz-Rodríguez et al. Submitted . . . . .	39
4.2.3	Time evolution of the azimuthally averaged toroidal magnetic field $\bar{B}_\phi$ near the surface of the star for simulations A6-A11. The colorbar is cut at $\pm 8$ kG. . . . .	40
4.2.4	Time evolution of the azimuthally averaged toroidal magnetic field $\bar{B}_\phi$ near the surface of the star for simulations A13-A16. The colorbar is cut at $\pm 8$ kG. Figure for simulation A16 is presented as simulation A8 in Ortiz-Rodríguez et al. Submitted. . . . .	41
4.2.5	Time evolution of the azimuthally averaged toroidal magnetic field $\bar{B}_\phi$ near the surface of the star for simulations B1-B5. The colorbar is cut at $\pm 8$ kG. . . . .	43
4.2.6	Time evolution of the azimuthally averaged toroidal magnetic field $\bar{B}_\phi$ near the surface of the star for simulations C1-C6. The colorbar is cut at $\pm 8$ kG. . . . .	44
4.2.7	Time evolution of the azimuthally averaged toroidal magnetic field at different depths. . . . .	45
4.2.8	Mollweide projection of the radial magnetic field at the surface for simulations of set A, A4, A14 and A16, with 43 days of rotation period. . . . .	47
4.2.9	Mollweide projection of the radial magnetic field at the surface for simulations of set B, B1, B4 and B5, with 61 days of rotation period. . . . .	48

4.2.10	Mollweide projection of the radial magnetic field at the surface for simulations of set C, C3, C5 and C6, with 90 days of rotation period. . . . .	49
4.2.11	Temporally and azimuthally averaged angular velocity $\overline{\Omega}(\varphi, z)$ for simulations A1, A13, A14 and A16. . . . .	53
4.2.12	Temporally and azimuthally averaged angular velocity $\overline{\Omega}(\varphi, z)$ for simulations A8 and C2. . . . .	54
4.2.13	Azimuthally averaged normalised kinetic helicity $\tilde{\mathcal{H}} = \mathcal{H}(\varphi, z)/u_{\text{rms}}\omega_{\text{rms}}$ for simulations A13 (top left), B3 (top right) and C4 (bottom). . . . .	55
4.2.14	Time evolution of the kinetic and magnetic energy densities in the kinematic regime. . . . .	59
4.2.15	Time evolution of the kinetic and magnetic energy densities in the saturated regime. . . . .	60
4.2.16	Radial magnetic field near the surface of the star reconstructed via spherical harmonic decomposition and real data. . . . .	63
5.1.1	Common envelope phase illustration . . . . .	65
5.2.1	Scatter plot of $\Delta Q_{xx}$ as a function of the magnetic Prandtl number. . . . .	70
5.2.2	Scatter plot of $\Delta Q_{xx}$ as a function of the toroidal magnetic energy density. . . . .	70
5.2.3	Scatter plot of $\Delta Q_{xx}$ as a function of the poloidal magnetic energy density. . . . .	71
5.2.4	Time evolution of $Q_{xx}$ together with $E_{\text{mag}}$ for simulations A4, A14 and A16. . . . .	72
5.2.5	Time evolution of $Q_{xx}$ together with $E_{\text{mag}}$ for simulations B1, B4 and B5. . . . .	73
5.2.6	Time evolution of $Q_{xx}$ together with $E_{\text{mag}}$ for simulations C3, C5 and C6. . . . .	74

# Chapter 1

## Introduction

### 1.1 Context

Starspots are the most visible manifestations of magnetic fields in the outermost layers of stars. In the case of the Sun, the sunspots have an 11-year cycle and it takes twice as long for the polarity of the spots to revert to the same. Today it is known that all solar activity is caused by an underlying magnetic field. The mechanism responsible for generating and sustaining magnetic fields in late-type stars is a self-excited dynamo (Brandenburg and Subramanian, 2005; Charbonneau, 2013, 2020). In the case of the Sun, it sustains the large-scale magnetic field by converting the poloidal magnetic field into a toroidal magnetic field primarily by shearing of the field lines via differential rotation. The physical mechanism by which the poloidal field is regenerated remains unclear. A proposed mechanism is from helical convective motions ( $\alpha$ -effect) (Parker, 1955; Steenbeck et al., 1966). Additionally, some dynamo models assume a high importance of the tachocline (Spiegel and Zahn, 1992), which is the shear layer between the radiative core and the convection zone in solar-like stars.

In the present day, stars different from the Sun are known for exhibiting surface activity (Baliunas et al., 1995). Typical examples are the late-type M dwarfs (Kochukhov, 2021), which are low-mass main-sequence stars and the most numerous type of star in the solar neighbourhood. These stars are of prime interest for the dynamo scientific community, since M dwarfs with masses up

to  $0.35 M_{\odot}$  are fully convective and do not possess a tachocline, and at the same time show large-scale magnetic fields. For instance, Proxima Centauri is a known fully convective star with an activity cycle of 7 years (Klein et al., 2021).

The investigation of magnetic fields of M dwarfs is not only a matter of interest for the dynamo scientific community, but also for the search of exoplanets orbiting M dwarf stars. Since magnetic fields may interfere with the detection of exoplanets because of the presence of large-scale structures, it is crucial to distinguish them from signatures of planets. Further, magnetic fields of M dwarfs can impact planets that orbit the habitable zone (Andersen and Korhonen, 2015).

## 1.2 Previous works with simulations

Three-dimensional numerical simulations of stars are performed with the aim of achieving a better understanding of their magnetic fields, dynamos, and convection as a function of stellar parameters (mass, age, rotation) and dimensionless numbers, e.g., the magnetic Prandtl number, that describe the physics in the stellar interiors. Some authors have performed numerical simulations of fully convective stars in spherical shells. For instance, Browning (2008) modeled a  $0.3M_{\odot}$  star with a domain extending from 0.08 to 0.96 times the stellar radius, finding that the star can generate magnetic field strengths of the order of kG. Gastine, T. et al. (2013) focused on the importance of the Rossby number, which is a measure of the influence of the Coriolis force on convective flows, for large-scale dynamos of M dwarfs with models in spherical shells. Brown et al. (2020) performed simulations of fully convective M dwarfs in spherical coordinates, finding a hemispherical dynamo solution for every computed case. Most recently, Käpylä (2021) presented an updated version of the “star-in-a-box” model in Cartesian coordinates of fully convective stars, which was first presented by Dobler et al. (2006). In that work, Käpylä (2021) presented simulations with and without magnetic fields, varying the rotation rate of the star, considering rotation periods ranging from 4.3 to 433 days, finding different solutions for the large-scale magnetic field and the differential rotation of the star. For slow rotation, predominantly axisymmetric large-scale magnetic fields were obtained. For intermediate rotation, large-scale

magnetic fields are predominantly axisymmetric and cyclic. For rapid rotation, large scale magnetic fields are mostly non-axisymmetric and the models show azimuthal dynamo waves (Cole et al., 2013).

## 1.3 This work

This thesis presents three-dimensional magneto-hydrodynamic simulations of fully convective stars using the “star-in-a-box” model (Käpylä, 2021). This model is described by the non-ideal equations of magneto-hydrodynamics that are solved with the Pencil Code (Pencil Code Collaboration et al., 2021). Using a cartesian box is beneficial because it includes the whole star, and the areas outside the star may be viewed as free boundaries for magnetic fields and flows, which can be advantageous when compared to spherical shell models.

### 1.3.1 Magnetism in intermediate to slowly rotating M dwarfs

The focus of this thesis is to explore the large-scale magnetic field solutions and flow properties of a fully convective M dwarf star with intermediate rotation periods of 43, 61 and 90 days, the last being the rotation period of the fully convective M dwarf, Proxima Centauri, a nearby star that exhibits an activity cycle of 7 years (Klein et al., 2021). In addition to varying the rotation period, we varied the magnetic Prandtl number,  $Pr_M$ , with values ranging from 0.1 to 10, which is a wide range for this type of simulations.  $Pr_M$  is an intrinsic property of the fluid defined as the ratio of viscosity to magnetic diffusivity, and it is a crucial ingredient for dynamos. Dynamos in stars with low  $Pr_M$  and large  $Pr_M$  have very different properties, and the effect on the dynamo has been shown for simulations of spherical shells by Käpylä et al. (2017). While here we pursue such a study for the first time modeling the star in full. The stellar parameters used here are the typical values for an M5 star and verified using simulations with Modules for Experiments in Stellar Astrophysics (MESA) (Paxton et al., 2010).

In addition to the large-scale dynamo, the feasibility of small-scale dynamo operation is also examined in the simulations presented here.

### 1.3.2 Influence of large-scale magnetic fields on binary systems

Close binaries like Post-Common-Envelope-Binaries (PCEBs) show eclipsing time variations (ETVs) in their O - C (observed minus calculated) diagram. PCEBs consist of a magnetically active main-sequence star, like an M dwarf and a White Dwarf. [Zorotovic and Schreiber \(2013\)](#) have found that  $\sim 90\%$  of the PCEBs show eclipsing time variations. These variations can be explained by the presence of a third body, like a planet, or due to the magnetic activity of one of the stars. This is possible due the Applegate mechanism ([Applegate, 1992](#)), where a time-dependent gravitational quadrupole moment (i.e., related to the shape of the star) is modulated by the stellar magnetic activity, and this in turn produces changes on the binary separation that can be noted in the O - C diagram. Low-mass post-common-envelope binaries with secondary masses of  $0.30$  to  $0.33 M_{\odot}$  are found to be the most promising candidates for the Applegate mechanism ([Völschow et al., 2018](#)). [Navarrete et al. \(2018\)](#) explored the feasibility of this mechanism under the framework presented by [Völschow et al. \(2016\)](#), suggesting that rotation plays an important role. Most recently, [Navarrete et al. \(2020\)](#) presented magneto-hydrodynamical simulations of spherical shells with different rotation rates, finding that for slow rotation, the quadrupole moment and magnetic field change in a quasi-periodic manner, while for rapid rotation, the quadrupole moment and magnetic field change in a more complex manner. Further, [Lanza \(2020\)](#) presented a model to explain the orbital period modulations in binary systems based on a permanent non-axisymmetric gravitational quadrupole moment, which is produced by a non-axisymmetric magnetic field.

An analysis of whether the changes of the quadrupole moment are important to influence the variation of periods of binary systems is also included in this thesis.

This thesis is presented as follows: an overview of stellar magnetic fields regarding the Sun and M dwarf stars is given in Chapter 2. Additionally, the most important concepts about magneto-hydrodynamics and dynamo mechanism are given, together with the flow properties which are important for large-scale magnetic fields. Chapter 3 presents the computational methods used, as well as the codes and model utilised to perform the simulations. In

Chapters 4 and 5 the results are given. The main conclusions and a discussion is presented in Chapter 6.



## Chapter 2

# Magnetic fields

This chapter provides an overview of stellar magnetic fields, including the most well-known, the Sun's magnetic field, as well as information on M dwarfs, the type of star covered in this thesis. An explanation of magneto-hydrodynamics and its equations, as well as an outline of the dynamo process, are given to comprehend how magnetic fields in stars evolve. Large-scale flows within stars are also discussed, which are important for large-scale magnetic fields.

### 2.1 Stellar magnetism

Stellar magnetism started to be a field of study when George Hale realised the magnetic origin of the sunspots a little more than a century ago, with measurements of Zeeman splitting in spectral lines in sunspots (Hale, 1908). However, he was not the first person to notice the spots; ancient records of observations of star spots in the Sun have existed long ago, such as those of Galileo Galilei in the early 16th century (Reeves et al., 2012) and even records dating back to 165 BC (Yau and Stephenson, 1988).

Magnetic fields have been observed in several types of stars along the Hertzsprung-Russel diagram, such as T Tauri stars from the pre-main-sequence, with authors reporting strengths of the order of kG (Johns-Krull et al., 1999; Johns-Krull, 2007). Solar-like (with radiative core and convective envelope) stars other than the Sun were also found to host magnetic fields, see e.g. the magnetic activity cycles reported for several stars by Baliunas et al. (1995);

or the reconstructed large-scale magnetic field of the star HN Pegasi using Zeeman-Doppler imaging by [Boro Saikia, S. et al. \(2015\)](#). Furthermore, stars beyond the main-sequence have been found to present surface magnetic fields, as presented by [Sabin et al. \(2014\)](#) for the AGB stars U Monocerotis and R Scuti. In this section, I will provide an overview of the magnetic fields of the Sun, the first star discovered to have magnetic fields and also the most studied example up to this point, as well as a description of magnetic fields in M dwarf stars, which are the primary objects of this study.

### 2.1.1 The Sun

The Sun is a common star in its main-sequence stage, converting hydrogen to helium in its core. The Sun's interior structure is typically divided into three zones: the core, the radiative zone, which is hydrodynamically stable and reaches up to  $0.7R_{\odot}$ , and the outer envelope, which is known as the convection zone because it carries heat to the surface via fluid motions. Figure 2.1.1 is an illustration of the internal structure of the radiative and convective zone of main-sequence stars.

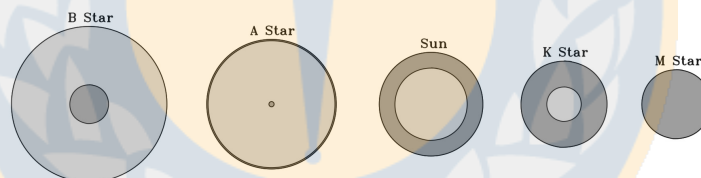


**Figure 2.1.1:** Internal structures of main-sequence stars. Dark gray color indicates convection zone while light gray indicates radiative zone. Sizes of stars are not to scale. Adapted from [Charbonneau \(2013\)](#).

The magnetic activity is one of the most researched characteristics of the Sun. As previously said, the most visible indication of the existence of magnetic fields on the surface of the Sun are the sunspots, which have been systematically recorded throughout the years. Sunspots, as the name implies, are darker spots in comparison to the surrounding areas because the darker areas have a lower temperature than the brighter ones. This temperature contrast is caused by the presence of strong magnetic fields, which obstruct convective heat transport from below the surface. The spots consist of the darker area called *umbra* which is generally surrounded by a less dark area named *penumbra*, as shown in Figure 2.1.2 together with the convection cells.

In addition, also other surface manifestations such as coronal loops, flares, eruptions, among others are recognised to be the result of an underlying magnetic field. Using existing records of the history of sunspots, Hale and collaborators (Hale et al., 1919) realized that sunspots appear in pairs of opposite magnetic polarities, with the polarity of the leading (in the direction of solar rotation) spot being the same for all pairs in one hemisphere while those in the opposite hemisphere have the opposite leading polarity. This behaviour of sunspots lasts roughly 11 years and their polarity is inverted from one cycle to the next. This is known as the *Hale's polarity law*.

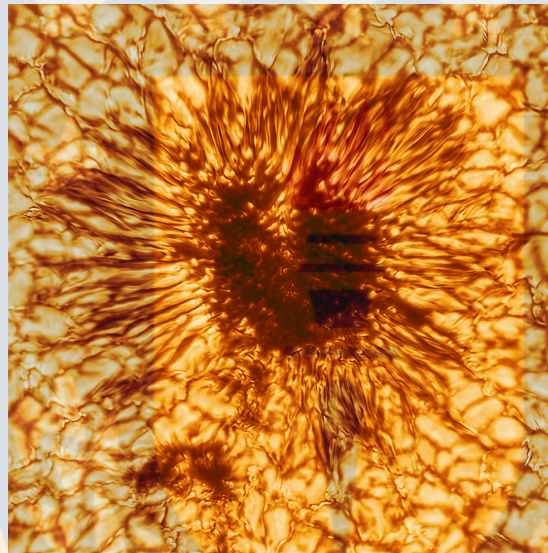


**Figure 2.1.2:** Sunspot image taken on January 28, 2020 by DKIST. Credit: NSO/NSF/AURA.

At the beginning of the cycle, the sunspots start to appear at mid latitudes ( $\sim 40^\circ$ ) in each hemisphere, and while the cycle progresses they appear closer and closer to the equator. As this is a cyclic process a butterfly diagram (due to its wingly shape) of sunspots is formed, as presented in Figure 2.1.3. It shows the longitudinally averaged magnetic field at the surface of the Sun for the last four sunspot cycles, where the change of the polarity from one cycle to the next is clearly seen. The solar magnetic cycle then lasts 22 years, which is twice the length of the sunspot cycle.

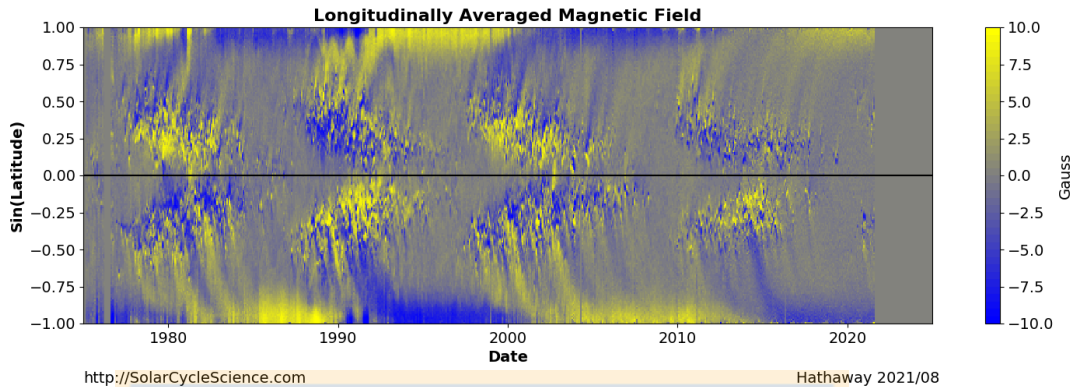


**Figure 2.1.3:** Longitudinally averaged magnetic field at the surface of the Sun for the four last sunspots cycles. Courtesy of D. Hathaway, Solar Cycle Science.

### 2.1.2 M dwarf stars

M dwarfs, also referred to as red dwarfs, are low-mass late-type main-sequence stars which are the most common type of stars in the Galaxy (Winters et al., 2019). They are known to exhibit abundant evidence of surface magnetic activity (Johns-Krull and Valenti, 1996; Kochukhov, 2021). These stars have masses between  $0.08-0.55M_{\odot}$  and effective temperatures of 2450-3850 K. Their luminosities are much lower than that of the Sun. An important property of these stars is that they undergo a change in their stellar structure at  $0.35 M_{\odot}$  (Chabrier and Baraffe, 1997). Above this mass they are partially convective, like the Sun, while with masses below that limit they are fully convective (see the rightmost illustration in figure 2.1.1). The minimum mass of M-dwarfs corresponds to  $0.08M_{\odot}$ ; objects below that mass are considered to be brown dwarfs. Since fully convective M dwarfs do not possess a tachocline, they are of particular interest for dynamo investigations because the role of this shear layer for dynamo operation is debated with authors that support the role of the tachocline for the dynamo operation in solar-like stars (e.g. Charbonneau, 2014) and authors who do not, such as Brandenburg (2005). In this sense, X-ray emission of late-type partially and fully convective stars show a similar trend with the Rossby number ( $rmRo$ ) (Wright and Drake, 2016) (an important dimensionless number that is defined in 2.2.2) such that X-ray emission increases with decreasing  $Ro$  until  $Ro \sim 0.1$  after which the X-ray luminosity saturates. This suggests that dynamos operating in partially and fully convective stars are similar and the tachocline is unimportant.

## 2.2 Magneto-hydrodynamics

Magneto-hydrodynamics (MHD) is the field that studies the interaction of plasmas as fluids with magnetic fields. It describes the macroscopic dynamics of a plasma. MHD is controlled by a combination of the Maxwell and Navier-Stokes equations, taking the Lorentz force into account. The set of equations is given below, first the continuity equation, which describes the conservation of mass,

$$\frac{D \ln \rho}{Dt} = -\nabla \cdot \mathbf{U}, \quad (2.2.1)$$

where  $D/Dt = \partial/\partial t + \mathbf{U} \cdot \nabla$  is the advective derivative,  $\rho$  is the density and  $\mathbf{U}$  is the velocity. The momentum equation is given by

$$\frac{D\mathbf{U}}{Dt} = \mathbf{g} - \frac{1}{\rho} \nabla p + \mathbf{F}_{\text{visc}} + \mathbf{F}_{\text{cent}} + \mathbf{F}_{\text{Cor}} + \mathbf{F}_{\text{Lor}}, \quad (2.2.2)$$

where  $p$  is pressure,  $\mathbf{g}$  is the gravitational acceleration,  $\mathbf{F}_{\text{visc}} = 1/\rho \nabla \cdot (2\nu\rho\mathbf{S})$  is for the viscous forces,  $\mathbf{F}_{\text{cent}} = -\boldsymbol{\Omega} \times (\boldsymbol{\Omega} \times \mathbf{r})$  is for the centrifugal forces,  $\mathbf{F}_{\text{Cor}} = -2\boldsymbol{\Omega} \times \mathbf{U}$  is for the Coriolis force, and  $\mathbf{F}_{\text{Lor}} = 1/\rho \mathbf{J} \times \mathbf{B}$  is for the Lorentz force, where  $\boldsymbol{\Omega}$  is the rotation rate,  $\mathbf{r}$  is the distance from the rotation axis,  $\nu$  is the kinematic viscosity,  $\mathbf{S}$  is the rate-of-strain tensor,  $\mathbf{J}$  is the current density, and  $\mathbf{B}$  is the magnetic field.

The equation for conservation of energy is given by

$$\rho T \frac{Ds}{Dt} = -\nabla \cdot \mathcal{F}_{\text{rad}} + 2\nu S^2 + \eta \nu_0 \mathbf{J}^2 + \Gamma, \quad (2.2.3)$$

where  $s$  is the specific entropy,  $\mathcal{F}_{\text{rad}} = -K\nabla T$  is the radiative flux, where  $K$  is the heat conductivity and  $\Gamma$  correspond to another sources of energy.

Finally, the induction equation describes the evolution of the magnetic field, it is given by

$$\frac{\partial \mathbf{B}}{\partial t} = \nabla \times (\mathbf{U} \times \mathbf{B}) + \eta \nabla^2 \mathbf{B}, \quad (2.2.4)$$

where  $\eta$  is the magnetic diffusivity. The set of MHD equations is supplemented with the solenoidality condition for the magnetic field:

$$\nabla \cdot \mathbf{B} = 0, \quad (2.2.5)$$

and an equation of state is needed to be consistent thermodynamically. For an ideal gas it is given by

$$p = \gamma\rho T = \mathcal{R}\rho T, \quad (2.2.6)$$

where  $\mathcal{R}$  is the universal gas constant,  $\rho$  is density and  $T$  is the temperature of the system.

### 2.2.1 Dimensionless parameters

Dimensionless parameters in fluids and plasmas allow for a quantitative characterization of many physical and astrophysical systems. These numbers usually compare the ratio of two terms in the MHD equations. The following are a few of them:

- (a) The Reynolds number,  $Re$ , is the ratio of the inertial to viscous forces from the momentum equation.  $Re$  determines if a flow is laminar or turbulent. It is given by  $Re = vl/\nu$ , where  $v$  is the typical amplitude of the velocity,  $l$  is a characteristic length scale of the motion and  $\nu$  is the kinematic viscosity.
- (b) The magnetic Reynolds number,  $Re_M = ul/\eta$ , is the ratio of advection to diffusion of  $\mathbf{B}$  in the induction equation. If  $Re_M \ll 1$  the second term in equation 2.2.4 dominates, so the magnetic field obeys a diffusion equation. The energy is lost via Ohmic dissipation. If  $Re_M \gg 1$  the first term in equation 2.2.4 dominates and the magnetic field is frozen in the flow. In this case, the magnetic field is elastic and oscillates at a frequency proportional to the Alfvén velocity.
- (c) The Prandtl number,  $Pr$ , is the ratio of two molecular transport properties, momentum diffusivity to thermal diffusivity. It is given by  $Pr = \nu/\alpha$ , where  $\alpha$  is the thermal diffusivity.
- (d) The Magnetic Prandtl number,  $Pr_M = Re_M/Re = \nu/\eta$ , characterizes the ratio of momentum diffusivity ( $\nu$ ) to magnetic diffusivity ( $\eta$ ).

### 2.2.2 Convection

Magneto-hydrodynamical processes take place mainly in the convection zone of stars. Convection is a process of energy transport that occurs through the movement of fluids. This process takes place when the temperature gradient of an atmosphere exceeds a threshold, causing the atmosphere to become unstable. In stars with convective envelopes like the Sun, convection can be seen in the photosphere, where convective cells called granules lead to the rise of elements hotter than their surroundings, depositing the energy in the surrounding medium. In Fig. 2.1.2 granules around the sunspot can be seen.

The condition under which an atmosphere or a part of a star is unstable to convection is known as the *Schwarzschild criterion* that is given by

$$\left. \frac{d \ln T}{\ln P} \right|_{ad} > \frac{d \ln T}{\ln P}, \quad (2.2.7)$$

where  $T$  is the temperature,  $P$  is the pressure, the suscript *ad* refers to the adiabatic gradient. If the condition is fulfilled, the medium is stable; otherwise, convection (instability) occurs if the temperature gradient in the stellar atmosphere is greater than the adiabatic gradient.

An important dimensionless number that measures the influence of the Coriolis force on convective flows is the *Rossby number* (Rossby, 1939) that is defined by

$$\text{Ro} = \frac{P_{\text{rot}}}{\tau}, \quad (2.2.8)$$

where  $P_{\text{rot}}$  is the rotation period and  $\tau$  is the convective turnover time, which is the typical time connected with convection, e.g.  $l/u$ .

### 2.2.3 Mixing length theory

The mixing length theory is a standard tool for modeling convection zones, proposed by Taylor (1915), Schmidt (1917) and Prandtl (1925). The main idea behind the theory is as follows: take a gas or fluid that is thought to be composed of parcels or elements that advect fluid properties such as heat or momentum. A parcel that comes up as a result of instability has the same properties as its former surrounding. It travels with a characteristic velocity

$v$  with a length  $l$ , known as the mixing length, and finally breaks up, and merges with its surroundings. The mixing length is the characteristic length over which a parcel will conserve its properties. This idea was applied to stellar convection by [Biermann \(1943\)](#).

## 2.3 Dynamo mechanism

A dynamo is a mechanism that maintains a magnetic field in a conducting fluid. The dynamo process converts kinetic into magnetic energy; this process must be efficient enough to compensate for Ohmic dissipation losses. Dynamos can be found to operate at small and large scales. The first correspond to those operating in scales comparable or smaller than the typical scale of the convective eddies, while large scale dynamos operate at the system scale. This thesis focuses on the large scale dynamos responsible for maintaining large scale magnetic fields in stars; a good example is the Solar dynamo.

### 2.3.1 Solar dynamo

As mentioned before, the Sun shows variation of the large scale magnetic field with a periodicity of 22 years that suggests that a dynamo is responsible for maintaining the field. The Solar dynamo has been described by several authors, e.g., [Brandenburg and Subramanian \(2005\)](#); [Charbonneau \(2014, 2020\)](#). The dynamo sustains the large-scale magnetic field and converts the poloidal magnetic field to a toroidal magnetic field and vice versa. The main ingredients by which this is explained are given below.

#### $\Omega$ effect

The  $\Omega$  effect refers to the amplification of the toroidal field by shearing the poloidal field lines via differential rotation. In the Sun the rotation is faster at the equator than at the poles, which is known as solar-like differential rotation (see figure [2.3.1](#)).

Consider an axisymmetric system in cylindrical coordinates  $(R, \varphi, z)$ , and an axisymmetric vector field  $\mathbf{B}$  as follows:

$$\mathbf{B} = \nabla \times (\chi \hat{\varphi} / R) + R\psi \hat{\varphi}, \quad (2.3.1)$$

where  $\chi(R, z, t)$  is a poloidal flux function and  $R\psi$  is the toroidal magnetic field. In the same way, with  $\mathbf{U}$  axisymmetric with respect to the same axis of symmetry as  $\mathbf{B}$ , we can write

$$\mathbf{U} = \mathbf{U}_{\text{pol}} + R\Omega\hat{\phi}, \quad (2.3.2)$$

where  $\mathbf{U}_{\text{pol}}(R, z, t)$  is an axisymmetric poloidal velocity field and  $\Omega(R, z, t)\hat{\phi}$  describes an axisymmetric toroidal differential rotation. Additionally, the poloidal and toroidal components of the induction equation, respectively, are:

$$\frac{\partial \chi}{\partial t} + \mathbf{U}_{\text{pol}} \cdot \nabla \chi = \eta \left( \nabla^2 \chi - \frac{2}{R} \frac{\partial \chi}{\partial R} \right), \quad (2.3.3)$$

$$\frac{\partial \psi}{\partial t} + \mathbf{U}_{\text{pol}} \cdot \nabla \psi = \mathbf{B}_{\text{pol}} \cdot \nabla \Omega + \eta \left( \nabla^2 \psi + \frac{2}{R} \frac{\partial \psi}{\partial R} \right), \quad (2.3.4)$$

where  $\mathbf{B}_{\text{pol}} \cdot \nabla \Omega$  in equation 2.3.4 describes the  $\Omega$  effect, i.e. the stretching of poloidal into toroidal fields by differential rotation. Since there is no relation between  $\psi$  and  $\chi$  in equation 2.3.3, there is no way to generate a toroidal field from a poloidal field. This is known as *Cowling's theorem*, it basically says that a purely axisymmetric magnetic field cannot be sustained by dynamo action (Cowling, 1933); then non-axisymmetric mechanisms are needed to explain how the poloidal field is maintained.

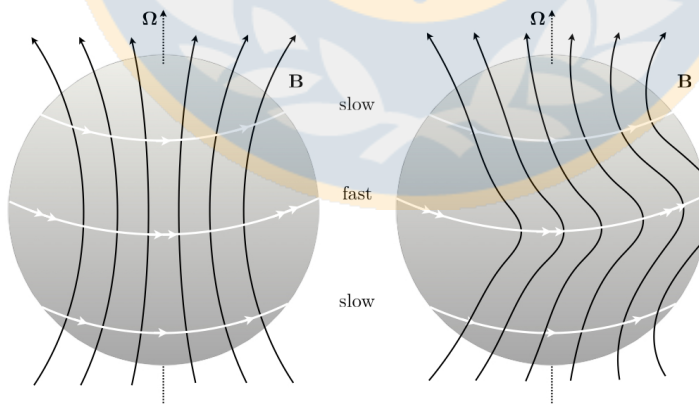


**Figure 2.3.1:** Schematic representation of the Sun differential rotation and the  $\Omega$  effect. The poloidal field lines are stretched due to the latitudinal shear near the equator, producing a toroidal field. Figure from the review by Rincon (2019).

### $\alpha$ effect

The physical mechanism by which the poloidal field is regenerated remains unclear. One of the proposed mechanisms includes turbulence, postulated first by Parker (1955); in this mechanism turbulence has helicity in the presence of rotation, and the helicity twists the toroidal field generating a perpendicular component to the field, the poloidal one. Furthermore, Steenbeck et al. (1966) presented the actual  $\alpha$ -effect with the *mean-field dynamo theory*, a mathematical theory of large-scale dynamos that is briefly presented below.

### Flux transport dynamos

The *Babcock-Leighton mechanism* proposed by Babcock (1961) and Leighton (1969) inspired the *flux transport dynamo* models, in which the tachocline, the shear layer at the bottom of the convection zone, is critical in maintaining the Sun's large-scale magnetic field. The toroidal magnetic field is generated by shearing in the tachocline, whereas the poloidal magnetic field is created by buoyant unstable flux tubes that rise from the tachocline and tilt due to Coriolis force. The meridional circulation (described in 2.4.2) transports the poloidal field to the poles and back to the tachocline in order for the cycle to restart. However, in models of *distributed dynamos*, the tachocline is unimportant (e.g. Käpylä et al., 2006).

### Mean-field dynamo theory

The idea behind *mean-field dynamo theory* or *mean-field electrodynamics* (Krause and Rädler, 1980) is to separate the magnetic and velocity field into a mean and a fluctuating part, considering a two-scale decomposition of the dynamics, using ensembles or averages. That is, the velocity and magnetic fields can be written as follows:

$$U = \bar{U} + u, \quad (2.3.5)$$

$$B = \bar{B} + b, \quad (2.3.6)$$

where  $\bar{U}$  and  $\bar{B}$  are the mean parts (large-scale) of the velocity and magnetic fields, while  $u$  and  $b$  the fluctuating parts. These averages satisfy the Reynolds rules,

$$\overline{\bar{U}_1 + \bar{U}_2} = \bar{U}_1 + \bar{U}_2, \quad (2.3.7)$$

$$\overline{\overline{\mathbf{U}}} = \overline{\mathbf{U}}, \quad (2.3.8)$$

$$\overline{\overline{\mathbf{U}\mathbf{u}}} = 0, \quad (2.3.9)$$

$$\overline{\overline{\mathbf{U}_1\mathbf{U}_2}} = \overline{\mathbf{U}_1\mathbf{U}_2}, \quad (2.3.10)$$

$$\frac{\partial \overline{\mathbf{U}}}{\partial t} = \frac{\partial \overline{\mathbf{U}}}{\partial t}, \quad (2.3.11)$$

$$\frac{\partial \overline{\mathbf{U}}}{\partial x_i} = \frac{\partial \overline{\mathbf{U}}}{\partial x_i}. \quad (2.3.12)$$

These averages are valid if the averaging length is much larger than the eddy scale. Applying these averages to the induction equation (2.2.4), it takes the form:

$$\frac{\partial \overline{\mathbf{B}}}{\partial t} = \nabla \times (\overline{\mathbf{U}} \times \overline{\mathbf{B}} + \overline{\mathbf{u} \times \mathbf{b}} - \eta \mu_0 \mathbf{J}), \quad (2.3.13)$$

where  $\overline{\mathcal{E}} = \overline{\mathbf{u} \times \mathbf{b}}$  is the *mean electromotive force* (EMF). Finding an expression for  $\overline{\mathcal{E}}$  is known as a closure problem, which is solved by writing  $\overline{\mathcal{E}}$  in terms of  $\overline{\mathbf{B}}$  and its gradients. An expression of  $\overline{\mathcal{E}}$  in terms of the large-scale quantities is needed to solve Equation 2.3.13, this is

$$\overline{\mathcal{E}}_i(\mathbf{x}, t) = a_{ij} \overline{B}_j + b_{ijk} \frac{\partial \overline{B}_k}{\partial x_j}, \quad (2.3.14)$$

where  $a_{ij}$  and  $b_{ijk}$  are second and third-order tensors that are solely dependent on the properties of the flow.

There is a linear relation between the mean field  $\overline{\mathbf{B}}$  and the fluctuations  $\mathbf{b}$ , the mean EMF can be expanded as follows:

$$\overline{\mathcal{E}}_i = \alpha_{ij} \overline{B}_j + (\boldsymbol{\gamma} \times \overline{\mathbf{B}})_i - \beta_{ij} (\nabla \times \overline{\mathbf{B}})_j - [\boldsymbol{\delta} \times (\nabla \times \overline{\mathbf{B}})]_i - \frac{\kappa_{ijk}}{2} (\nabla_j \overline{B}_k + \nabla_k \overline{B}_j), \quad (2.3.15)$$

where  $\boldsymbol{\alpha}$  and  $\boldsymbol{\beta}$  are symmetric second-order tensors, the prior one is related to Parker's mechanism mentioned above and can generate a poloidal field from a toroidal field, while the latter is a turbulent magnetic diffusion term,  $\boldsymbol{\gamma}$  and  $\boldsymbol{\delta}$  are vectors, and  $\boldsymbol{\kappa}$  is a third-order tensor. They are given by

$$\alpha_{ij} = \frac{1}{2} (a_{ij} + a_{ji}), \quad (2.3.16)$$

$$\beta_{ij} = \frac{1}{4} (\varepsilon_{ikl} b_{jkl} + \varepsilon_{jkl} b_{ikl}), \quad (2.3.17)$$

$$\gamma_i = -\frac{1}{2}\varepsilon_{ijk}a_{jk}, \quad (2.3.18)$$

$$\delta_i = \frac{1}{4}(b_{jji} - b_{jij}), \quad (2.3.19)$$

$$\kappa_{ijk} = -\frac{1}{2}(b_{ijk} + b_{ikj}), \quad (2.3.20)$$

where  $\varepsilon_{ijk}$  is the antisymmetric Levi-Cevita tensor.

## 2.4 Flow properties

As mentioned previously, large-scale flows and flow properties contribute to the dynamo operation in the convection zone of stars, such as differential rotation, meridional circulation and kinetic helicity, that are briefly described below.

### 2.4.1 Differential rotation

Differential rotation (DR) refers to a non-uniform angular velocity of the convection zone that is mainly produced by the action of the Reynolds stresses, which are correlations of the turbulent (fluctuating) velocity components. The Coriolis force operates on turbulence, which then reacts to redistribute angular momentum, modifying the global rotation behaviour, and producing differential rotation. Thus, the interplay of rotation and convection explains DR (e.g. [Rüdiger, 1989](#)).

As demonstrated in the work of [Schou et al. \(1998\)](#), helioseismology and Doppler imaging data allowed researchers to investigate the inner angular velocity of the Sun. Since the angular velocity varies not only with latitude but also with depth, the amplitude of the differential rotation can be measured radially and latitudinally, as shown in the work of [Käpylä et al. \(2013\)](#). This is the situation with the Sun, where the convection zone rotates faster near the equator than at the poles, as illustrated in [Figure 2.4.1](#), which depicts the rotation rate of the Sun as a function of latitude and radius.

### 2.4.2 Meridional circulation

Meridional circulation is a large-scale flow that transports angular momentum and contributes to the energy transport inside stars. It has longitudinally averaged north-south and radial velocity components. Meridional circulation is driven by thermal wind and Reynolds stress. Meridional circulation has been shown to have a significant impact on solar dynamo models (Choudhuri et al., 1995), such as flux transport models, where meridional circulation causes magnetic activity to migrate equatorward throughout the duration of the solar cycle.

Meridional circulation in the Sun moves matter poleward at the surface and equatorward at some unknown depth. (reviewed in Choudhuri, 2021).

### 2.4.3 Kinetic helicity

Kinetic helicity is a measure of the winding and linking of vortex lines in fluids. It is produced in rotating fluids such as stars. For the  $\alpha$ -effect to work, an underlying velocity field with lack of reflectional symmetry associated with a non-zero kinetic helicity is needed Krause and Rädler (1980). The kinetic helicity is given by

$$\mathcal{H} = \int_V \boldsymbol{\omega} \cdot \mathbf{u} dV, \quad (2.4.1)$$

where  $\boldsymbol{\omega}$  is the vorticity.

For stars, the sign of  $\mathcal{H}$  is important. For example, a poleward-propagating dynamo wave is expected when a negative kinetic helicity on the northern hemisphere is found. This is known as the Parker-Yoshimura rule after Parker (1955) and Yoshimura (1975).

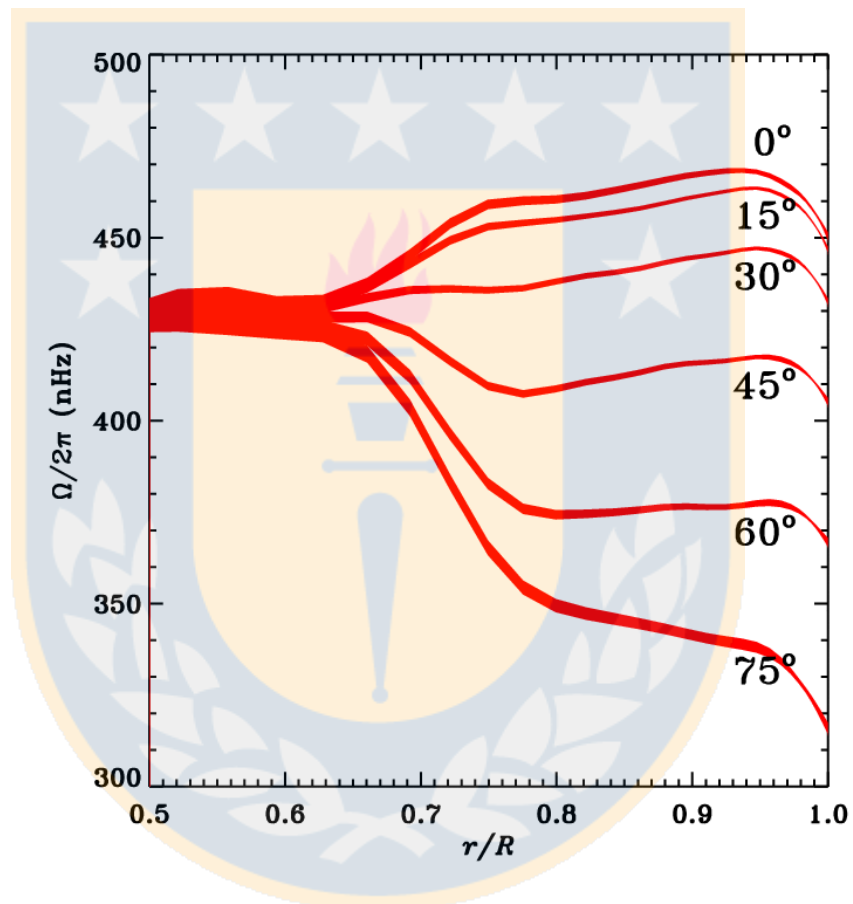


**Figure 2.4.1:** Rotation rate of the sun at different latitudes as a function of depth. The error bars are shown by the thickness of the curves. Credits: GONG/NSO/AURA/NSF.

## Chapter 3

# Computational methods

A description of the codes used, Modules for Experiments in Stellar Astrophysics and the Pencil Code is given in this chapter. The numerical model, stellar parameters, and relations between code and physical units are also discussed.

### 3.1 MESA

Modules for Experiments in Stellar Astrophysics (MESA<sup>1</sup>; Paxton et al. 2010) is an open source library with a variety of modules. It employs adaptive mesh refinement and time step controls, as well as OpenMP-based shared memory parallelism. The one-dimensional stellar evolution module `star` was used in this work with the aim of obtaining the stellar parameters for an M5 star.

Once MESA is installed it is possible to run simulations. First thing to do is setup the configuration files which are in the run directory.

#### 3.1.1 Files to set in the run directory

There are three configuration files. ‘`inlist`’ tells MESA whether it can find its configuration information elsewhere. ‘`inlist_project`’ is the file that contains the parameters that control the simulation. For example, one may select whether or not the simulation should begin with a pre-main sequence model and when to stop it, as well as the initial mass, rotation rate, and

<sup>1</sup><https://github.com/MESAHub/mesa/releases>

energy conservation options, among other control functions. `inlist_pgstar` is for setting options for plotting a Hertzsprung-Russell diagram and a temperature/density profile while the simulation is running.

To compile and run a simulation one has to use the shell scripts ‘`mk`’ and ‘`rn`’.

### 3.1.2 Output files

The output files are stored in the ‘LOG’ directory. The history of the run is kept in the file ‘`history.data`’, one line per recorded model. Column numbers appear on the first line of `history.data`, column names appear on the second line, and the values appear on the following lines. ‘`profiles.index`’ sets the number of profiles to be saved, since saving every profile would require too much disk space. ‘`profile#.data`’ (# indicate the profile number) saves information about the selected models. Temperature, density, pressure, mass percentage of hydrogen, helium, and metals, among other variables, are all contained in these profiles, which span the stellar radius. The variables contained in ‘`history.data`’ and ‘`profile#.data`’ can be set in

```
$MESA_DIR/star/defaults/history_columns.list,
$MESA_DIR/star/defaults/profile_columns.list.
```

### 3.1.3 Structure and composition equations

The stellar structure is divided into cells ( $k$ ), which are numbered from the surface to the center of the star. MESA star solves both the structure and composition equations simultaneously, from top to bottom (see section 6.2 of Paxton et al. 2010). The mass conservation equation is given in a finite volume form as follows:

$$\rho_k = \frac{dm_k}{(4/3)\pi(r_k^3 - r_{k+1}^3)}, \quad (3.1.1)$$

where  $\rho_k$ ,  $m_k$  and  $r_k$  are boundary variables for density, mass and radius, respectively. The momentum conservation at the interior of the cell boundaries is given by

$$P_{k-1} - P_k = \overline{dm_k} \left[ -\frac{Gm_k}{4\pi r_k^4} - \frac{a_k}{4\pi r_k^2} \right], \quad (3.1.2)$$

where  $P_k$  is the pressure,  $\overline{dm}_k = 0.5(dm_{k-1} + dm_k)$  and  $a_k$  is the Lagrangian acceleration. The energy transport through the cell boundaries is given by

$$T_{k-1} - T_k = \overline{dm}_k \left[ \nabla_{T,k} \left( \frac{dP}{dm} \right) \frac{\overline{T}_k}{\overline{P}_k} \right], \quad (3.1.3)$$

where  $\nabla_{T,k} = d \ln T / d \ln P$ ,  $\overline{T}_k$  and  $\overline{P}_k$  are temperature and pressure interpolated by mass, respectively. The energy conservation equation is

$$L_k - L_{k-1} = dm_k (\epsilon_{\text{nuc}} - \epsilon_{v,\text{thermal}} + \epsilon_{\text{grav}}), \quad (3.1.4)$$

where  $\epsilon_{\text{nuc}}$  is the total nuclear reaction specific energy generation rate minus the nuclear reaction neutrino-loss rate,  $\epsilon_{v,\text{thermal}}$  is the specific thermal neutrino loss rate, and  $\epsilon_{\text{grav}}$  is the specific rate at which gravitational energy changes.

## 3.2 The Pencil code

The simulations were run with the PENCIL CODE<sup>2</sup> (Pencil Code Collaboration et al., 2021), which is a high-order finite-difference code for solving differential equations with primary applications in compressible astrophysical magnetohydrodynamics. The code works efficiently under the Message Passing Interface (MPI) on massively parallel computers with shared or distributed memory. MPI is a message-passing library that is built specifically for parallel computing systems. The equations that Pencil solves are the non-ideal MHD equations, which are given in the description of the model, in section 3.3.

### 3.2.1 Starting

The code is stored in Github and can be downloaded in Linux with the command

```
git clone https://github.com/pencil-code/pencil-code.git
```

In order to use the code, one has to take into account its systems requirements:

- *F95* and *C* compiler,
- a *Unix/Linux*-type system with *make* and *csh*,

<sup>2</sup><https://github.com/pencil-code>

- *Perl*,
- an *MPI* (Message Passing Interface) for parallelization on multiprocessor systems (for the use of more than one CPU),
- *IDL* or *Python* for visualization of the results.

Once the code is installed the environment must be set in the `pencil-code` directory as follows (for `cs`h or `tc`sh users):

```
sh > cd pencil-code
sh > ./sourceme.sh
```

### Files in the run directory

Then, the folders to work in must be configured. This is done by the script `pc_setupsrc` which is in the folder `pencil-code/bin`. In the run directory one can find files, such as: `start.in`, `run.in`, `phiaver.in`, `print.in`, `run.csh`, `start.csh`, the sub-directory `src` with the files `Makefile.local` and `cparam.local`. These files we need to set up according to our simulations. Also, a sub-directory called `data` is needed to store the output data.

The files with the extension `.in` specify the startup, runtime and output parameters in the time series and averages over  $\phi$ , respectively. The files ending with `.csh` are links to the `pencil-code/bin` directory to initialize the code. `Makefile.local` allows to chose individual physical and technical modules, which are described in 3.2.2, and `cparam.local` allows to set the grid size and the number of processors for each direction. The sub-directory `data` has the following output files:

- `dim.dat`: Stores the global array dimensions.
- `legend.dat`: The header line specifying the names of the diagnostic variables in `time_series.dat`.
- `time_series.dat`: Time series of diagnostic variables.
- `tsnap.dat`: Time when the next snapshot 'VARN' should be written.
- `params.log`: Keeps a log of all the parameters.

- ‘param.nml’: Set of startup parameters.
- ‘param2.nml’: Set of runtime parameters.
- ‘proc0’, ‘proc1’, ... : Directories with data from the individual processors. Each of the directories can contain the following files:
  - ‘var.dat’: binary file storing the latest snapshot,
  - ‘VARN’: binary file storing individual snapshot number N,
  - ‘dim.dat’: file storing the array dimensions,
  - ‘time.dat’: file storing the time corresponding to ‘dim.dat’,
  - ‘grid.dat’: binary file storing the part of the grid seen by the given processor.

### Compiling and running

To compile with the usage of multi-processor with GNU/MPI one has to use:

```
unix > pc_build -GNU-GCC_MPI
```

This command is dependent on the system users are working on. A helpful command for removing produced files in the event of a e.g. typo is:

```
unix > pc_build -cleanall
```

For running the code one has to use the `pc_run` command.

### Running Pencil Code simulations using SLURM

Simple Linux Utility for Resource Management (SLURM) is a system for job management and job scheduling for Linux clusters. This work was mainly developed running simulations on clusters.

The main functions of SLURM are to grant access to computing nodes for predetermined amounts of time in order for them to complete tasks. It offers a framework for launching, executing, and monitoring work across the set of assigned nodes. Furthermore, it resolves resource contention by maintaining a queue of pending tasks.

### 3.2.2 Modularity

The Pencil Code is highly modular, which means it has modules that may be turned on and off in the 'src/Makefile.local' file based on the needs of the user. For example, the settings for the simulations with the *star-in-a-box* setup, which is described in 3.3, are:

```
MPICOMM = mpicomm
IO       = io_dist
FILE_IO  = file_io_f2003

HYDRO    = hydro
DENSITY  = density
ENTROPY  = entropy
MAGNETIC = magnetic
RADIATION = noradiation
PSCALAR  = nopscalar
EOS      = eos_idealgas

GRAVITY  = gravity_r
FORCING  = noforcing
SHEAR    = noshear
TIMEAVG  = timeavg

REAL_PRECISION = double
```

The first three modules are technical, the MPI (for multiprocessor use) which is activated, with input/output distributed over processors. The subsequent ones are physics modules, such as hydro which is activated and it deals with things related to the velocity, the density module (activated), the entropy module (activated) that solves the entropy equation, magnetic fields are activated, while radiation and pscalar for additional passive scalar field are switched off. The EOS (equation of state) implements the ideal gas equation, the gravity module sets the gravity field (activated), the forcing and shear modules are switched off. The last option specifies the precision, which in this case is double precision (8-byte floating point numbers).

### 3.2.3 Output files

#### Time series

The time series are written every  $nt$  time step in 'dat/time\_series.dat'. The user can choose which parameters to save in 'print.in'. Part of the output can contain the following diagnostic quantities:

1.  $it$  indicates the current time step,
2. the time,  $t$ ,
3.  $dt$  indicates the length of the time step,
4.  $urms$ , indicates the rms velocity,  $\sqrt{\langle \bar{u}^2 \rangle}$ ,
5.  $umax$  indicates the maximum velocity,  $\max|\mathbf{u}|$ ,
6. the rms vorticity,  $orms$ ,  $\sqrt{\langle \bar{\omega}^2 \rangle}$ ,
7. the kinetic helicity,  $oum$ ,  $\langle \boldsymbol{\omega} \cdot \mathbf{u} \rangle$ ,
8. the mean density,  $\text{rhom} = \langle \rho \rangle$ ,
9.  $brms$  indicates the rms magnetic field,  $\sqrt{\langle \bar{b}^2 \rangle}$ ,
10.  $inertia_{xx\_car}$ ,  $inertia_{yy\_car}$ ,  $inertia_{zz\_car}$  are the  $xx$ ,  $yy$  and  $zz$  components of the inertia tensor.

#### Snapshot, video, slice files and averages

Snapshot files include full information about primary variables. There are two sorts of snapshot files: current and permanent snapshots, both of which are stored in a 'data/procN' directory. These files can be used to restart a simulation from a certain point according to the needs of the user, such as changing the resolution or an input variable.

Slice files contain information of variables in a given plane, which can be configured in 'run.in', respectively. The video files can be read using the program 'src/read\_all\_videofiles.x', whereas slices are found in 'data/proc\*/' and they are written in the each processor.

The averages can be in one or two dimensions. They are listed in the files 'xyaver.in', 'xzaver.in' and 'yzaver.in', where the first two letters

indicate the averaging directions.

### 3.3 The star-in-a-box model with the Pencil Code

We use the star-in-a-box model described by Käpylä (2021), which is based on the set-up by Dobler et al. (2006). The model allows dynamo simulations of fully convective stars. In the current case we employ a sphere of radius  $R$  embedded in a cubic box with a length of  $2.2R$ . We solve the magnetohydrodynamic equations of induction, continuity, motion and energy conservation given as

$$\frac{\partial \mathbf{A}}{\partial t} = \mathbf{u} \times \mathbf{B} - \eta \mu_0 \mathbf{J}, \quad (3.3.1)$$

$$\frac{D \ln \rho}{Dt} = -\nabla \cdot \mathbf{u}, \quad (3.3.2)$$

$$\frac{D \mathbf{u}}{Dt} = -\nabla \Phi - \frac{1}{\rho} (\nabla p - \nabla \cdot 2\nu \rho \mathbf{S} + \mathbf{J} \times \mathbf{B}) - 2\boldsymbol{\Omega} \times \mathbf{u} + \mathbf{f}_d, \quad (3.3.3)$$

$$T \frac{Ds}{Dt} = -\frac{1}{\rho} [\nabla \cdot (\mathbf{F}_{\text{rad}} + \mathbf{F}_{\text{SGS}}) + \mathcal{H} - \mathcal{C}] + 2\nu \mathbf{S}^2 + \mu_0 \eta \mathbf{J}^2, \quad (3.3.4)$$

where  $\mathbf{A}$  is the magnetic vector potential,  $\mathbf{u}$  is the velocity field,  $\mathbf{B} = \nabla \times \mathbf{A}$  is the magnetic field,  $\mu_0$  is the magnetic permeability of the vacuum,  $\eta$  is the magnetic diffusivity,  $\rho$  is the density of the fluid,  $D/Dt = \partial/\partial t + \mathbf{u} \cdot \nabla$  is the convective derivative,  $T$  is the temperature,  $p$  is the pressure,  $\nu$  is the kinematic viscosity,  $s$  is the specific entropy,  $\mathbf{J} = \nabla \times \mathbf{B}/\mu_0$  is the current density,  $\boldsymbol{\Omega} = \Omega_0 \hat{\mathbf{z}}$  is the rotation vector, with  $\Omega_0$  being the rotation rate of the star and  $\hat{\mathbf{z}}$  the vertical unit vector.  $\Phi$  is the gravitational potential that corresponds to an isentropic hydrostatic state of the star which is given by

$$\Phi(r) = -\frac{GM}{R} \frac{a_0 + a_2 r'^2 + a_3 r'^3}{1 + b_2 r'^2 + b_3 r'^3 + a_3 r'^4}, \quad (3.3.5)$$

where  $G$  is the gravitational constant,  $M$  is the mass of the star,  $a_0 = 2.34$ ,  $a_2 = 0.44$ ,  $a_3 = 2.60$ ,  $b_2 = 1.60$ ,  $b_3 = 0.21$  and  $r' = r/R$ .

$\mathbf{S}$  is the traceless rate-of-strain tensor,

$$S_{ij} = \frac{1}{2}(u_{i,j} + u_{j,i}) - \frac{1}{3}\delta_{ij} \nabla \cdot \mathbf{u}, \quad (3.3.6)$$

where the commas denote differentiation and  $\delta_{ij}$  is the Kronecker delta.

$f_d$  describes the damping of flows outside the star which is given by

$$\mathbf{f}_d = -\frac{\mathbf{U}}{\tau_{\text{damp}}} f_e(r), \quad (3.3.7)$$

where  $\tau_{\text{damp}} \approx 1$  is a damping timescale, and  $f_e(r)$  is described by

$$f_e(r) = \frac{1}{2} \left( 1 + \tanh \frac{r - r_{\text{damp}}}{\omega_{\text{damp}}} \right), \quad (3.3.8)$$

where  $r_{\text{damp}} = 1.03R$  and  $\omega_{\text{damp}} = 0.03R$ .

$\mathcal{H}$  and  $\mathcal{C}$  describe heating and cooling, respectively.  $\mathcal{H}$  is given by a normalised Gaussian profile:

$$\mathcal{H}(r) = \frac{L_{\text{sim}}}{(2\pi\omega_L^2)^{3/2}} \exp\left(-\frac{r^2}{2\omega_L^2}\right), \quad (3.3.9)$$

where  $L_{\text{sim}}$  correspond to the luminosity in the simulation and  $\omega_L$  is the width of the Gaussian.  $\mathcal{C}$  models stellar surface radiative losses and it is given by

$$\mathcal{C} = \rho c_p \frac{T(\mathbf{x}) - T_{\text{surf}}}{\tau_{\text{cool}}} f_e(r), \quad (3.3.10)$$

where  $\tau_{\text{cool}} = \tau_{\text{damp}}$  is a cooling timescale.

$\mathbf{F}_{\text{rad}}$  is the radiative flux given by

$$\mathbf{F}_{\text{rad}} = -K\nabla T, \quad (3.3.11)$$

where

$$K(\rho, T) = K_0(\rho/\rho_0)^{a-1}(T/T_0)^{b+3}, \quad (3.3.12)$$

where  $a = -1$  and  $b = 7/2$  corresponds to the Kramers' opacity law.

$\mathbf{F}_{\text{SGS}}$  is the subgrid-scale (SGS) entropy flux that does not contribute to the net energy transport, but it damps fluctuations near grid scale, and it is given by

$$\mathbf{F}_{\text{SGS}} = -\chi_{\text{SGS}}\rho\nabla s', \quad (3.3.13)$$

where  $\chi_{\text{SGS}}$  is the SGS diffusion coefficient,  $s' = s - \bar{s}_t$  is the entropy fluctuation and  $\bar{s}_t$  is a running temporal mean of entropy.

### 3.3.1 Control parameters and physical units

The parameters that define the model are the dimensionless luminosity  $\mathcal{L}$  which was defined by [Dobler et al. \(2006\)](#) as

$$\mathcal{L} = \frac{L_{\text{sim}}}{\sqrt{G^3 M^5 / R^5}}. \quad (3.3.14)$$

The density stratification is determined by the dimensionless pressure scale height at the surface

$$\xi_0 = \frac{\mathcal{R} T_{\text{surf}}}{GM/R}, \quad (3.3.15)$$

where  $T_{\text{surf}} = T(r = R)$ . For our simulations we have  $\mathcal{L} = 5.5 \cdot 10^{-5}$  and  $\xi_0 = 0.062$ .

#### Stellar parameters

We used the stellar parameters for an M5 dwarf which were the same as those used by [Käpylä \(2021\)](#), i.e. stellar mass  $M_\star = 0.21M_\odot$ , radius  $R_\star = 0.27R_\odot$ , and luminosity  $L_\star = 0.008L_\odot$ . We used an effective temperature  $T_{\text{eff}} = 4000$  K and a central density  $\rho_c^\star \approx 1.5 \cdot 10^5 \text{ kg m}^{-3}$ . These are typical values for an M5 dwarf and they were verified using simulations with the MESA code ([Paxton et al., 2010](#)). Hence, for a real M5 star we have  $\xi_\star = 2.2 \cdot 10^{-4}$  and  $\mathcal{L}_\star = 2.4 \cdot 10^{-14}$ .

The surface gravity for the star is given by

$$g_\star = \frac{GM_\star}{R_\star^2} = \frac{0.21}{(0.27)^2} \frac{GM_\odot}{R_\odot^2} \approx 2.9g_\odot \approx 750 \frac{m}{s^2}, \quad (3.3.16)$$

where  $g_\odot = 260 \text{ m s}^{-2}$ .

#### Enhanced luminosity approach

We use here the enhanced luminosity approach described by [Käpylä et al. \(2020\)](#), where the gap between the shortest (acoustic timestep) and longest (Kelvin-Helmholtz time) timescales is compressed such that the latter can be

resolved in the simulations. The luminosity ratio between the simulated star and a real M5 star is  $L_{\text{ratio}} = \mathcal{L}/\mathcal{L}_\star \approx 2.1 \cdot 10^9$ . Since the enhanced luminosity leads to an increase of the convective velocity as  $u_{\text{conv}} \propto L_{\text{ratio}}^{1/3}$ , the velocities are greater by a factor of  $L_{\text{ratio}}^{1/3} \approx 1280$ . These scaling relations have been established in various previous studies (Käpylä et al., 2020; Navarrete et al., 2021), and allow us to relate our numerical results to astrophysical stars.

### Relations between code units and physical units

Working with numerical simulations does not automatically give values in physical units; therefore, we must convert from simulations to physical units in order to better understand the results.

The conversion factor for the rotation rate is given by

$$\Omega^{\text{sim}} = L_{\text{ratio}}^{1/3} \left( \frac{g^{\text{sim}} R_\star}{g_\star R^{\text{sim}}} \right)^{1/2} \Omega_\star, \quad (3.3.17)$$

where  $g^{\text{sim}} = g^{\text{sim}}(r = R) = 1$  and  $R = 1$  and  $\Omega_\star$  is the rotation rate of the star. The conversion factor for length is given by

$$\boldsymbol{x} [\text{m}] = \left( \frac{R_\star}{R^{\text{sim}}} \right) \boldsymbol{x} [\text{sim. units}]. \quad (3.3.18)$$

The conversion factor for time is

$$t [\text{s}] = \left( \frac{\Omega^{\text{sim}}}{\Omega_\star} \right) t [\text{sim. units}]. \quad (3.3.19)$$

The factor for the velocity conversion is the ratio of the factors of length and time

$$\boldsymbol{U} [\text{m s}^{-1}] = \left( \frac{\Omega_\star R_\star}{\Omega^{\text{sim}} R^{\text{sim}}} \right) \boldsymbol{U} [\text{sim. units}]. \quad (3.3.20)$$

For the conversion factor of the magnetic field we need a reference density in physical units. We used the central density of the star, which for an M5 star is  $\rho_c^\star \approx 1.5 \cdot 10^5 \text{ kg m}^{-3}$ . The conversion factor is

$$\boldsymbol{B} [\text{T}] = \left[ \frac{\mu_0 \rho_c^\star (\Omega_\star R_\star)^2}{\mu^{\text{sim}} \rho_c^{\text{sim}} (\Omega^{\text{sim}} R^{\text{sim}})^2} \right] \boldsymbol{B} [\text{sim. units}], \quad (3.3.21)$$

where  $\mu_0 = 4\pi \cdot 10^7 \text{ H m}^{-1}$  is the magnetic permeability of vacuum, with

$\mu_0^{\text{sim}} = 1$  and  $\rho_c^{\text{sim}} = 1$ .



## Chapter 4

# Three-dimensional MHD simulations with varying magnetic Prandtl number and rotation period

In this chapter, the results of the simulations, which include large-scale magnetic fields, large-scale flows, and flow properties, are presented in detail, along with the results of the thesis. The viability of a small-scale dynamo is also explored.

### 4.1 Simulations

As mentioned in 2.1.2, large-scale magnetic fields have been observed on the surfaces of fully convective M dwarfs. Numerical simulations are an important way to understand the physics that operate in this environment. This section contains a description of the simulations performed in this thesis.

The simulations are divided into two groups: there are simulations with varying magnetic Prandtl number, a dimensionless number which is briefly introduced in 2.2.1, and simulations with varying rotation period. The magnetic Prandtl number is important for dynamo activity, as established before in many contexts, such as in works with simulations of the turbulent dynamo by Federrath et al. (2014), or the work by Schekochihin et al. (2007) with numerical simulations of forced turbulence. The magnetic Prandtl number

is given by the ratio of kinematic viscosity,  $\nu$ , to magnetic diffusivity,  $\eta$ , which for hydrogen plasma is (Brandenburg and Subramanian, 2005)

$$\text{Pr}_M = \frac{\nu}{\eta} = 1.1 \times 10^{-4} \left( \frac{T}{10^6 \text{ K}} \right)^4 \left( \frac{\rho}{0.1 \text{ g cm}^{-3}} \right)^{-1} \left( \frac{\ln \Lambda}{20} \right)^{-2}, \quad (4.1.1)$$

with  $\ln \Lambda$  the Coulomb logarithm. It is clear from this that  $\text{Pr}_M$  is strongly affected by temperature and density. Cool astronomical bodies with high densities have low  $\text{Pr}_M$ , which is the case for the solar convection zone, where the values of  $\text{Pr}_M$  range from  $10^{-7}$  to  $10^{-4}$ . However, reaching very low values of the magnetic Prandtl number is numerically unfeasible since simulations can only be performed with a finite numerical resolution, i.e., the smallest scale (grid spacing) which the simulation can resolve, which is determined by the computer resources available. The smallest scale in simulations is not even near the smallest scale in real systems. This limitation has an impact on other dimensionless parameters as well, such as the fluid Prandtl number and the Reynolds numbers. It is therefore quite helpful to be able to work with as high a resolution as possible in order to get more realistic outcomes. In the case of this work, it has been possible to perform simulations with magnetic Prandtl numbers between 0.1 to 10, which is a wide explored range if we consider the state of art, like the simulations of spherical shells with  $0.25 \leq \text{Pr}_M \leq 5$  (Käpylä et al., 2017). Regarding the grid resolution, simulations were performed with  $200^3$ ,  $288^3$  and  $576^3$ .

On the other hand, the rotation period of the star has also been varied, considering  $P_{\text{rot}}$  of 43, 61 and 90 days. In this regime, stars are considered to be slow to intermediate rotators. Rotation periods of fully convective M dwarfs have been reported in a wide range, with values from a few hours for the rapid rotators, to rotation periods of 90 days, as in the case of Proxima Centauri. Table 4.1.1 contains a summary of the simulations performed here, which are divided into three sets. Set A is for simulations with  $P_{\text{rot}} = 43$  days, set B for  $P_{\text{rot}} = 61$  days and set C is for  $P_{\text{rot}} = 90$  days. In addition to the dimensionless parameters described before (the fluid and magnetic Reynolds number given in 2.2.1) other ones are also given, such as the subgrid-scale Prandtl number,

$$\text{Pr}_{\text{SGS}} = \frac{\nu}{\chi_{\text{SGS}}}, \quad (4.1.2)$$

where  $\chi_{\text{SGS}}$  is the subgrid-scale entropy diffusion. The parameter that gives the ratio of Coriolis forces to viscous forces is the Taylor number

$$\text{Ta} = \frac{4\Omega_0^2 R^4}{\nu^2}, \quad (4.1.3)$$

where  $\Omega_0 = 2\pi/P_{\text{rot}}$ . Additionally, the ratio of advection of temperature or entropy by the flow to the diffusion of the same physical quantity is given by the Péclet number. If the Péclet number is large, heat transfer is dominated by advection; when it is small, diffusion dominates. The Péclet number is given by

$$\text{Pe} = \frac{u_{\text{rms}}}{\chi_{\text{SGS}} k_R}, \quad (4.1.4)$$

where  $u_{\text{rms}}$  is the volume averaged root-mean-square velocity within a spherical radius  $r < R$ , and  $k_R = 2\pi/R$  is the scale of the largest convective eddies. The rotational influence on the flow is measured by the Coriolis number

$$\text{Co} = \frac{2\Omega_0}{u_{\text{rms}} k_R}. \quad (4.1.5)$$

## 4.2 Results

This section presents the results of this thesis, regarding large-scale magnetic fields under the different scenarios explored here.

### 4.2.1 Large-scale magnetic fields at different $\text{Pr}_M$

Magnetic fields that are coherent over large spatial scales are known as large-scale magnetic fields. In most of the presented simulations, large-scale magnetic fields are similar to the large structures of the Sun. Prior to the formation of large-scale magnetic fields, a seed magnetic field is amplified in the kinematic regime where the field grows exponentially. The seed field in the case of the simulations presented here is a random small-scale field of about  $\sim 1$  G. The kinematic stage lasts until the magnetic forces are comparable to the turbulent forces, at which point the magnetic field growth enters a saturated and non-linear stage. This last stage is of interest to the study of the effects of magnetic fields in stars. Figure 4.2.1 shows the evolution of  $B_{\text{rms}}$  for

Sim	$u_{\text{rms}}[\text{m/s}]$	$B_{\text{rms}}[\text{kG}]$	$\text{Pr}_M$	$\text{Pr}_{\text{SGS}}$	$\text{Re}_M$	Re	Co	Ta	Pe	Grid
A1	10.1	12.0	0.1	0.04	54	548	10	$4.6 \cdot 10^{10}$	21.9	$200^3$
A2	10.1	12.3	0.1	0.04	78	784	10	$9 \cdot 10^{10}$	31.8	$288^3$
A3	10.1	11.8	0.2	0.08	54	271	10	$1.1 \cdot 10^{10}$	21.7	$200^3$
A4	10.1	10.5	0.5	0.20	54	108	10	$1.8 \cdot 10^9$	21.7	$200^3$
A5	10.1	9.1	0.7	0.28	55	78	10	$9.5 \cdot 10^8$	21.9	$200^3$
A6	9.6	11.3	0.7	0.28	74	106	10	$1.9 \cdot 10^9$	29.8	$200^3$
A7	9.9	10.6	0.9	0.20	53	107	10	$1.8 \cdot 10^9$	21.5	$200^3$
A8*	14.0	$2 \cdot 10^{-4}$	0.2	0.28	21	108	7	$9.5 \cdot 10^8$	30.3	$200^3$
A9	10.0	9.5	0.5	0.28	39	77	10	$9.5 \cdot 10^8$	21.8	$200^3$
A10	10.5	11.0	1	0.20	104	104	10	$1.8 \cdot 10^9$	20.9	$200^3$
A11	9.4	10.7	1	0.28	72	72	11	$9.5 \cdot 10^8$	20.3	$200^3$
A12*	13.0	$2 \cdot 10^{-3}$	1	0.40	69	69	8	$4.6 \cdot 10^8$	27.8	$200^3$
A13	9.2	9.7	2	0.40	98	49	11	$4.6 \cdot 10^8$	19.9	$200^3$
A14	7.7	12.3	5	0.40	208	41	13	$4.6 \cdot 10^8$	16.6	$200^3$
A15	7.7	11.5	7	0.40	298	41	13	$4.6 \cdot 10^8$	16.7	$200^3$
A16	7.3	11.7	10	0.40	388	39	14	$4.6 \cdot 10^8$	15.6	$200^3$
B1	11.1	9.8	0.5	0.40	83	166	6	$1.7 \cdot 10^9$	67.5	$200^3$
B2	11.2	10.7	1	0.40	167	167	6	$1.7 \cdot 10^9$	67.8	$576^3$
B3	10.5	12.0	2	0.40	314	157	7	$1.7 \cdot 10^9$	63.7	$576^3$
B4	9.8	12.4	5	0.40	735	147	7	$1.7 \cdot 10^9$	58.4	$576^3$
B5	9.1	11.9	10	0.40	1367	136	8	$1.7 \cdot 10^9$	55.2	$576^3$
C1	11.9	12.3	1	0.20	256	256	4	$1.8 \cdot 10^9$	55.2	$288^3$
C2*	15.0	$6 \cdot 10^{-5}$	0.5	0.4	40	80	3	$1.1 \cdot 10^8$	32.4	$200^3$
C3	12.3	8.4	1	0.40	66	66	4	$1.1 \cdot 10^8$	26.6	$200^3$
C4	11.3	12.3	2	0.40	336	168	4	$9 \cdot 10^8$	68.0	$576^3$
C5	10.0	15.1	5	0.40	749	150	5	$9 \cdot 10^8$	60.6	$576^3$
C6	9.5	12.0	10	0.40	1423	142	5	$9 \cdot 10^8$	57.5	$576^3$

**Table 4.1.1:** Summary of the simulations. From left to right the columns correspond to the simulation name, root-mean-square velocity, root-mean-square magnetic field strength, magnetic and sub-grid-scale Prandtl number, magnetic and fluid Reynolds number, Coriolis number which is  $\text{Co} = \text{Ro}^{-1}$ , Taylor and Peclet numbers. The last column indicates the grid resolution that was used. Asterisks indicate runs with no dynamo.

different simulations.

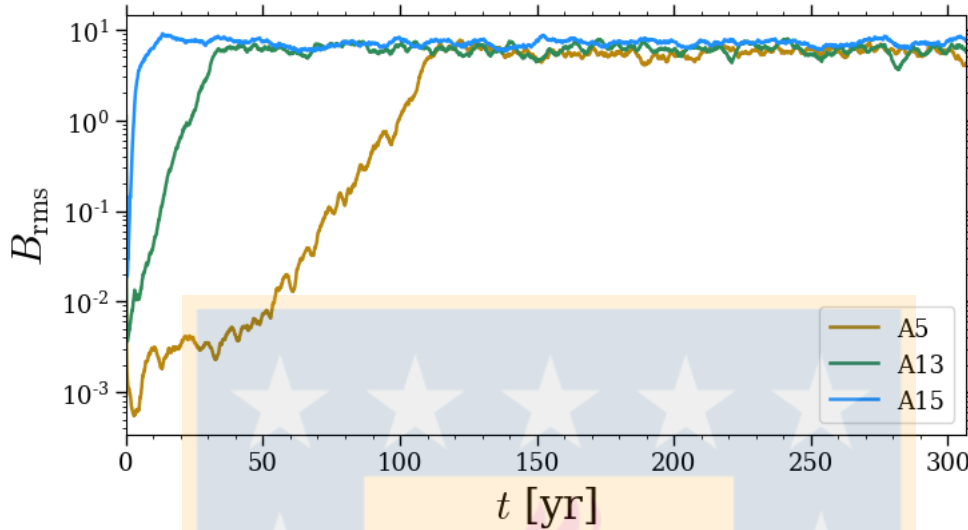


**Figure 4.2.1:** Time evolution of volume averaged rms magnetic field of simulations A5, A13 and A15. The kinematic stage is shorter for increasing magnetic Prandtl number.

#### 4.2.1.1 Toroidal magnetic field

Some of the simulations show cycles of the large-scale magnetic field with periods ranging from 7 to 10 years. These cycles can be seen in Figures 4.2.2 and 4.2.3 that show the azimuthally averaged toroidal magnetic field,  $\bar{B}_\phi(R, \theta, t)$ , near the surface. The cycles were confirmed by applying the FFT (Fast Fourier Transform) to the signal, which in this case is  $\bar{B}_\phi(R, \theta, t)$  near the surface for both the northern and southern hemispheres at mid latitudes.

Set A consists of simulations with  $P_{\text{rot}} = 43$  days. This set can be mainly divided into the low- $\text{Pr}_M$  simulations, for values  $\leq 2$  and high- $\text{Pr}_M$ , for values  $> 2$ . For low- $\text{Pr}_M$ , the simulations present cycles near the surface, which increase their periods with increasing magnetic Prandtl number. Recalling that  $\text{Pr}_M$  is defined as the ratio of  $\nu$  to  $\eta$ , this behaviour of the large-scale dynamo is sensitive to the changes of the diffusivities. As the magnetic diffusion decreases, the magnetic diffusion timescale increases, and it is expected that the dynamo period will increase as well. This has been reported before by Käpylä et al. (2017). Table 4.2.1 is complementary, indicating cycle periods, momentum and magnetic diffusivities, and maximum and minimum values of the azimuthally averaged toroidal magnetic field ( $\bar{B}_\phi$ ).

In the low- $\text{Pr}_M$  regime, simulations A1-A13 show cycles and the azimuthally averaged magnetic field propagates predominantly in the poleward direction, as can be seen in Figures 4.2.2, 4.2.3 and in the first figure of 4.2.4. It is easy to see from the last image that at  $\text{Pr}_M = 2$ , the simulation presents fewer obvious cycles, which begin to disappear in the last 70 years of the simulation. One of the simulations, A5 (bottom in Figure 4.2.2), shows longer cycles predominantly at the northern hemisphere. In this magnetic Prandtl number regime, simulations A8 and A12 do not present large-scale magnetic fields because their magnetic Reynolds number is subcritical. The critical magnetic Reynolds number is the value that  $\text{Re}_M$  must surpass in order for the dynamo to work. Based on the values of  $\text{Re}_M$  given in Table 4.1.1, the critical number for simulation A8 is estimated to be between values greater than 21, and around 54. In the case A12, the critical value is somewhat higher.

The simulations with the higher  $\text{Pr}_M$  in set A (A14 - A16) do no longer show cycles and the dynamo solution is irregular, showing random magnetic field sign reversals. Simulation A14 shows irregular reversals in both hemispheres up to  $\sim 130$  years, then for more than 100 years it does not change its polarity and shows reversals again after that. Simulation A15 also shows irregular reversals on both hemispheres throughout the entire simulation. Finally, simulation A16 presents irregular reversals, too, and its field is more concentrated at the equator (see bottom panel of Figure 4.2.4). This is different in the low- $\text{Pr}_M$  simulations, where the structures spans nearly all latitudes, from the equator to near the poles.

Sim	$\nu$ [m <sup>2</sup> /s]	$\eta$ [m <sup>2</sup> /s]	Pr <sub>M</sub>	Cycles [yrs]	$\bar{B}_\phi^{\max}; \bar{B}_\phi^{\min}$ [kG]
A1	$5.6 \cdot 10^5$	$5.6 \cdot 10^6$	0.1	8.4	13.6; -16.0
A2	$3.9 \cdot 10^6$	$3.9 \cdot 10^7$	0.1	7.3	17.6; -16.0
A3	$1.1 \cdot 10^6$	$5.6 \cdot 10^6$	0.2	7.7	15.8; -13.9
A4	$2.8 \cdot 10^6$	$5.6 \cdot 10^6$	0.5	8.5	12.7; -14.9
A5	$3.9 \cdot 10^6$	$5.6 \cdot 10^6$	0.7	8.6	14.1; -14.0
A6	$2.7 \cdot 10^6$	$3.9 \cdot 10^6$	0.7	8.7	13.9; -15.6
A7	$5.0 \cdot 10^6$	$5.6 \cdot 10^6$	0.9	8.2	14.3; -14.6
A8*	$3.9 \cdot 10^6$	$1.9 \cdot 10^7$	0.2	-	-
A9	$3.9 \cdot 10^6$	$7.8 \cdot 10^6$	0.5	9	14.5; -13.3
A10	$2.8 \cdot 10^6$	$2.8 \cdot 10^6$	1	9.8	14.4; -14.9
A11	$3.9 \cdot 10^6$	$3.9 \cdot 10^6$	1	9	15.2; -14.3
A12*	$5.6 \cdot 10^6$	$5.6 \cdot 10^6$	1	-	-
A13	$5.6 \cdot 10^6$	$2.8 \cdot 10^6$	2	11.3	13.8; -14.3
A14	$5.6 \cdot 10^6$	$1.1 \cdot 10^6$	5	-	10.7; -13.5
A15	$5.6 \cdot 10^6$	$7.8 \cdot 10^5$	7	-	11.9; -11.3
A16	$5.6 \cdot 10^6$	$5.6 \cdot 10^5$	10	-	10.4; -10.4
B1	$2.0 \cdot 10^6$	$4.0 \cdot 10^6$	0.5	7.3	16.3; -16.5
B2	$2.0 \cdot 10^6$	$2.0 \cdot 10^6$	1	-	16.2; -18.4
B3	$2.0 \cdot 10^6$	$1.0 \cdot 10^6$	2	-	14.8; -15.2
B4	$2.0 \cdot 10^6$	$4.0 \cdot 10^5$	5	-	11.2; -14.9
B5	$2.0 \cdot 10^6$	$2.0 \cdot 10^5$	10	-	10.1; -10.1
C1	$1.4 \cdot 10^6$	$1.4 \cdot 10^6$	1	-	16.6; -17.0
C2*	$5.6 \cdot 10^6$	$1.1 \cdot 10^7$	0.5	-	-
C3	$5.6 \cdot 10^6$	$5.6 \cdot 10^6$	1	-	16.6; -16.9
C4	$2.0 \cdot 10^6$	$1.0 \cdot 10^6$	2	-	15.1; -14.9
C5	$2.0 \cdot 10^6$	$4 \cdot 10^5$	5	-	17.0; -17.1
C6	$2.0 \cdot 10^6$	$2.0 \cdot 10^5$	10	-	13.5; -7.9

**Table 4.2.1:** Complementary table. Columns from left to right indicate the momentum diffusivity, magnetic diffusivity, cycle periods if applicable, and the maximum and minimum of  $\bar{B}_\phi$ . Asterisks indicate runs with no dynamo. Part of this table is in Ortiz-Rodríguez et al. Submitted

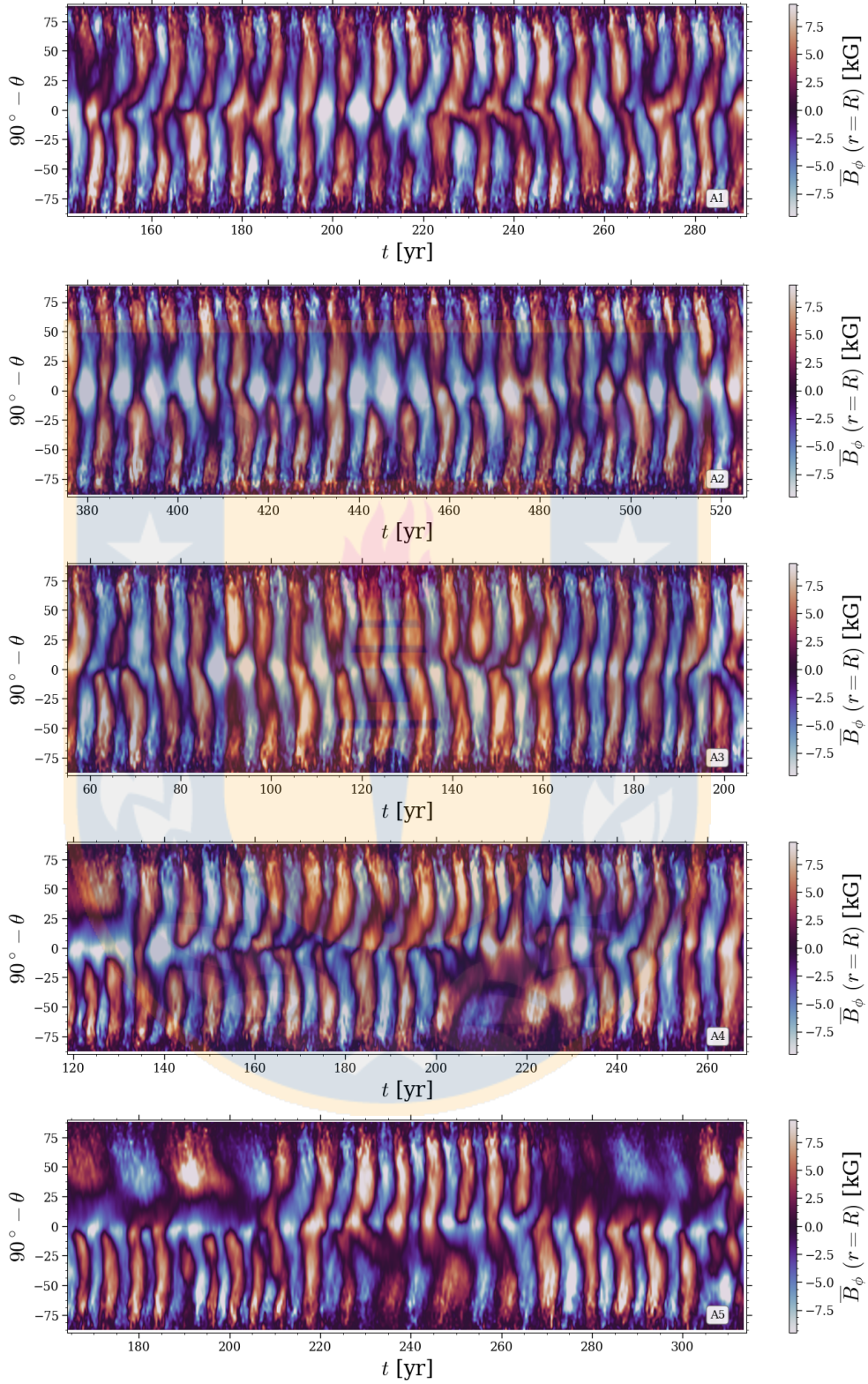


**Figure 4.2.2:** Time evolution of the azimuthally averaged toroidal magnetic field  $\bar{B}_\phi$  near the surface of the star for simulations A1-A5. The colorbar is cut at  $\pm 8$  kG. Figure for simulation A3 is presented as simulation A2 in Ortiz-Rodríguez et al. Submitted

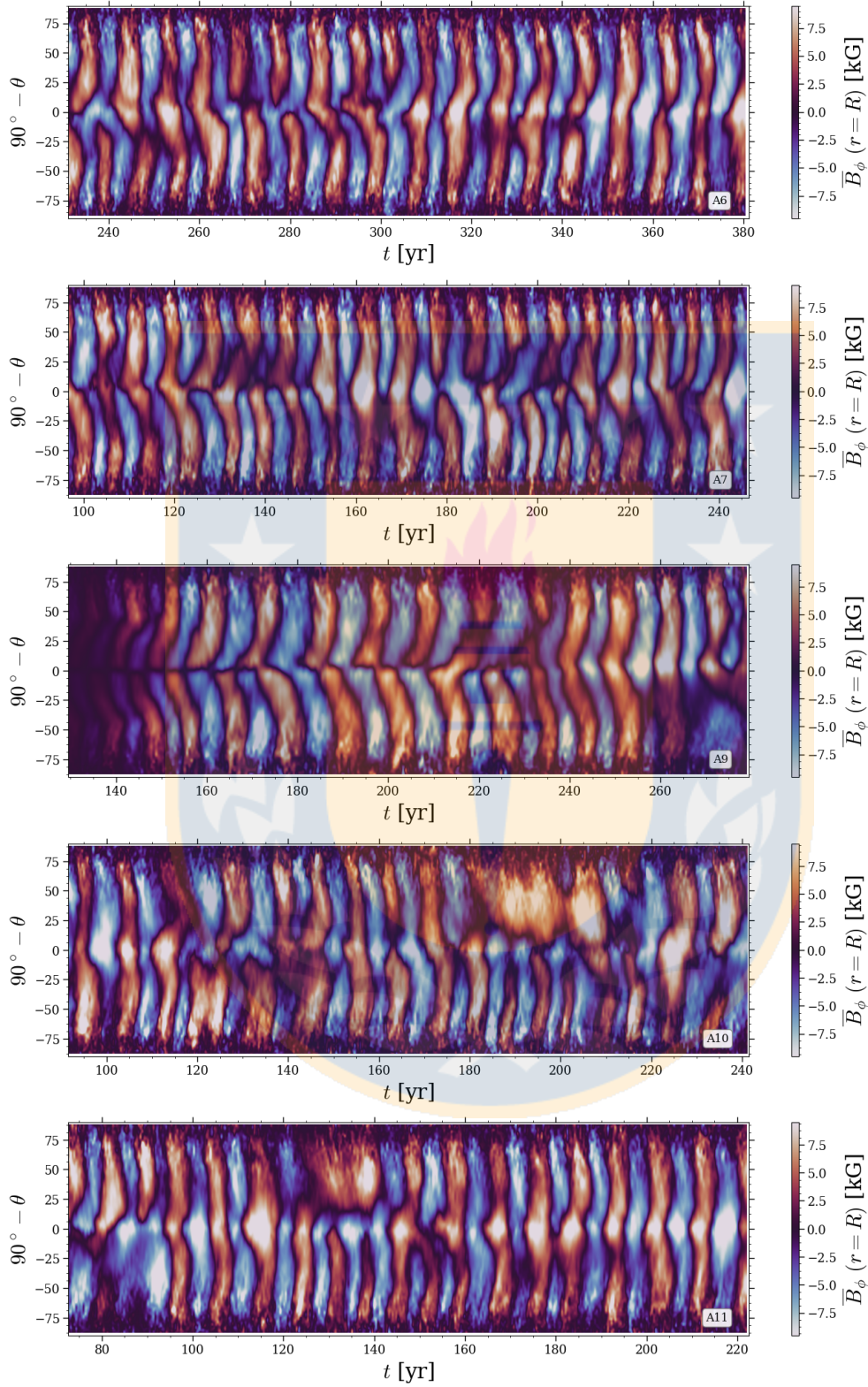


**Figure 4.2.3:** Time evolution of the azimuthally averaged toroidal magnetic field  $\bar{B}_\phi$  near the surface of the star for simulations A6-A11. The colorbar is cut at  $\pm 8$  kG.

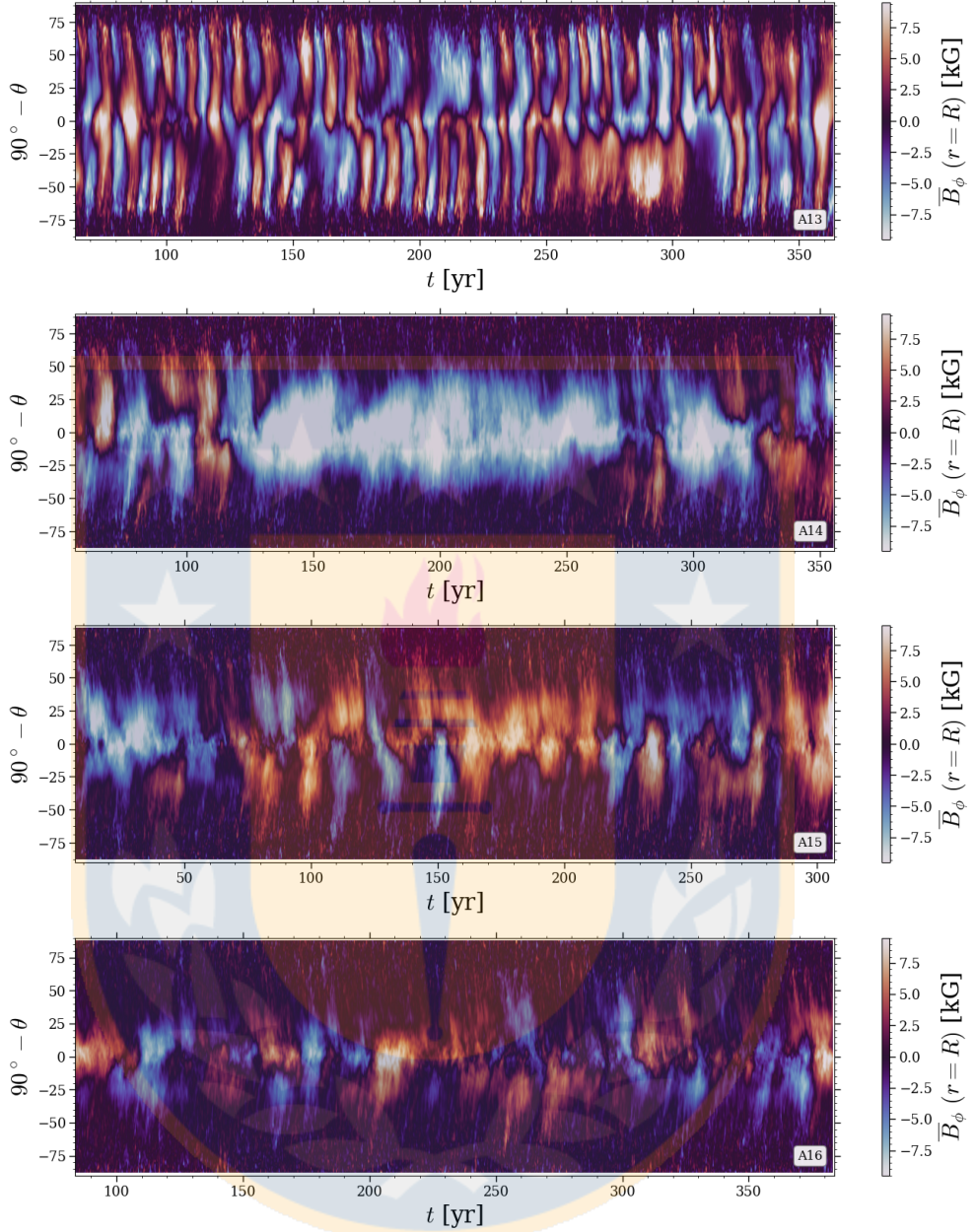


**Figure 4.2.4:** Time evolution of the azimuthally averaged toroidal magnetic field  $\bar{B}_\phi$  near the surface of the star for simulations A13-A16. The colorbar is cut at  $\pm 8$  kG. Figure for simulation A16 is presented as simulation A8 in Ortiz-Rodríguez et al. Submitted.

#### 4.2.1.2 Large-scale magnetic fields at different $P_{\text{rot}}$

Even in the low- $\text{Pr}_M$  regime, cycles do not exist in simulations with longer rotation periods. This is shown in sets B and C. Figures of the magnetic field component  $\bar{B}_\phi$  of set B are presented in Figure 4.2.5. Simulation B1

shows cyclic reversals at the start of the simulation, but random reversals begins to dominate after 400 years. A dipole field is found in simulation B2; in this case it seems to dominate since the beginning of the simulation, but still showing random reversals. In the case of B3, the simulation with  $\text{Pr}_M = 2$ , the dipole is visible, but still there are some random reversals. For instance, in year 70 of the simulation there is a reversal in both hemispheres and four reversals more between 125 to 175 years. Apart from that, the polarity of the magnetic field is predominantly negative (positive) at the northern (southern) hemisphere. Simulation B4 with  $\text{Pr}_M = 5$  shows random reversals that last significantly longer than in the previous simulations, with different polarities in both hemispheres, besides its large structures are concentrated from the equator to nearly  $\pm 70$  degrees. In the case of B5 with  $\text{Pr}_M = 10$ ,  $\bar{B}_\phi$  is predominantly irregular or quasi-stationary. Simulations with  $P_{\text{rot}} = 90$  days do not present random reversals in the low- $\text{Pr}_M$ . From Figure 4.2.6 it can be seen that simulations C1, C3 and C4 and C5 show a dipolar  $\bar{B}_\phi$ , while C6 shows irregular sign reversals with less clear large-scale structures as in B5. Besides, C2 is subcritical, so it does not show large-scale magnetic fields.

For all of the above-mentioned scenarios,  $\text{Re}_M$  increases with  $\text{Pr}_M$ , as expected since they are related, but also the former increases as the rotation rate decreases (see Table 4.1.1). As described before, the dynamo solution is affected not only by  $\text{Pr}_M$ , but also by the rotation period, even when the explored range is small, considering mid and low rotation periods. The importance of the rotation period for magnetic fields in stars is well known, as it was also demonstrated by Käpylä (2021), finding mainly three different dynamo-generated large-scale magnetic fields for slowly, intermediate and rapid rotation, as described in Section 1.2. The transition of axisymmetry at slow rotation to non-axisymmetry at rapid rotation has also been reported by Viviani et al. (2018) for simulations of spherical wedges. In addition to the numerical studies, the relation between stellar rotation rate and magnetic activity (chromospheric emission) was first suggested by Kraft (1967), and demonstrated with observations, e.g., see the work by Noyes et al. (1984); Pizzolato et al. (2003); Astudillo-Defru et al. (2017).

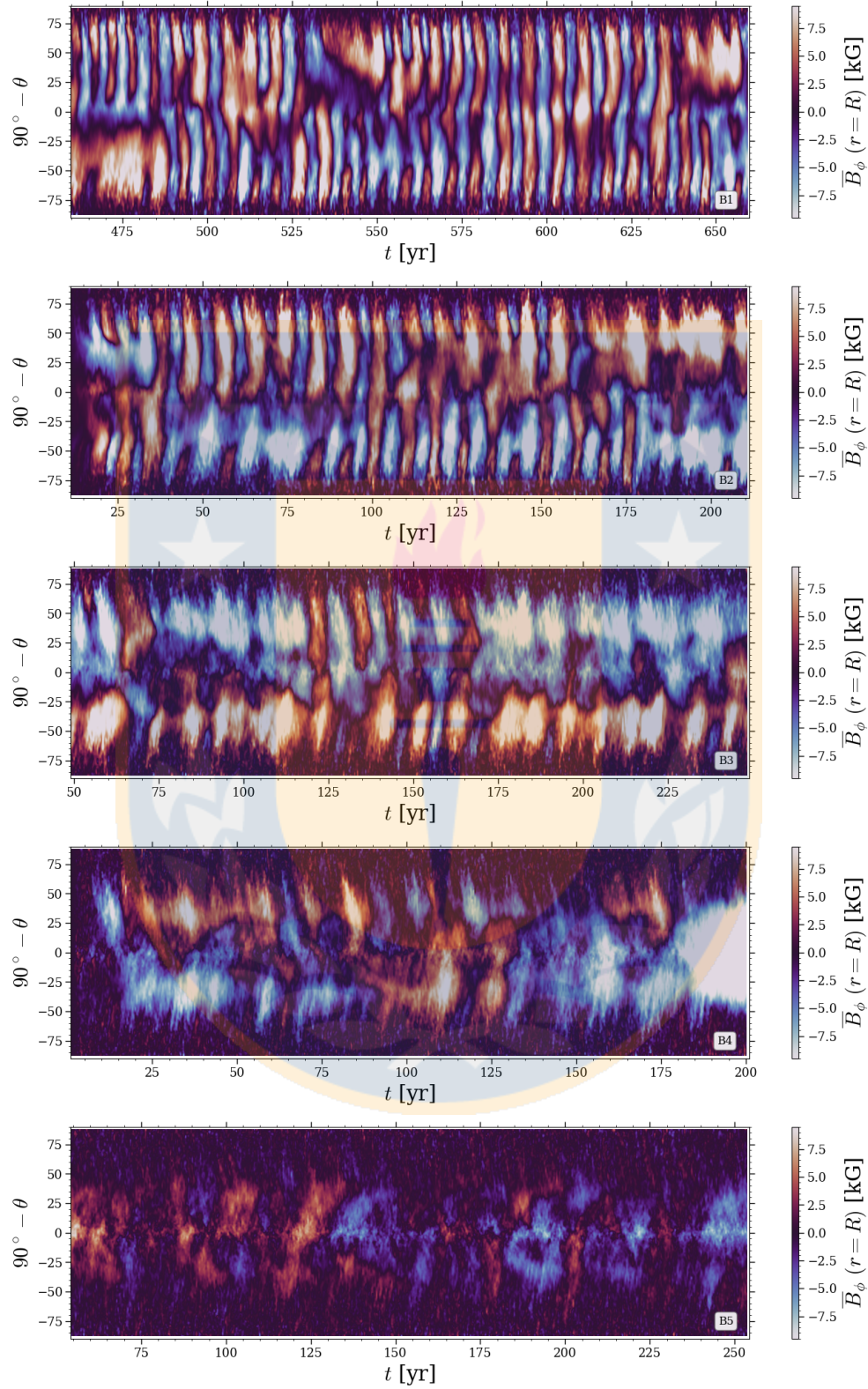


**Figure 4.2.5:** Time evolution of the azimuthally averaged toroidal magnetic field  $\bar{B}_\phi$  near the surface of the star for simulations B1-B5. The colorbar is cut at  $\pm 8$  kG.

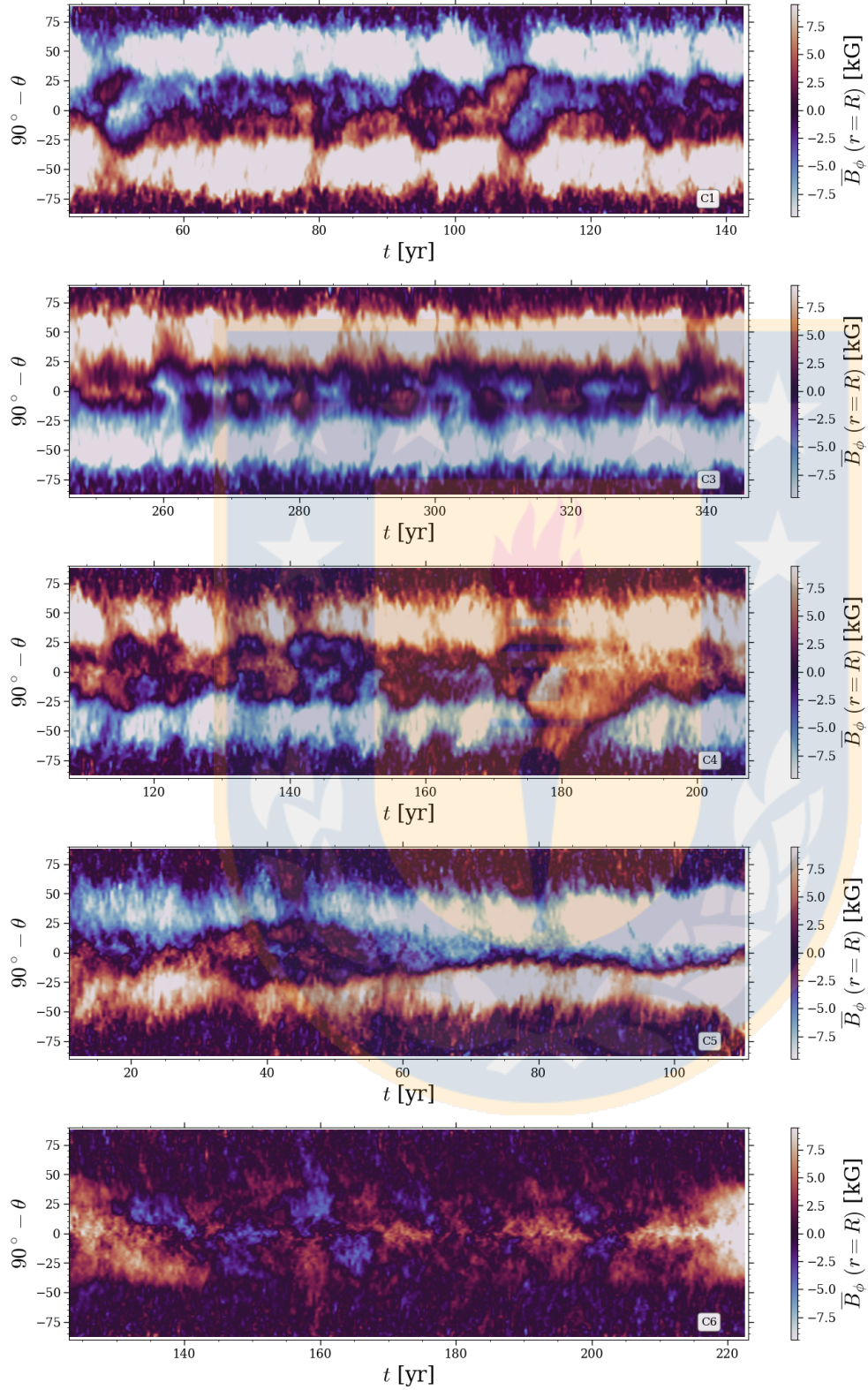


**Figure 4.2.6:** Time evolution of the azimuthally averaged toroidal magnetic field  $\overline{B}_\phi$  near the surface of the star for simulations C1-C6. The colorbar is cut at  $\pm 8$  kG.

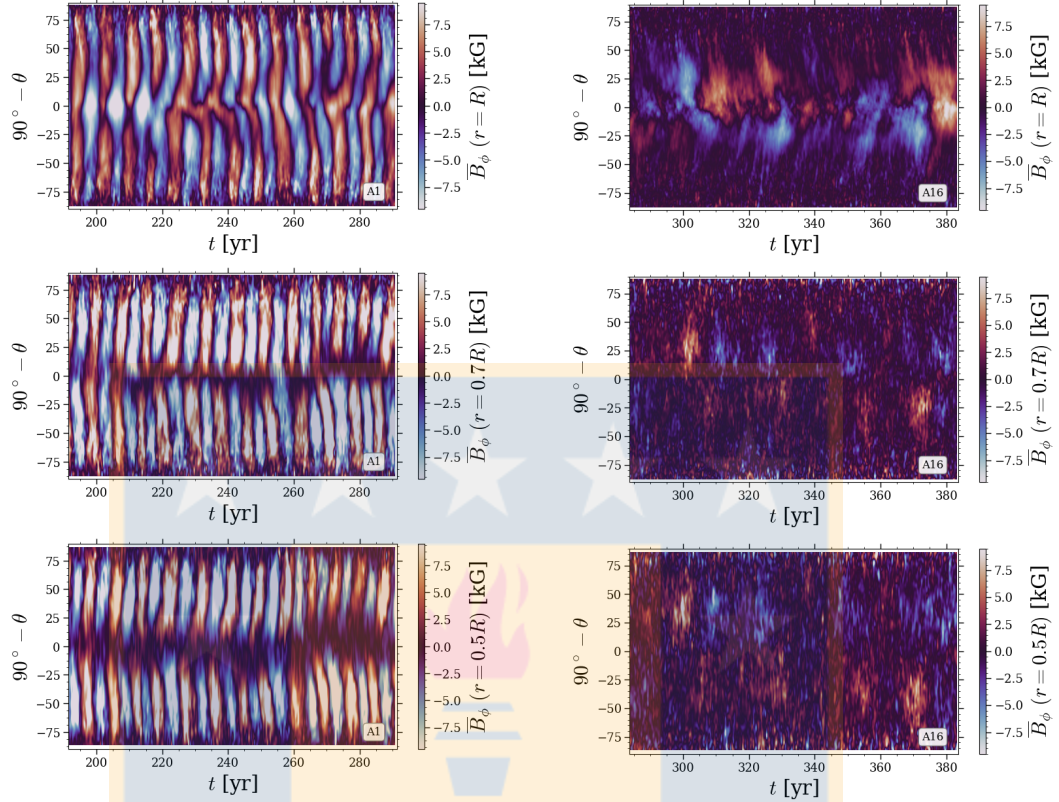


**Figure 4.2.7:** Time evolution of the azimuthally averaged toroidal magnetic field for simulations A1 (left) and A16 (right) at  $r = R$  (top),  $r = 0.7R$  (middle) and  $r = 0.5R$  (bottom).

#### 4.2.1.3 The magnetic field at different stellar radii (depth)

Large scale structures of the magnetic field change with depth. Besides of measuring the field near the surface, it was also analysed at  $r = 0.5R$  and  $r = 0.7R$ . In the case of simulations which show cycles, these cycles are visible at different depth, though the polarity shifts from the surface to the interior of the star. That is, the polarity changes from the surface to 70% of the stellar radius, while subsequently it remains similar in the interior of the star. For the cases with the highest magnetic Prandtl number ( $\text{Pr}_M > 2$ ), the polarity of the azimuthally averaged toroidal magnetic field also changes, and it shows a quasi-stationary dynamo solution in the deeper layers. Figure 4.2.7 shows two representative cases at  $r = 0.5R$ ,  $r = 0.7R$  and near the surface, simulation A1 with  $\text{Pr}_M = 0.1$  and A16 with  $\text{Pr}_M = 10$ , respectively.

#### 4.2.1.4 Radial magnetic field

The radial magnetic field at the surface is presented for some of the simulations. Figure 4.2.8 shows Mollweide projections of the radial magnetic field for simulations of set A (A4, A14 and A16). Run A4 with  $\text{Pr}_M = 0.5$  and  $\text{Re}_M = 54$  presents defined large-scale structures of the magnetic field. As the magnetic Prandtl number and hence the magnetic Reynolds number grow, the large structures become smaller, as shown in the middle panel of Figure 4.2.8 for simulation A14. This simulation has  $\text{Pr}_M = 5$  and  $\text{Re}_M = 208$ , and besides having thinner structures, they also become more intense. The bottom panel of Figure 4.2.8 shows the radial magnetic field for simulation A16. Here, the structures become even smaller, spanning longitudes of around  $15^\circ$ . Figures 4.2.9 and 4.2.10 are the projections of the radial magnetic field for simulations of sets B and C, respectively. In the three sets of simulations the behavior is the same, with the structures becoming smaller with increasing  $\text{Pr}_M$ . Additionally, in the three sets, the structures concentrate more and more at the equator and less at the poles as the Prandtl magnetic number increases.

#### 4.2.1.5 The Proxima Centauri case

The simulations of set C are inspired by Proxima Centauri, a fully convective M 5.5 star with  $P_{\text{rot}} \approx 90$  days. With the star-in-a-box model we were able to adopt that rotation period; nevertheless, in the explored parameter space of the magnetic and fluid Prandtl number, the large-scale magnetic fields do not show an activity cycle as was found with observations by Suárez Mascareño et al. (2016), Wargelin et al. (2017) and Klein et al. (2021). These studies reported an activity cycle of 7 years. However, the simulations of set A present similar activity cycles as shown in Table 4.2.1. We note that Yadav et al. (2016) found an activity cycle of 9 years for a simulation of a fully convective star with the rotation period of Proxima Centauri using a spherical shell that excludes the stellar center. The parameter range used in that work does not fully overlap with the one of this work, for instance, they have  $\text{Pr}_M = 0.1$ , the density stratification is higher in that work, and we used a model for the entire star. In view of the results of Yadav et al. (2016), it seems clear that the dynamo is sensitive to one or more of the different parameters.

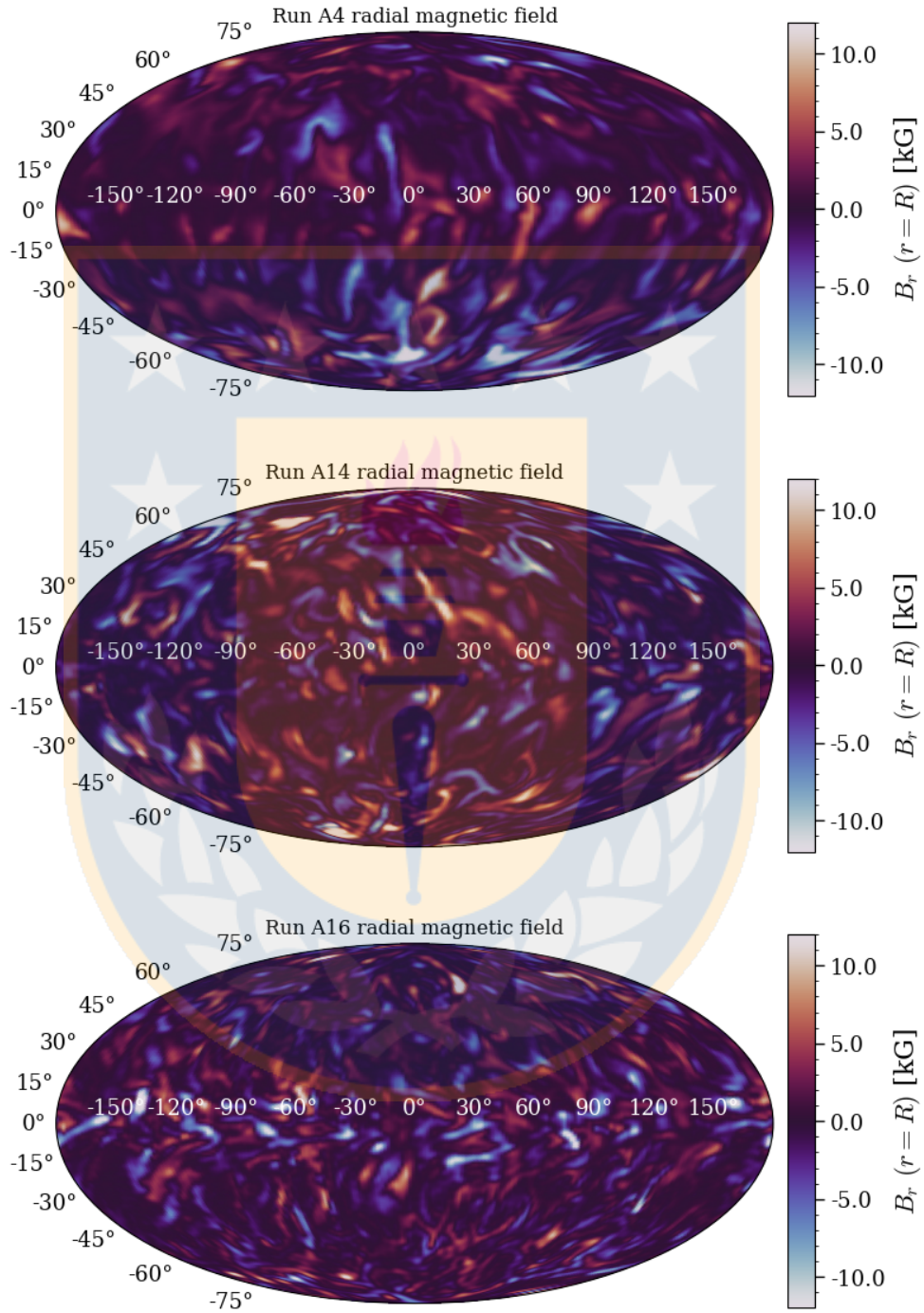


**Figure 4.2.8:** Mollweide projection of the radial magnetic field at the surface for simulations A4, A14 and A16, with  $P_{\text{rot}} = 43$  days. The colorbar is cut at  $\pm 12$  kG.

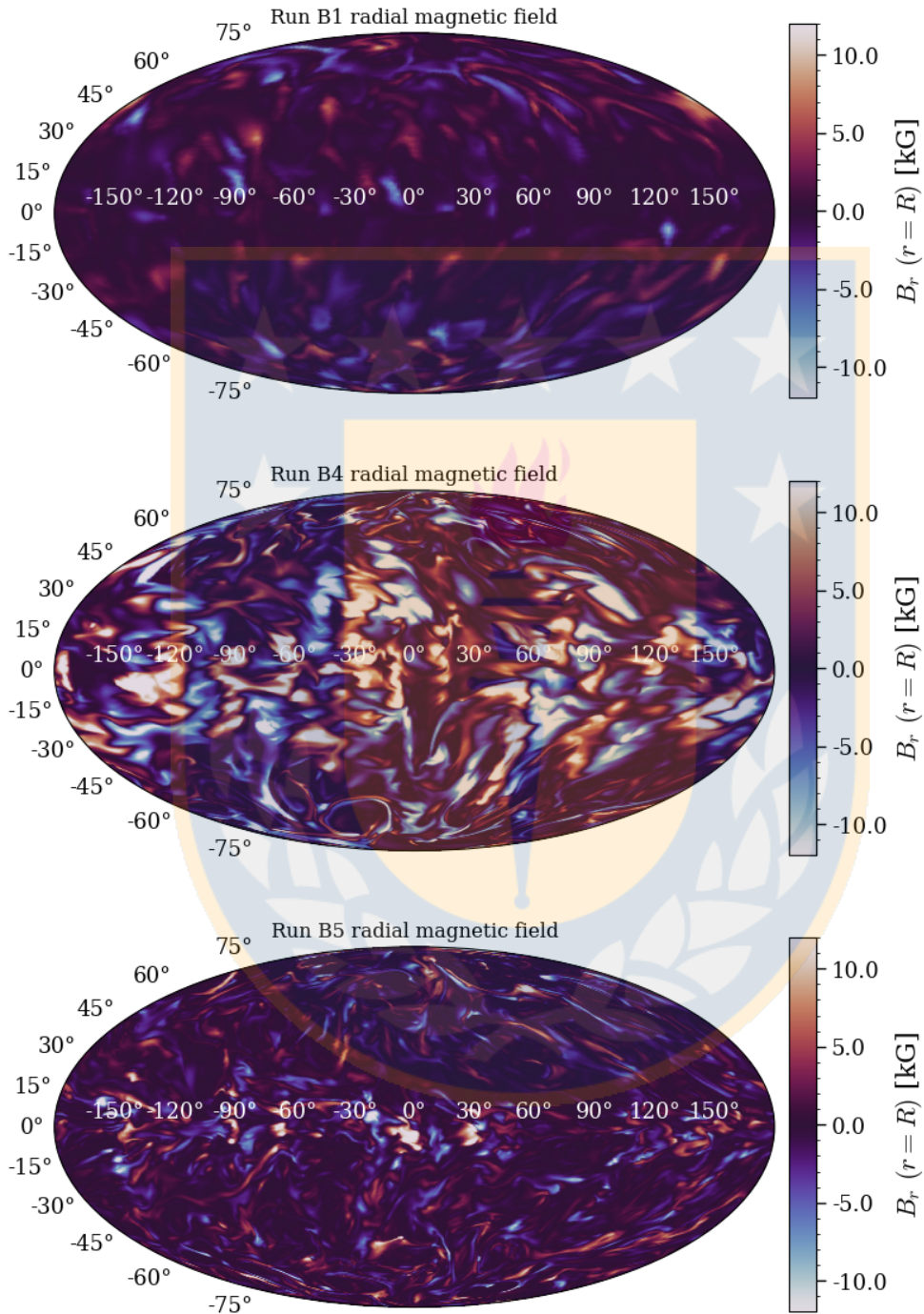


**Figure 4.2.9:** Mollweide projection of the radial magnetic field at the surface for simulations B1, B4 and B5, with  $P_{\text{rot}} = 61$  days. The colorbar is cut at  $\pm 12$  kG.

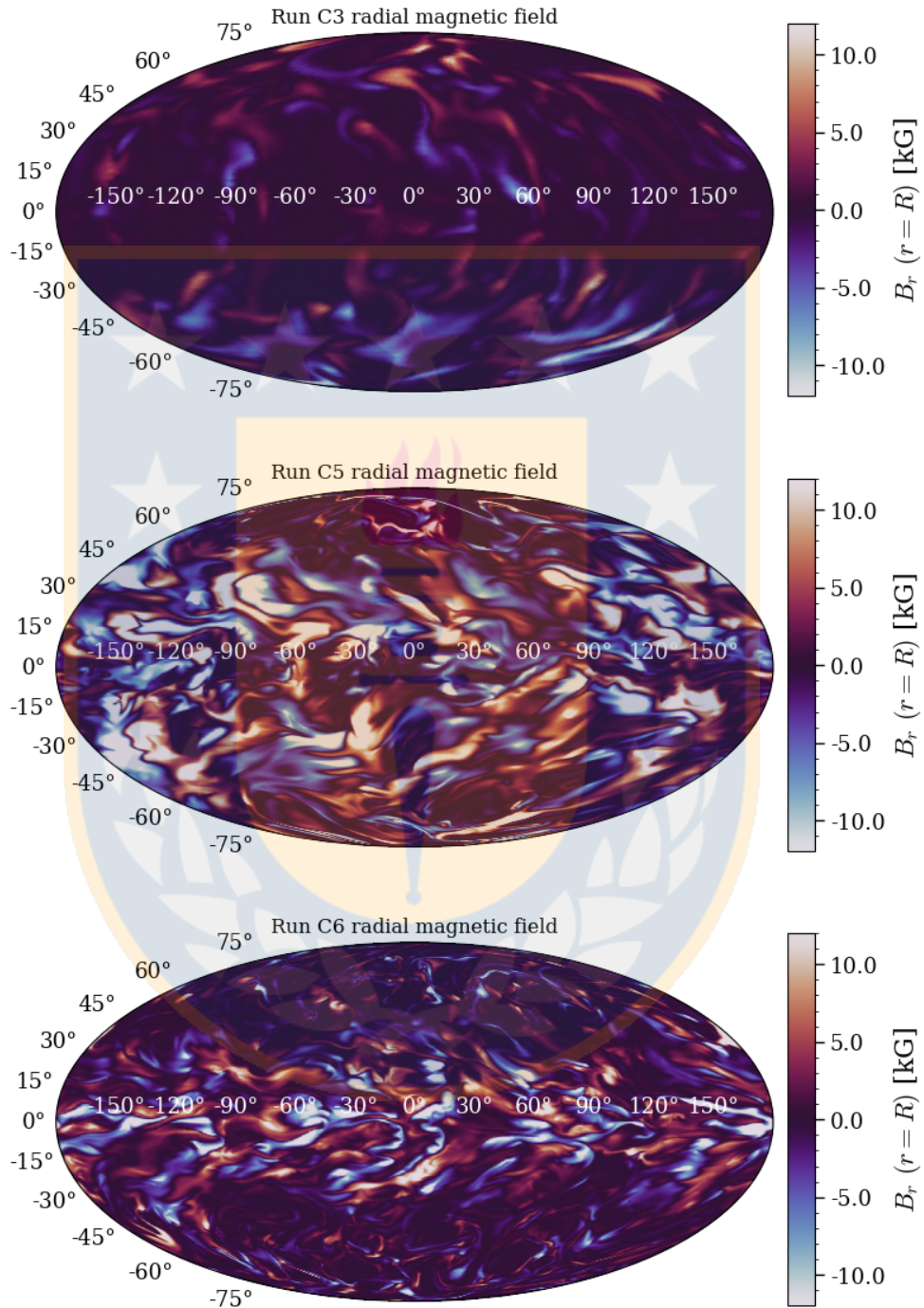


**Figure 4.2.10:** Mollweide projection of the radial magnetic field at the surface for simulations C3, C5 and C6, with  $P_{\text{rot}} = 90$ . The colorbar is cut at  $\pm 12$  kG.

### 4.2.2 Large scale flows

As mentioned in chapter 3, differential rotation is a crucial ingredient for large-scale magnetic fields; it is solar-like (the angular velocity is faster at the equator than at the poles) for all the simulations presented in this work. The averaged rotation rate in cylindrical coordinates can be written as

$$\bar{\Omega}(\varpi, z) = \Omega_0 + \bar{U}_\phi(\varpi, z)/\varpi. \quad (4.2.1)$$

The averaged meridional flow is given as

$$\bar{U}_{\text{mer}}(\varpi, z) = (\bar{U}_\varpi, 0, \bar{U}_z). \quad (4.2.2)$$

The angular velocity varies with depth as well as with latitude. This can be quantified with the amplitude of the radial  $\Delta_\Omega^{(r)}$  and latitudinal differential rotation  $\Delta_\Omega^{(\bar{\theta})}$ , which are given as

$$\Delta_\Omega^{(r)} = \frac{\bar{\Omega}_{\text{top,eq}} - \bar{\Omega}_{\text{bot,eq}}}{\bar{\Omega}_{\text{top,eq}}}, \quad (4.2.3)$$

$$\Delta_\Omega^{(\bar{\theta})} = \frac{\bar{\Omega}_{\text{top,eq}} - \bar{\Omega}_{\text{top,\bar{\theta}}}}{\bar{\Omega}_{\text{top,eq}}}, \quad (4.2.4)$$

where the subscripts indicate depth and latitude, respectively, "top" corresponding to  $0.9 R$ , "bot" corresponding to  $0.1 R$ , eq stands for the equator ( $\theta = 0^\circ$ ) and  $\bar{\theta}$  stands for an average of  $\bar{\Omega}$  for latitudes  $+\theta$  and  $-\theta$ . Note that  $\Delta_\Omega^{(r)}$  and  $\Delta_\Omega^{(\bar{\theta})}$  are in spherical coordinates.

Table 4.2.2 lists the values of  $\Delta_\Omega^{(r)}$  and  $\Delta_\Omega^{(\bar{\theta})}$  for the three sets of simulations. The solar-like differential rotation is indicated by the positive values of the amplitudes of the differential rotation. The amplitude of the radial differential rotation decreases with increasing magnetic Prandtl number in set A (see second column of Table 4.2.2.) This can also be seen from Figure 4.2.11 that shows the rotation profiles for simulations A1, A13, A14 and A16 with magnetic Prandtl numbers of 0.1, 2, 5 and 10, respectively. Simulations A1, A13 and A14 have positive amplitudes of both the radial and latitudinal differential rotation, which is evident in the rotation profiles of Figure 4.2.11. Simulation A16 exhibits positive values for the amplitude of the latitudinal differential rotation

and negative values for the amplitude of the radial differential rotation, as illustrated in the bottom left panel of Figure 4.2.11 where the angular velocity does not change significantly with depth.

Sim	$\Delta_{\Omega}^{(r)}$	$\Delta_{\Omega}^{(\theta)}(60^{\circ})$	$\Delta_{\Omega}^{(\theta)}(75^{\circ})$	$\bar{u}_{mer}^{rms}[\text{m/s}]$
A1	0.13	0.038	0.044	0.54
A2	0.13	0.035	0.044	0.35
A3	0.13	0.039	0.046	0.56
A4	0.15	0.044	0.054	0.58
A5	0.17	0.052	0.063	0.61
A6	0.12	0.037	0.049	0.34
A7	0.14	0.041	0.052	0.58
A8*	0.28	0.100	0.100	0.75
A9	0.18	0.060	0.069	0.60
A10	0.14	0.036	0.048	0.57
A11	0.12	0.036	0.046	0.55
A12*	0.23	0.092	0.091	0.70
A13	0.11	0.037	0.046	0.34
A14	0.020	0.018	0.019	0.38
A15	0.015	0.023	0.025	0.39
A16	-0.006	0.019	0.017	0.33
B1	0.067	-0.006	-0.020	0.40
B2	0.062	-0.009	-0.023	0.70
B3	-0.029	0.041	0.043	0.52
B4	0.100	0.062	0.076	0.47
B5	-0.029	0.041	0.043	0.32
C1	0.12	0.10	0.12	0.52
C2	0.087	0.067	0.060	0.20
C3	0.008	-0.043	-0.069	0.42
C4	0.052	0.095	0.101	0.50
C5	-0.013	0.086	0.078	0.46
C6	-0.058	0.064	0.063	0.36

**Table 4.2.2:** Amplitude of the temporally and azimuthally averaged angular velocity  $\bar{\Omega}(r, \theta)$ . From left to right the columns indicate the name of the simulation, the amplitude of the radial differential rotation, the amplitude of the latitudinal differential rotation at  $60^{\circ}$  and  $75^{\circ}$ , and the rms value of the meridional flow speed.

The simulations presented here have Coriolis numbers ranging from 3 to 14. Therefore it is consistent to obtain solar-like differential rotation as in the first simulations presented with this version of the setup by Käpylä (2021),

where the transition from antisolar to solar-like differential rotation takes place for Coriolis numbers between 0.7 and 2. This is also in agreement with the simulations of spherical shell convection by [Viviani et al. \(2018\)](#), where the transition takes place around  $Co = 3$ . Simulation C2 has the lowest Coriolis number of the three sets; it has no dynamo, though it might be used to compare with simulations that have. In this regard, [Figure 4.2.12](#) shows the rotation profiles for simulations A8 and C2. They show that a faster angular velocity spans broader latitudinal range and smaller radial one compared to the simulations with dynamo. This shows the effect of magnetic fields on the differential rotation.

The streamlines in [Figures 4.2.11](#) and [4.2.12](#) indicate the mass flux due to meridional circulation, a mechanism that is partly responsible for redistributing the angular momentum within the convection zone. In the low- $Pr_M$  ( $Pr_M < 2$ ) regime in our simulations, the streamlines are composed of multiple small cell, while in the highest  $Pr_M$  the pattern is composed of 2 to 3 large cells, which are symmetric with respect to the equator (see bottom panels of [Figure 4.2.11](#)). For simulations of sets B and C the flow cells are similar to those of set A. The amplitude of the meridional flow velocity ( $\bar{U}_{mer}^{max}$ ) is indicated in the lower right corner of each panel in that Figure, as well as for [Figure 4.2.12](#).  $\bar{U}_{mer}^{max}$  is 2.7, 3.7, 2.2 and 1.5 m/s, for simulations A1, A13, A14 and A16, respectively. The values of  $\bar{U}_{mer}^{max}$  are very large, corresponding to 20 (A16) to 40% (A13) of the overall rms velocity. The rms value of the meridional velocity is given in the fifth column of [Table 4.2.2](#). In the case of simulations A8, A12 and C2, the meridional circulation also has multiple cell patterns.

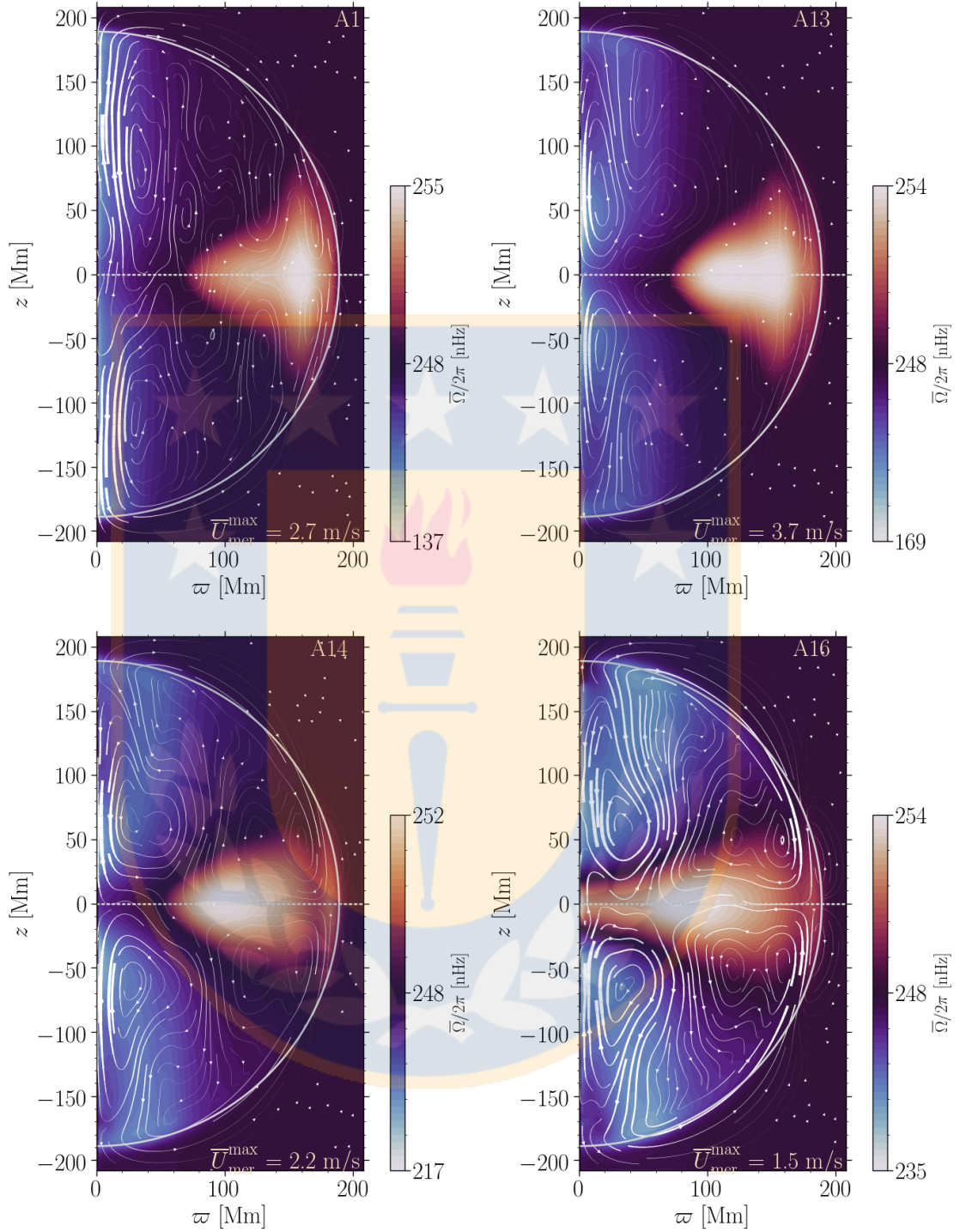


**Figure 4.2.11:** Temporally and azimuthally averaged angular velocity  $\bar{\Omega}(\omega, z)$  for simulations A1 (top left), A13 (top right), A14 (bottom left) and A16 (bottom right). The streamlines show the meridional flow and its amplitude is indicated in the lower right corner. The surface is indicated by the gray line while the equator is indicated by the gray dotted line.

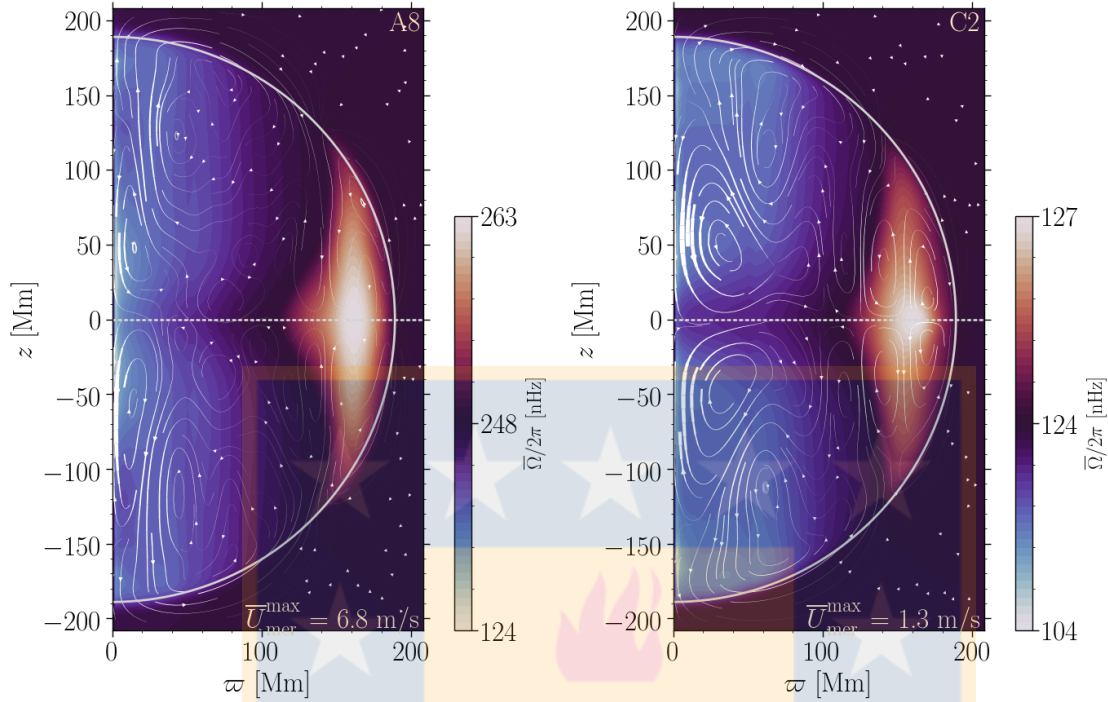


**Figure 4.2.12:** Temporally and azimuthally averaged angular velocity  $\bar{\Omega}(\omega, z)$  for simulations A8 and C2, which do not have dynamo. The streamlines show the meridional flow and its amplitude it is indicated in the lower right corner. The surface is indicated by the gray line while the equator is indicated by the gray dotted line.

For the three sets of simulations, the kinetic helicity,  $\mathcal{H} = \overline{\boldsymbol{\omega} \cdot \boldsymbol{U}}$ , is negative (positive) in the northern (southern) hemisphere, as shown in Figure 4.2.13 for simulations A13, B3 and C4 with  $\text{Pr}_M = 2$ . This, with  $\frac{\partial \bar{\Omega}}{\partial r} > 0$ , is associated with a poleward propagating dynamo wave (Parker, 1955; Yoshimura, 1975), which is most noticeable for the simulations of set A.

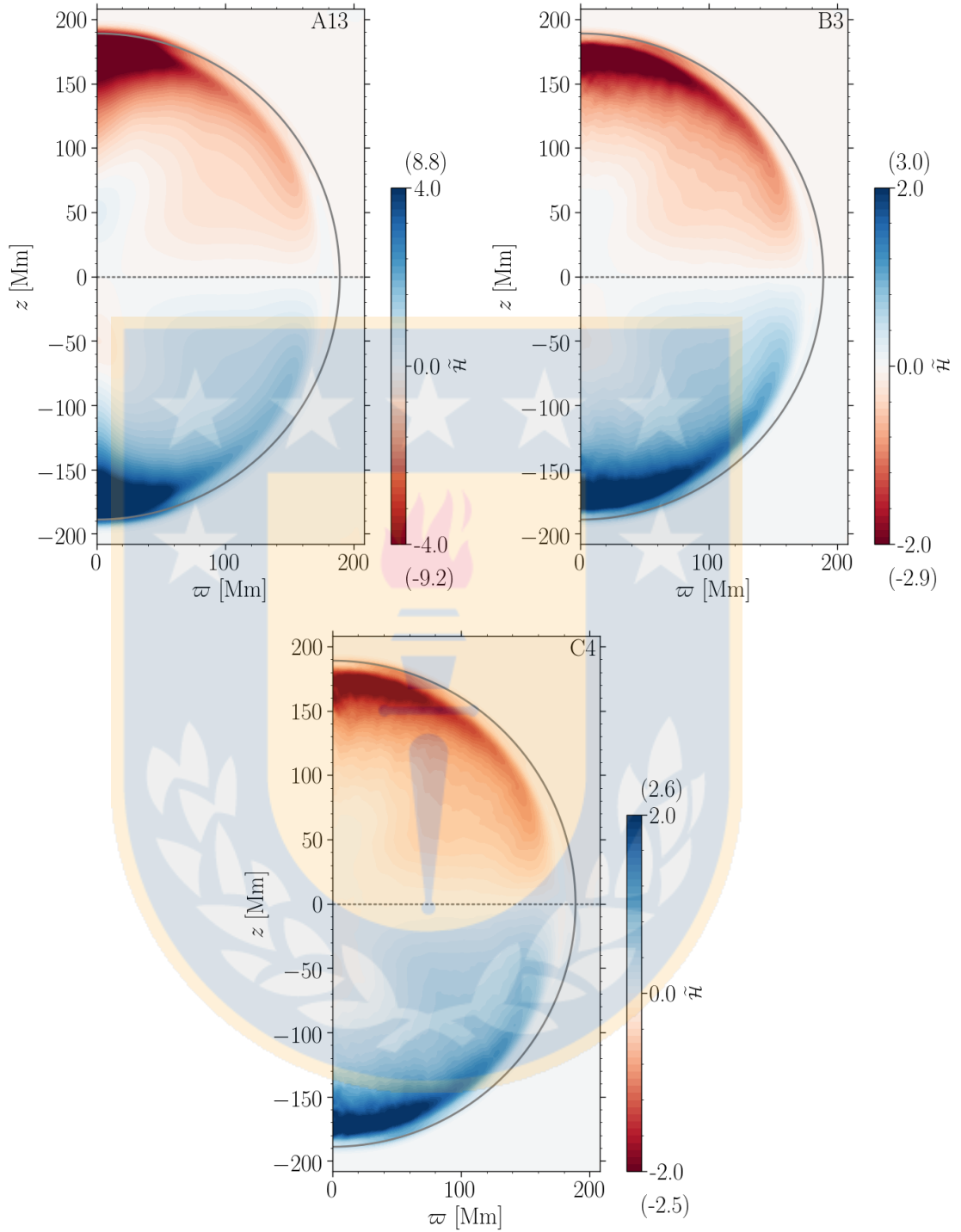


**Figure 4.2.13:** Azimuthally averaged normalised kinetic helicity  $\tilde{\mathcal{H}} = \mathcal{H}(\varpi, z)/u_{\text{rms}}\omega_{\text{rms}}$  for simulations A13 (top left) with  $P_{\text{rot}} = 43$  days, B3 (top right) with  $P_{\text{rot}} = 61$  days, and C4 (bottom) with  $P_{\text{rot}} = 90$  days, one for each rotation period with  $\text{Pr}_M = 2$ .

### 4.2.3 Energies as function of $\text{Pr}_M$

The energies of the simulations are summarized in table 4.2.3. The magnetic energy  $E_{\text{mag}}$  in the three sets of simulations are of the order of  $10^5$  [ $\text{J m}^{-3}$ ]. One might anticipate that  $E_{\text{mag}}$  rises with increasing  $\text{Re}_M$  ( $\text{Pr}_M$ ), as observed in the work by Käpylä et al. (2017) using simulations of spherical shells. However, the magnetic energy in the saturated regime should also be determined by the inertial and Lorentz force balance. In that sense, there is no apparent pattern in the simulations provided here in terms of the variation of  $E_{\text{mag}}$ . For the kinetic energy  $E_{\text{kin}}$  it is more obvious, as it decreases as  $\text{Re}_M$  increases. This can be explained because at large  $\text{Pr}_M$  the kinetic energy is turned into magnetic energy more efficiently. Then, the ratio  $E_{\text{mag}}/E_{\text{kin}}$  grows as the magnetic Prandtl number increases. The energy density of the differential rotation,  $E_{\text{kin}}^{\text{DR}}$ , also decreases with increasing  $\text{Pr}_M$ . Furthermore, as the rotation period increases,  $E_{\text{kin}}^{\text{DR}}$  decreases sharply for high- $\text{Pr}_M$  (see the third column of table 4.2.3).

In the simulations A8, A12 and C2 where there is no dynamo the magnetic fields are negligibly small, while their kinetic energy is of the same order of magnitude as some of the simulations where there is dynamo. This is due to the magnetic field not being strong enough to back react and damp the flow through the Lorentz force. This is analogous to what happens in the kinematic regime of simulations that have dynamos. The top panels of Figures 4.2.14 and 4.2.15 show the evolution of the magnetic and kinetic energy densities in both the kinematic and saturated regime for simulation A4. The kinematic regime in which the magnetic energy grows exponentially lasted around 80 years in this simulation. From Figure 4.2.14 it can be seen that the kinetic energy density is about 6 orders of magnitude larger than the magnetic energy at the beginning of the simulation, a gap that decreases with time. In the saturated regime, the kinetic and magnetic energy densities become comparable (see top panel of Figure 4.2.15), with the kinetic energy density being approximately 1.5 times the magnetic energy density.

In addition to the changes of the large-scale magnetic field with changing  $\text{Pr}_M$ , the kinematic regime also experiences changes, i.e., the growth of the magnetic field is faster with increasing magnetic Prandtl number, implying that the

kinematic regime is shorter. The bottom panels of Figures 4.2.14 and 4.2.15 show the kinematic and saturated regime of simulation A16, respectively. The kinematic regime in this simulation lasts about 7 years. In the saturated regime, the kinetic energy density is slightly reduced, and the magnetic energy density is higher by a factor of  $\sim 1.8$ . This transition where the magnetic energy density is higher than the kinetic energy density in the saturated regime occurs at  $\text{Pr}_M \sim 2$  for sets A and B, and at  $\text{Pr}_M \sim 5$  for set C. Browning (2008) reported a similar behaviour of the magnetic and kinetic energy densities in simulation of fully convective stars with solar rotation rate. Simulation Cm of that work with  $\text{Pr}_M = 8$  presents a  $E_{\text{mag}}$  of about 1.2 times  $E_{\text{kin}}$ , while in Cm2 with  $\text{Pr}_M = 5$ ,  $E_{\text{mag}}$  does not overcome  $E_{\text{kin}}$ . In all simulations of the present work, the energy densities show fluctuations, but no systematic variation is observed.

The azimuthally averaged toroidal and poloidal magnetic fields are also analysed. The energy density of the toroidal magnetic field in general decreases with increasing magnetic Prandtl number, being up to 30% of the total magnetic energy density,  $E_{\text{mag}}$ . On the other hand, the poloidal field is less than 10% of the total magnetic energy density for all simulations. Just in one case, simulation B1, its  $E_{\text{mag}}^{\text{pol}}$  is twice the corresponding  $E_{\text{mag}}^{\text{tor}}$ .

The energy densities for differential rotation  $E_{\text{kin}}^{\text{DR}}$  and meridional circulation  $E_{\text{kin}}^{\text{MC}}$  are also calculated for all simulations. It is clear from Table 4.2.3 that the ratio of  $E_{\text{kin}}^{\text{DR}}$  to  $E_{\text{kin}}$  decreases with increasing magnetic Prandtl number. In simulations A8, A12 and C2, where there is no dynamo, the magnetic field is weak,  $E_{\text{kin}}^{\text{DR}}$  is almost 0.6 times  $E_{\text{kin}}$ . Furthermore,  $E_{\text{kin}}^{\text{DR}}$  is approximately 5 times greater in the simulations with no dynamo than in cases with dynamos. Then, in the parameter range investigated in this study, magnetic fields contribute to the quenching of the differential rotation. This is in agreement with the work of Browning (2008).

The energy density of the meridional circulation varies little amongst the three sets, being roughly 1-3% of its respective  $E_{\text{kin}}$ . Simulation C2 is an outlier, with  $E_{\text{kin}}^{\text{MC}}$  being 12% of its  $E_{\text{kin}}$ , and up to  $\sim 30$  times greater than in the other cases.

Sim	$E_{\text{mag}}$	$E_{\text{mag}}^{\text{tor}}/E_{\text{mag}}$	$E_{\text{mag}}^{\text{pol}}/E_{\text{mag}}$	$E_{\text{kin}}$	$E_{\text{kin}}^{\text{DR}}/E_{\text{kin}}$	$E_{\text{kin}}^{\text{MC}}/E_{\text{kin}}$
A1	7.3	0.23	0.07	8.47	0.23	0.01
A2	7.6	0.20	0.06	8.49	0.27	0.02
A3	7.06	0.24	0.06	8.24	0.24	0.06
A4	5.59	0.20	0.06	8.66	0.31	0.02
A5	4.2	0.24	0.06	10.23	0.34	0.02
A6	6.46	0.21	0.05	7.62	0.31	0.02
A7	5.72	0.25	0.06	8.36	0.31	0.02
A8*	-	-	-	20.16	0.55	0.01
A9	4.58	0.28	0.07	11.62	0.32	0.02
A10	6.26	0.16	0.04	8.08	0.32	0.02
A11	5.78	0.20	0.05	7.35	0.30	0.02
A12*	-	-	-	16.27	0.54	0.02
A13	6.5	0.15	0.04	4.5	0.32	0.02
A14	7.21	0.07	0.03	4.28	0.16	0.02
A15	6.65	0.14	0.02	4.54	0.14	0.02
A16	6.86	0.03	0.02	3.93	0.10	0.01
B1	4.94	0.02	0.04	10.81	0.33	0.02
B2	5.82	0.16	0.03	10.79	0.38	0.02
B3	7.22	0.11	0.03	8.95	0.30	0.02
B4	8.45	0.06	0.02	6.95	0.22	0.02
B5	7.24	0.03	0.02	6.36	0.014	0.01
C1	7.67	0.17	0.03	11.43	0.31	0.03
C2*	-	-	-	19.87	0.14	0.12
C3	3.64	0.34	0.03	12.68	0.44	0.02
C4	7.73	0.12	0.03	9.54	0.25	0.03
C5	11.9	0.10	0.03	6.88	0.19	0.03
C6	7.38	0.04	0.02	6.90	0.16	0.02

**Table 4.2.3:** The energies are given in units of  $10^5 \text{ J m}^{-3}$ . From left to right the columns indicate: the magnetic energy density is  $E_{\text{mag}} = \langle \mathbf{B}^2/2\mu_0 \rangle$ , the brackets indicate volume average within the radius of the star. The kinetic energy density is  $E_{\text{kin}} = \frac{1}{2}\langle \rho \mathbf{U}^2 \rangle$ . The energy density for the azimuthally averaged toroidal and poloidal field are given by  $E_{\text{mag}}^{\text{tor}} = \overline{B}_\phi^2/2\mu_0$ , and  $E_{\text{mag}}^{\text{pol}} = (\langle \overline{B}_\omega^2 + \overline{B}_z^2 \rangle)/2\mu_0$ , respectively. The energy density for the differential rotation and meridional circulation are given by are given by  $E_{\text{kin}}^{\text{DR}} = \frac{1}{2}\langle \rho \overline{U}_\phi^2 \rangle$ , and  $E_{\text{kin}}^{\text{MC}} = (\langle \overline{U}_\omega^2 + \overline{U}_z^2 \rangle)/2\mu_0$ , respectively. Asterisks indicate runs with no dynamo.

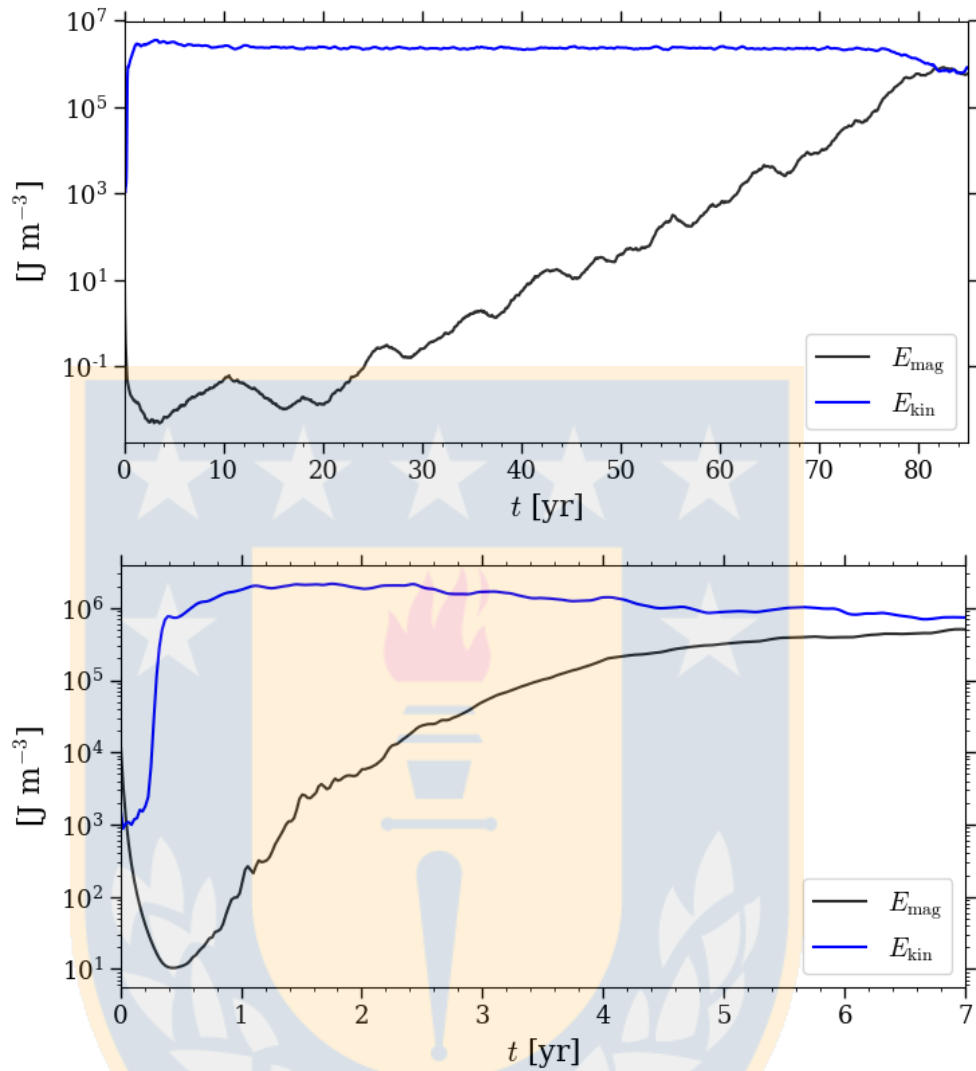


**Figure 4.2.14:** Time evolution of the kinetic and magnetic energy densities in the kinematic regime for simulations A4 (top) and A16 (bottom).

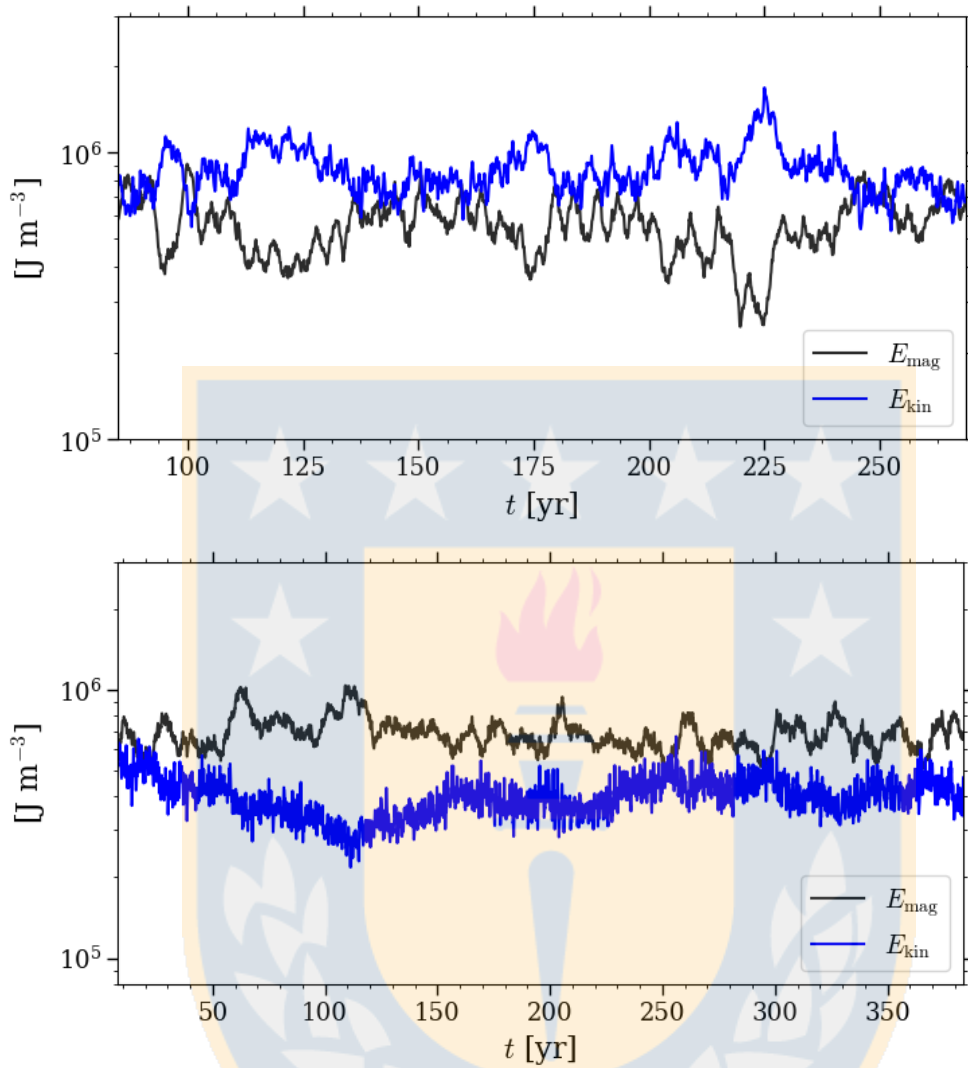


**Figure 4.2.15:** Time evolution of the kinetic and magnetic energy densities in the saturated regime for simulations A4 (top) and A16 (bottom).

#### 4.2.4 Spherical harmonic decomposition

As mentioned in Section 2.3, dynamos are found to operate at large scales and at small scales as well. Small-scale dynamos produce magnetic fields that are of the order of the typical scale of the energy-containing eddies or even smaller. Small-scale magnetic fields are found in many astrophysical systems. In the case of the Sun, small-scale magnetic fields are thought to be produced by the small-scale dynamo (Solanki, 1993; Martínez Pillet, 2013; Borrero et al., 2017). In the case of M dwarfs, small-scale magnetic fields have been studied observationally, e.g., by Kochukhov and Lavail (2017), where they found that most of the magnetic energy is concentrated on small scales, and also numerically (Yadav et al., 2015). Some works with numerical simulations have not been able to reproduce both large scale and small scale magnetic fields simultaneously, because they were not able to resolve small-scale motions (Browning, 2008).

In order to study whether we may have small structures of the magnetic field in the simulations presented here, a good instrument to use is the Spherical Harmonic decomposition, since it can represent magnetic fields in term of different modes. Spherical harmonics originate from solving Laplace's equation in spherical coordinates. The spherical harmonic decomposition used here was for the radial magnetic field,  $B_r$ .

We consider a function  $f = f(\theta, \phi)$  that can be written as

$$f(\theta, \phi) = \sum_{l=0}^{l_{\max}} \sum_{m=-l}^l \tilde{f}_l^m(\theta, \phi) Y_l^m(\theta, \phi), \quad (4.2.5)$$

where

$$\tilde{f}_l^m = \int_0^{2\pi} \int_0^\pi f(\theta, \phi) Y_l^{m*} \sin \theta d\theta d\phi. \quad (4.2.6)$$

For the radial magnetic field  $B_r(\theta, \phi)$ , we consider the condition (see Krause and Rädler 1980)

$$B_{r,l}^{-m} = (-1)^m B_{r,l}^{m*}. \quad (4.2.7)$$

Then, the spherical harmonics is given as

$$B_r(\theta, \phi) = \sum_{l=1}^{l_{\max}} B_{l,r}^0 Y_l^0 + 2\text{Re} \left( \sum_{l=1}^{l_{\max}} \sum_{m=1}^l B_{l,r}^m Y_l^m \right). \quad (4.2.8)$$

Because of the solenoidality of the magnetic field there is no contribution to the magnetic field for  $l = 0$ , therefore this term has been dropped.

With this method we are able to measure the energy contained in these modes. Low-order modes represent large-scale structures of the magnetic field, and the higher modes correspond to the smaller structures. The total radial magnetic energy density near the surface and the radial magnetic energy density for specific modes  $m = 0, 1, 2$ , as well as the energy density contained in the higher modes, which are considered small-scale fields, are given in Table 4.2.4. The energy contained in the non-axisymmetric modes  $m = 3, 4, 5, \dots, 10$  are not listed there. The mode  $m = 0$  corresponds to the axisymmetric part of the radial magnetic field, the modes  $m = 1$  and  $m = 2$  correspond to the first and the second non-axisymmetric modes, respectively. Additionally,  $l, m \geq 10$  were considered as the small-scale fields. This was done for selected simulations of each set. For all the cases, the  $m = 0$  mode is dominant, while the non-axisymmetric modes  $m = 1$  and  $m = 2$  are subdominant. This was reported before by Viviani et al. (2018), where their slowly rotating simulations were the ones with non-axisymmetric magnetic field being subdominant. As shown in the last column of Table 4.2.4, the magnetic energy density contained in  $l, m > 10$ , corresponding to the non-axisymmetric small-scale magnetic field, is 2 to 3 orders of magnitudes lower than the dominant mode  $m = 0$ .

The top left panel of Figure 4.2.16 presents a reconstruction of the radial magnetic field near the surface of simulation B4 using the first 10 ( $0 < l \leq 10$ ) spherical harmonics with the aim to show that large-scale structures are concentrated at low spherical harmonics. The top right panel shows a reconstruction of  $B_r$  considering  $0 < l \leq 100$ , and the bottom panel shows the radial magnetic field from the original data (same as in Figure 4.2.9). This shows that the spherical harmonic decomposition works well. The reconstruction of the magnetic field via spherical harmonic decomposition has been done for the three sets of simulations.

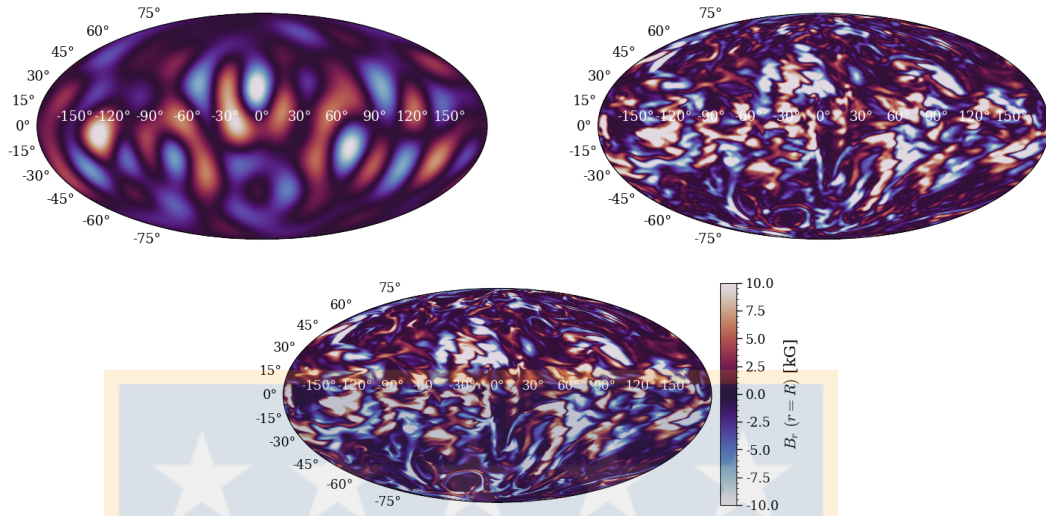


**Figure 4.2.16:** Radial magnetic field near the surface of the star reconstructed via spherical harmonic decomposition and real data. The top left figure is the reconstruction of the radial magnetic field using  $0 < l \leq 10$ , the top right panel is the reconstruction of the radial magnetic field using  $0 < l \leq 100$ , and the bottom panel shows the radial magnetic field using the real data.

Sim	$E_{\text{mag}}^{\text{tot}}$	$E_{\text{mag}}^{m=0}$	$E_{\text{mag}}^{m=1}$	$E_{\text{mag}}^{m=2}$	$E_{\text{mag}}^{l,m>10}$
A4	5.0(-1)	5.2(-2)	4.7(-4)	3.3(-4)	1.2(-3)
A14	1.41	2.7(-1)	5.4(-4)	1.1(-3)	2.7(-3)
A16	5.1(-1)	2.2(-2)	2.7(-4)	2.6(-4)	2.5(-3)
B1	2.3(-1)	3.0(-2)	1.9(-4)	1.1(-4)	5.9(-4)
B4	2.19	1.4(-1)	1.6(-3)	1.0(-3)	8.8(-3)
B5	4.6(-1)	2.3(-2)	2.6(-4)	2.1(-4)	2.2(-3)
C3	3.1(-1)	5.0(-2)	1.7(-4)	2.9(-4)	5.5(-4)
C5	2.65	1.2(-1)	3.0(-3)	2.2(-3)	8.5(-3)
C6	9.2(-1)	2.5(-2)	4.6(-4)	1.1(-3)	4.9(-3)

**Table 4.2.4:** From left to right the columns indicate the total magnetic energy density  $E_{\text{mag}}^{\text{tot}}$ , the magnetic energy density of the modes  $m = 0, 1, 2$ , and the magnetic energy density considering  $l, m > 10$ .

## Chapter 5

# Possible impact of large scale magnetic field on binary systems

This chapter presents an exploration of the feasibility of the Applegate mechanism as a possible origin of the eclipsing time variations in Post-Common Envelope Binaries (PCEBs).

### 5.1 Eclipsing Time Variations

As described on the introduction, PCEBs often consist of a magnetically active M dwarf and a White Dwarf. This type of binary system often presents eclipsing times variations (ETVs) in the Observed minus Calculated diagram (O - C). An O - C diagram compares the actual timing of an eclipse with the moment we expect the event to occur in case of a constant period.

PCEBs are the result of the common envelope phase of a binary system (Paczynski et al., 1976). The common envelope phase starts with two main-sequence stars, stars 1 and 2 in Figure 5.1.1. One of them expands into its red-giant phase filling its Roche lobe and encompasses the binary companion. The expansion results in a common envelope around the two stars, and star 2 starts spiralling into star 1. Eventually, the envelope disappears, leaving a close system consisting of the core of star 1 in the orbit of star 2.

90% of the PCEBs present eclipsing time variations (Zorotovic and Schreiber, 2013). The variation of the binary period may be related to the presence

of a third body, e.g., a planet, causing changes in the light travel time, e.g., [Beuermann et al. \(2013\)](#). There are two scenarios in which those planets might have formed. The first-generation scenario explains how the planet formed with the binary system and survived the Common envelope phase, although this is unlikely since protoplanetary disk lifetimes around main-sequence binaries are often too brief to generate big planets in most cases ([Kraus et al., 2011](#)). Furthermore, the planets must have survived the common-envelope evolution. The second-generation scenario is that the planet forms from the Common envelope material that is expelled from the system ([Schleicher and Dreizler, 2014](#)). Alternatively, the ETVs may be produced by the changes of the gravitational quadrupole moment of the magnetically active star, which in turn is produced by an underlying magnetic field within it. This was first proposed by [Applegate \(1992\)](#), and it is analyzed here.

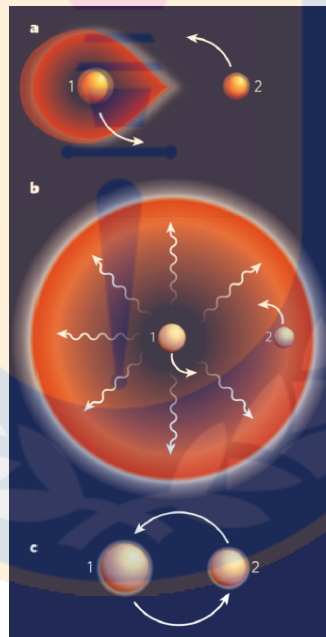


**Figure 5.1.1:** Common envelope phase illustration. This Figure was taken from [Bulik \(2007\)](#).

## 5.2 The Applegate mechanism

The Applegate mechanism proposed by [Applegate \(1992\)](#) attributes the eclipsing time variations to the magnetic activity of the active star, by coupling the magnetic activity to the variations of the gravitational quadrupole moment

of the star. In this model, the binary system is composed of the magnetically active star and a companion star, which is treated as a point mass. The gravitational potential outside the active star is given by

$$\phi(x) = -\frac{GM}{r} - \frac{3}{2}GQ_{ik}\frac{x_ix_k}{r^5}, \quad (5.2.1)$$

where  $x_i$  and  $x_j$  are Cartesian coordinates measured from the center of mass of the star,  $Q_{ik}$  is the quadrupole tensor defined by

$$Q_{ik} = I_{ik} - \frac{1}{3}\delta_{ik}\text{Tr}I, \quad (5.2.2)$$

where  $\text{Tr}I$  is the trace of the inertia tensor, which is defined by

$$I_{ik} = \int x_ix_k dm = \int \rho(x)x_ix_k d^3x. \quad (5.2.3)$$

Assuming that the system has synchronized spin and orbit, the orbit is circularized, and the rotational and orbital angular momenta are aligned. Taking the  $\hat{z}$ -axis to lie in the direction of the angular momentum, the  $\hat{x}$ -axis pointing at the companion, and the coordinate system rotating about the  $\hat{z}$ -axis, the total quadrupole moment in this coordinate system is only affected by the  $Q_{xx}$  term. Then, Equation 5.2.1 gives

$$\phi(x) = -\frac{GM}{r} - \frac{3}{2}\frac{GQ_{xx}}{r^3}. \quad (5.2.4)$$

Further, according to Applegate (1992) the variations of the quadrupole moment and the variations of the period of the binary system are related via

$$\frac{\Delta P}{P} = -9\left(\frac{R}{a}\right)^2 \frac{\Delta Q_{xx}}{MR^2}, \quad (5.2.5)$$

where  $R$  is the radius of the active star and  $a$  is the separation between the stars.

The angular momentum in the star's outer layers determines the quadrupole moment to a substantial degree. The outer layers of the star will spin up and become more oblate if angular momentum is transferred to them. According to Applegate (1992), a torque provided by a subsurface magnetic field is needed for angular momentum transfer to take place. The required strength of the

magnetic field is given as

$$B^2 \sim \frac{GM^2}{R^4} \left(\frac{a}{R}\right)^2 \frac{\Delta P}{P_{\text{mod}}}, \quad (5.2.6)$$

where  $P_{\text{mod}}$  is the orbital period modulation timescale. The amplitude of orbital period modulation  $\Delta P/P$ , and the amplitude of the oscillation in the O - C diagram is given by

$$\frac{\Delta P}{P} = 2\pi \frac{O - C}{P_{\text{mod}}}. \quad (5.2.7)$$

### 5.2.1 Quadrupole moment

In order to obtain  $Q_{xx}$  in the simulations presented here, it is necessary to take into account the enhanced luminosity described in 3.3.1. Then, the ratio of luminosities  $L_{\text{ratio}}$  is given by

$$L_{\text{ratio}} = \frac{\mathcal{L}}{\mathcal{L}_{M5}}, \quad (5.2.8)$$

where  $\mathcal{L}_{M5}$  is the dimensionless luminosity for an M5 star (see below) and  $\mathcal{L}$  is the dimensionless luminosity in the simulations (Dobler et al., 2006; Käpylä, 2021) which is

$$\mathcal{L} = \frac{L_{\text{sim}}}{\sqrt{G^3 M^5 / R^5}} = 5.5 \cdot 10^{-5}. \quad (5.2.9)$$

The dimensionless luminosity for an M5 star is calculated as follows

$$\mathcal{L}_{M5} = \frac{L_{M5}}{\sqrt{G^3 M_{M5}^5 / R_{M5}^5}}, \quad (5.2.10)$$

where  $G$  is the gravitational constant,  $L_{M5}$ ,  $M_{M5}$  and  $R_{M5}$  are the luminosity, mass and radius for the star. The parameters were obtained with the MESA code (see 3.3.1). Then,  $\mathcal{L}_{\text{ratio}} = 2.1 \cdot 10^9$ . One could also use the flux ratio  $\mathcal{F}_{\text{ratio}}$  and obtain the same number as using  $\mathcal{L}_{\text{ratio}}$ , since the radius does not change. The fluctuation of the pressure is given as

$$\Delta p = \left(\frac{\partial p}{\partial \rho}\right)_s \Delta \rho \equiv c_s^2 \Delta \rho, \quad (5.2.11)$$

where  $c_s$  is the sound speed and the subscript  $s$  indicates constant entropy variations. On the other hand, the pressure scales as

$$\Delta P \sim \rho u^2. \quad (5.2.12)$$

Equating 5.2.11 and 5.2.12 we get

$$\frac{\Delta \rho}{\rho} \sim \frac{u^2}{c_s^2} = \text{Ma}^2, \quad (5.2.13)$$

where  $\text{Ma}$  is the Mach number, which scales as (see Käpylä et al. 2020; Navarrete et al. 2020)

$$\text{Ma} \sim L_{\text{ratio}}^{1/3}, \quad (5.2.14)$$

and thereby,

$$\Delta \rho \sim L_{\text{ratio}}^{2/3}. \quad (5.2.15)$$

Then, the scaling for  $Q_{xx}$  needs a factor of  $L_{\text{ratio}}^{-2/3} = (2.1 \cdot 10^9)^{-2/3}$ , which in  $\text{kg m}^2$  is

$$Q_{xx} = 2.2 \cdot 10^{40} Q_{xx}^{\text{sim}}, \quad (5.2.16)$$

where the subscript "sim" denotes the quadrupole moment obtained from simulations.

### 5.2.1.1 Evolution of $Q_{xx}$

The evolution of  $Q_{xx}$  together with  $E_{\text{mag}}$  is presented for some of the simulations. Figure 5.2.4 shows the time evolution of  $Q_{xx}$  for simulations A4, A14 and A16, with magnetic Prandtl numbers of 0.5, 5 and 10, respectively. In simulation A4,  $Q_{xx}$  evolves in a quasi-periodic manner, it presents three minima, the first at  $t = 125$  years, the second at  $t = 175$  years and the third at  $t = 230$  years.  $Q_{xx}$  in A14 also shows peaks and troughs, but it has more fluctuations. In A16, the quadrupole moment has one important minimum at  $t = 110$  years, then it increases until  $t = 170$  years and increases again presenting various maxima and minima. In the three sets, at  $\text{Pr}_M < 5$   $Q_{xx}$  evolves correlated with  $E_{\text{mag}}$ , while at higher  $\text{Pr}_M$  (5 and 10),  $Q_{xx}$  appears less correlated with  $E_{\text{mag}}$ , and it seems anti-correlated at  $\text{Pr}_M = 10$ . Figures 5.2.5 and 5.2.6 show the evolution of both for simulations of set B (B1, B4 and B5) and set C (C3, C5 and C6), respectively. In this regime, they evolve in a similar

manner as in set A. From the figures it is possible to see (by eye) a correlation at low- $\text{Pr}_M$  and an anti-correlation at high- $\text{Pr}_M$ .

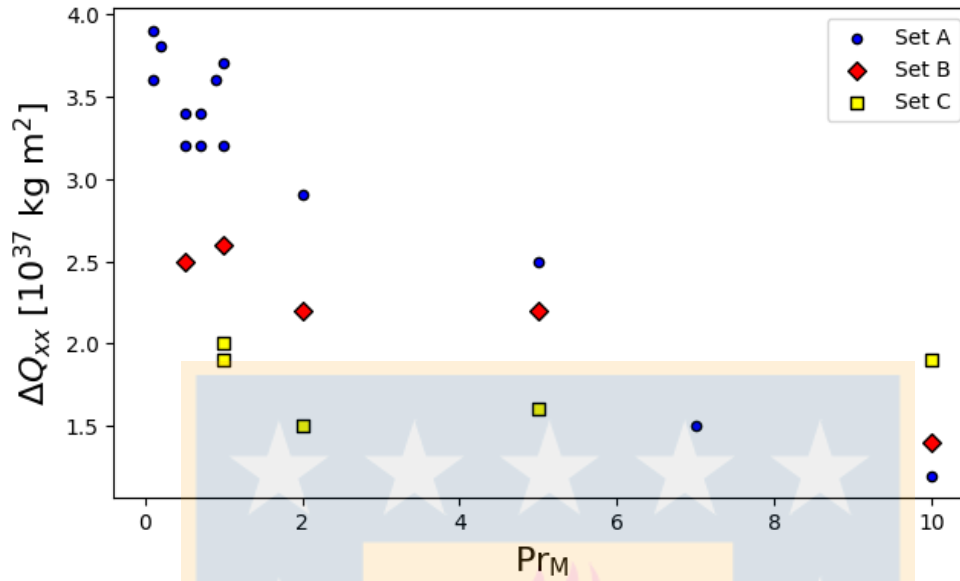
To determine if there is a correlation or anti-correlation, the Pearson (linear) correlation was utilized, with the coefficient ranging from  $[-1,1]$ , with 1 (-1) representing perfect correlation (anti-correlation). The correlation coefficient is calculated as follows:

$$x|y = \frac{\sum(x - m_x)(y - m_y)}{\sqrt{(\sum(x - m_x)^2 \sum(y - m_y)^2)'}} \quad (5.2.17)$$

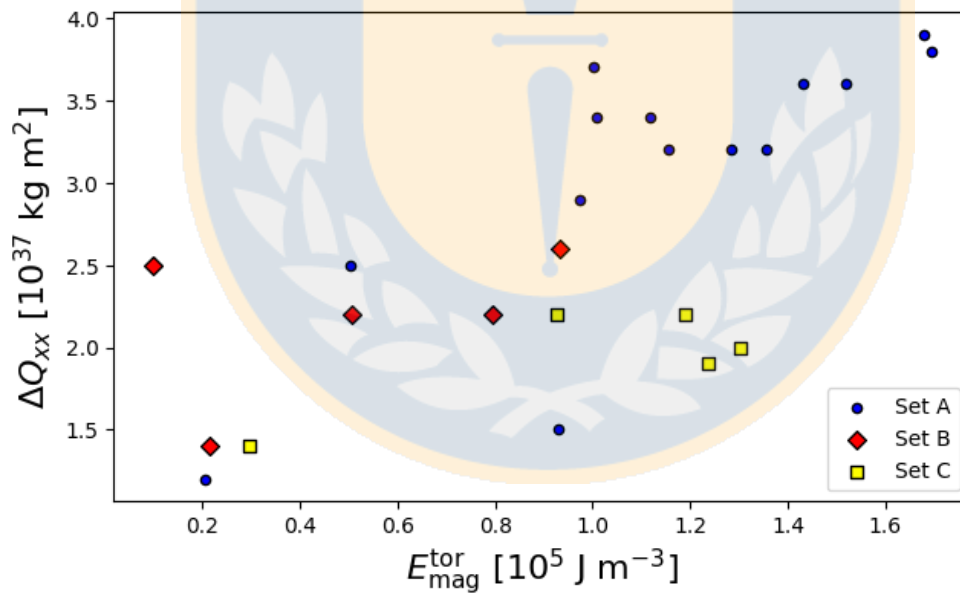
where  $m_x$  and  $m_y$  are the sample mean and  $x|y$  is the coefficient.

Table 5.2.1 provides the amplitude of  $Q_{xx}$  for the simulations presented here, and the correlation coefficients between the quadrupole moment and the total magnetic energy. From the table it is clear that a correlation (anti-correlation) exists for simulations with  $\text{Pr}_M \leq 2$  ( $\text{Pr}_M \geq 5$ ). Besides that, the amplitude of the variation of  $Q_{xx}$  (see Table 5.2.1) decreases with increasing  $\text{Pr}_M$ , and it decreases further with decreasing rotation rate, e.g. simulations A10, B2 and C1 have  $\text{Pr}_M = 1$  with  $\Delta Q_{xx} = 3.7 \cdot 10^{37}$ ,  $2.6 \cdot 10^{37}$  and  $2.0 \cdot 10^{37}$  [kg m<sup>2</sup>], respectively. Figure 5.2.1 provides a scatter plot for better visualization.

Figures 5.2.2 and 5.2.3 show how  $\Delta Q_{xx}$  is related to the toroidal and poloidal magnetic energy densities, respectively. The bottom panel of that figure shows that  $\Delta Q_{xx}$  has larger values when the poloidal magnetic energy density is larger. When comparing with the toroidal magnetic energy, there is a trend but it is less clear.



**Figure 5.2.1:** Scatter plot of  $\Delta Q_{xx}$  as a function of the magnetic Prandtl number.



**Figure 5.2.2:** Scatter plot of  $\Delta Q_{xx}$  as a function of the toroidal magnetic energy density.

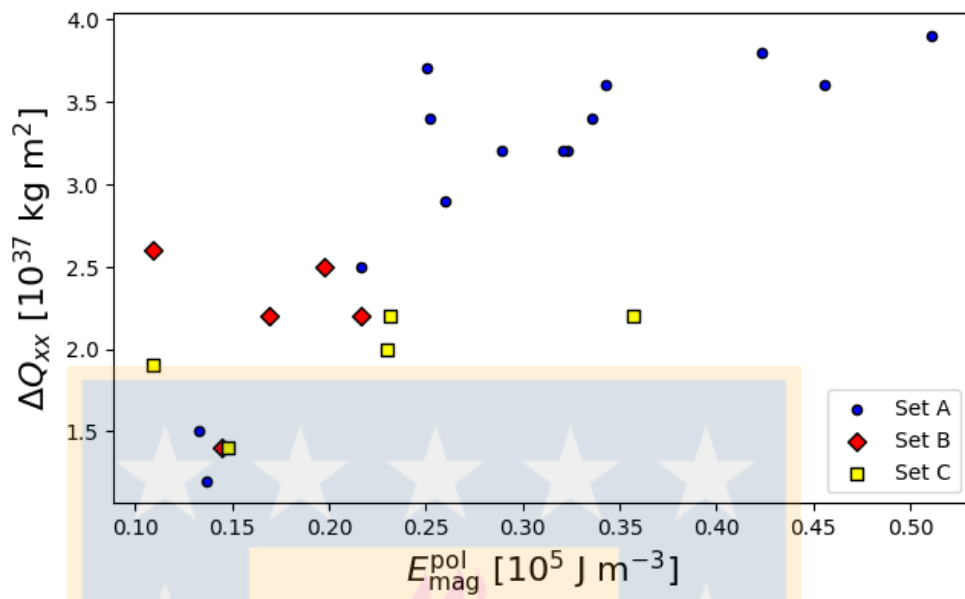


**Figure 5.2.3:** Scatter plot of  $\Delta Q_{xx}$  as a function of the poloidal magnetic energy density.

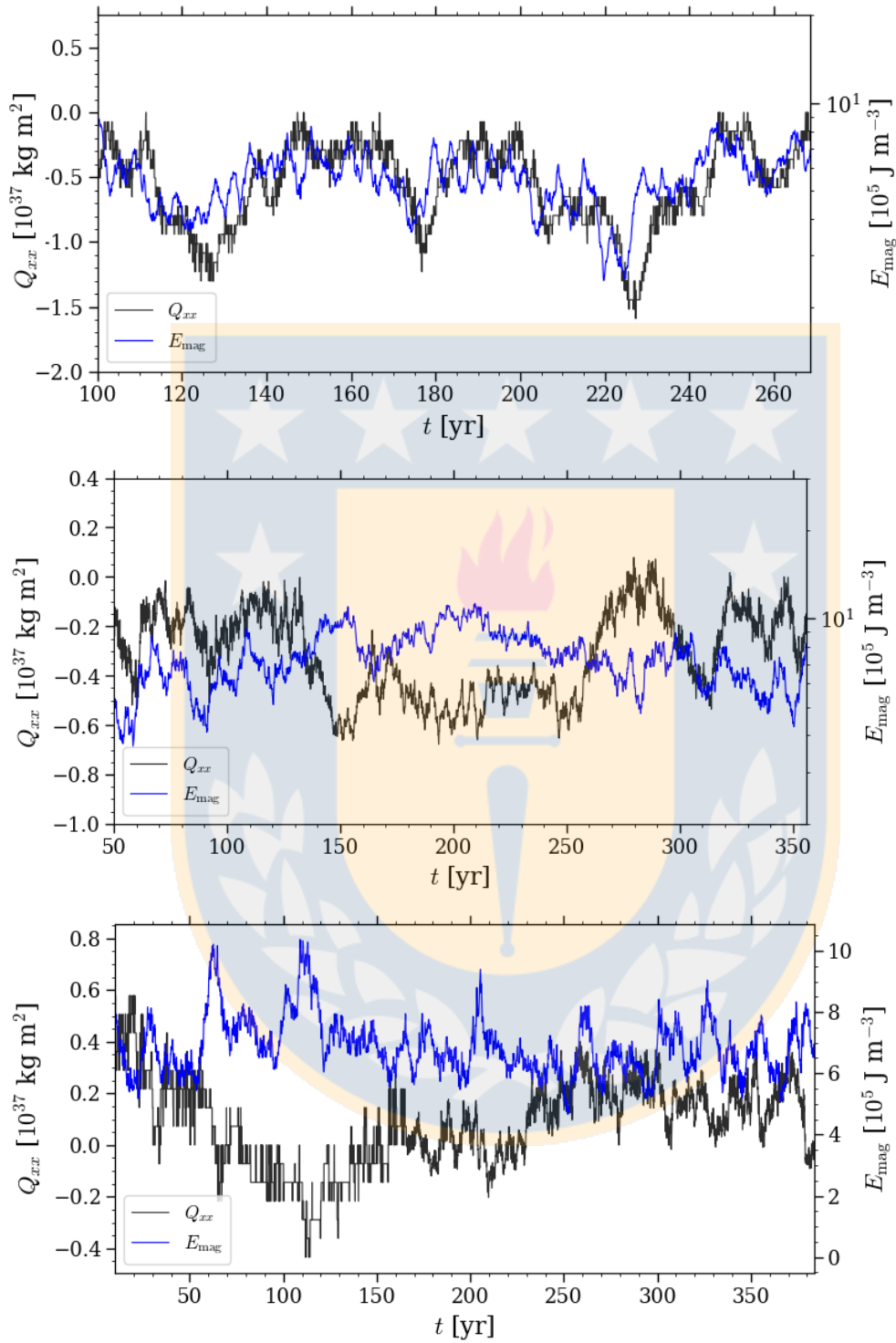


**Figure 5.2.4:** Time evolution of  $Q_{xx}$  together with  $E_{\text{mag}}$  for simulations A4, A14 and A16.

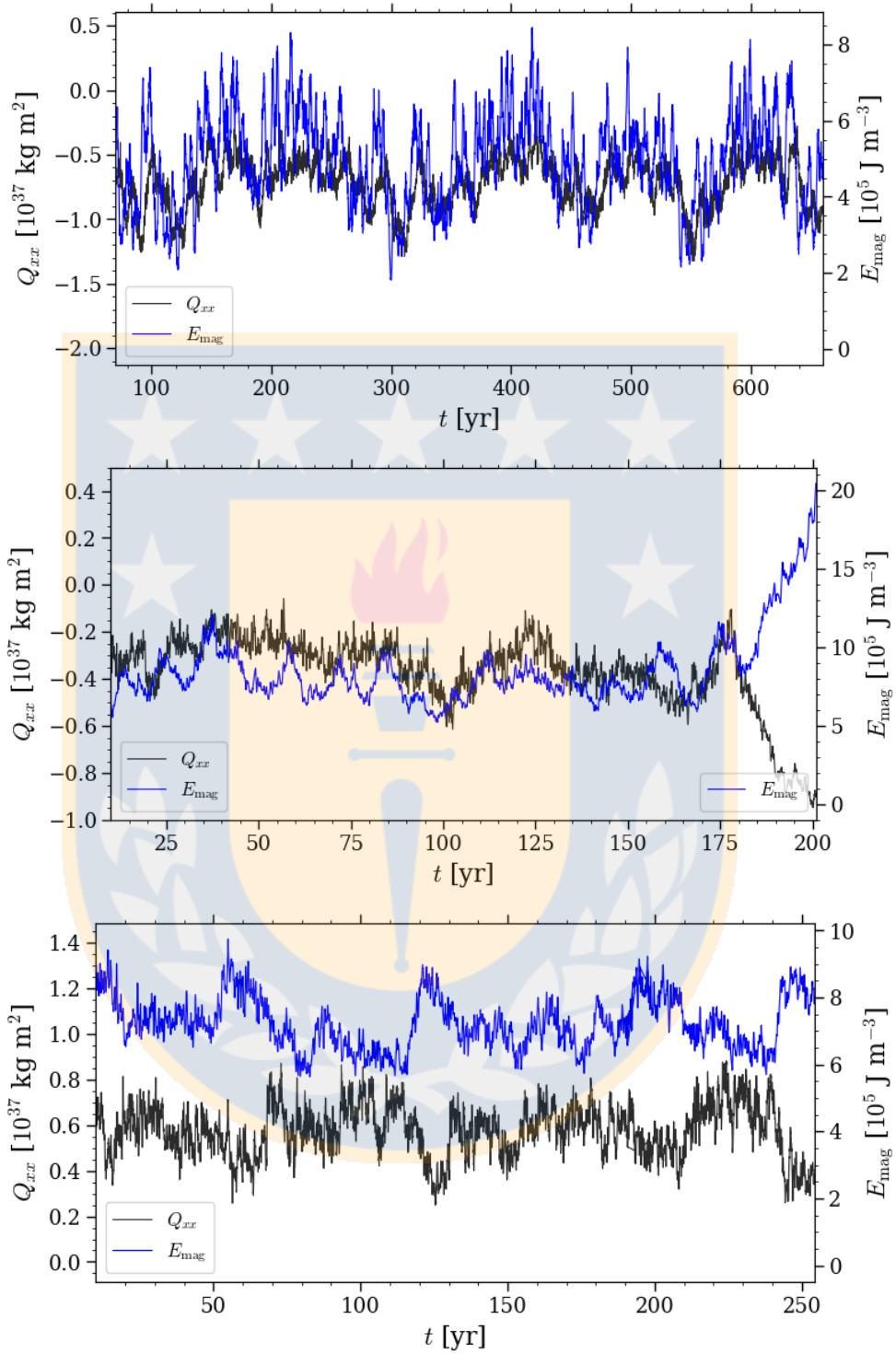


**Figure 5.2.5:** Time evolution of  $Q_{xx}$  together with  $E_{\text{mag}}$  for simulations B1, B4 and B5.

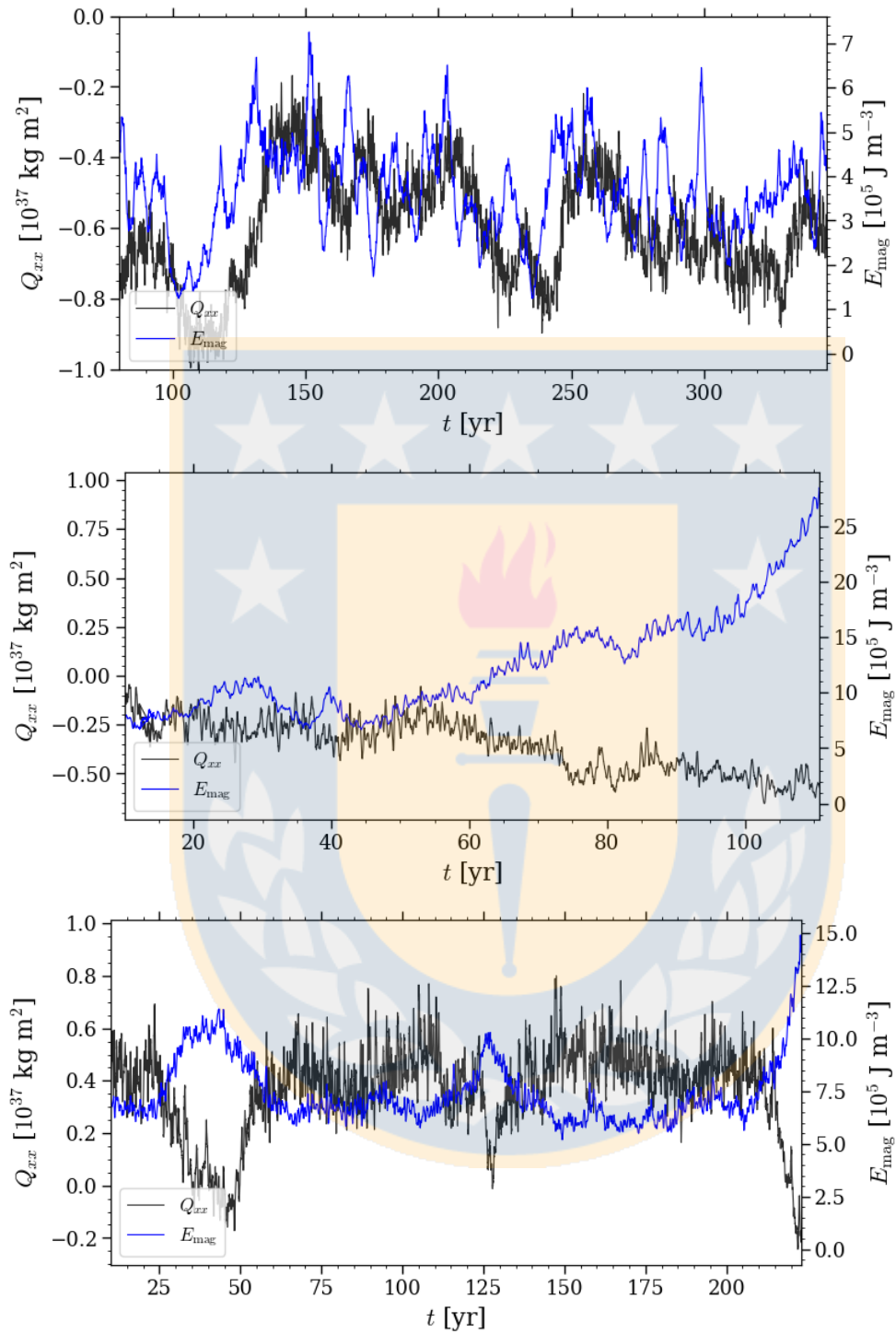


**Figure 5.2.6:** Time evolution of  $Q_{xx}$  together with  $E_{\text{mag}}$  for simulations C3, C5 and C6.

Sim	$\Delta Q_{xx}$	$Q_{xx} E_{\text{mag}}^{\text{total}}$
A1	3.9(37)	0.89
A2	3.6(37)	0.45
A3	3.8(37)	-0.01
A4	3.4(37)	0.49
A5	3.4(37)	0.48
A6	3.2(37)	0.43
A7	3.6(37)	0.32
A9	3.2(37)	0.43
A10	3.7(37)	0.33
A11	3.2(37)	0.33
A13	2.9(37)	0.44
A14	2.5(37)	-0.57
A15	1.5(37)	-0.02
A16	1.2(37)	-0.46
B1	2.5(37)	0.45
B2	2.6(37)	0.11
B3	2.2(37)	0.56
B4	2.2(37)	-0.57
B5	1.4(37)	-0.47
C1	2.0(37)	0.27
C3	1.9(37)	0.33
C4	1.5(37)	0.44
C5	1.6(37)	-0.79
C6	1.9(37)	-0.80

**Table 5.2.1:** The second column gives the amplitude of the variations of  $Q_{xx}$  and the third column provides the correlation coefficient between  $Q_{xx}$  and  $E_{\text{mag}}$ .

### 5.2.2 Period variations and O - C

The period variations and the expected O - C variations are calculated considering the stellar parameters for an M5 star. For this purpose, we will consider various values for the binary separation  $a$  of the PCEBs. According to Table 2 of the work by [Völschow et al. \(2016\)](#), the binary separation for those systems with low-mass secondary star ranges from 0.6 to 1.7  $R_{\odot}$ . We will use four binary separations,  $a_1 = 0.6$ ,  $a_2 = 0.8$ ,  $a_3 = 1.4$  and  $a_4 = 1.7$ , in units of the solar radius,  $R_{\odot}$ . The modulation period  $P_{\text{mod}}$  corresponds to the period of  $Q_{xx}$ , which was calculated via Fast Fourier Transform. The calculations are for a subset of the simulations using Equations 5.2.5 and 5.2.7. Table 5.2.2

gives variations of the orbital period during one cycle of the binary,  $\left(\frac{\Delta P}{P}\right)_{a_i}$  for the binary separations  $a_i$ , with  $i = 1, 2, 3, 4$  already defined before. Table 5.2.3 gives the modulation period  $P_{\text{mod}}$  and the O - C values for the different binary separations, also denoted with the subscript  $a_i$ . The obtained values of  $\Delta P/P$  range from  $1.84 \cdot 10^{-10}$  to  $4.82 \cdot 10^{-9}$ , while the O - C values range from 1.44 to 0.04 seconds.

Sim	$\left(\frac{\Delta P}{P}\right)_{a_1}$	$\left(\frac{\Delta P}{P}\right)_{a_2}$	$\left(\frac{\Delta P}{P}\right)_{a_3}$	$\left(\frac{\Delta P}{P}\right)_{a_4}$
A1	4.82(-9)	2.71(-9)	8.85(-10)	6.00(-10)
A3	4.45(-9)	2.50(-9)	8.17(-10)	5.54(-10)
A4	4.20(-9)	2.36(-9)	7.72(-10)	5.23(-10)
A14	3.09(-9)	1.7(-9)	5.67(-10)	3.85(-10)
A16	1.48(-9)	8.34(-10)	2.72(-10)	1.84(-10)
B1	3.09(-9)	1.73(-10)	5.67(-10)	3.85(-10)
B5	1.73(-9)	9.73(-10)	3.17(-10)	2.15(-10)
C3	2.34(-9)	1.32(-9)	4.31(-10)	2.92(-10)
C6	2.34(-9)	1.32(-9)	4.31(-10)	2.92(-10)

**Table 5.2.2:** Variation of the orbital period during a cycle of the binary for the different binary periods  $a_1 = 0.6$ ,  $a_2 = 0.8$ ,  $a_3 = 1.4$  and  $a_4 = 1.7 R_{\odot}$ .

Sim	$P_{\text{mod}}$	O - C <sub><math>a_1</math></sub>	O - C <sub><math>a_2</math></sub>	O - C <sub><math>a_3</math></sub>	O - C <sub><math>a_4</math></sub>
A1	50	1.21	0.68	0.22	0.15
A3	29	0.64	0.36	0.11	0.08
A4	67	1.41	0.79	0.25	0.17
A14	56	0.86	0.49	0.15	0.10
A16	49	0.36	0.20	0.06	0.04
B1	93	1.44	0.811	0.26	0.17
B5	63	0.54	0.30	0.10	0.06
C3	63	0.74	0.41	0.13	0.09
C6	80	0.94	0.53	0.17	0.11

**Table 5.2.3:** From left to right the columns indicate the modulation period  $P_{\text{mod}}$  (in years), and the O - C values (in seconds) for  $a_1 = 0.6$ ,  $a_2 = 0.8$ ,  $a_3 = 1.4$  and  $a_4 = 1.7 R_{\odot}$ .

### 5.2.3 Comparison to a real system: HU Aquarii

HU Aquarii is a PCEB system with a white dwarf and an M4 star that has a mass of  $0.18 M_{\odot}$ , a radius of  $0.22 R_{\odot}$  and rotation period of a few hours. This

star has a similar mass and radius to the M5 star used in this thesis, so it is a good comparison example.

HU Aquarii has been a candidate for hosting planets due to the time variations. However, [Wittenmyer et al. \(2012\)](#) suggested that the planetary hypothesis is not the right mechanism to explain the eclipsing time variations. [Navarrete et al. \(2018\)](#) found the Applegate mechanism to be feasible in this system.

The observed  $\frac{\Delta P}{P}$  of this system is  $1.8 \cdot 10^{-6}$  ([Völschow et al., 2016](#)), whilst in the simulations presented here the relative period change is three to four orders of magnitude lower. [Bours et al. \(2016\)](#) reported O - C values for 67 close binaries, with most of the secondaries being M dwarfs, including HU Aquarii. Assuming that the O - C diagrams of Figure 1 of that work are for a cycle, the amplitude of the O - C for HU Aquarii is 155 seconds. The difference between the results provided here and those reported may be due to the difference in the rotation rates used here, which are lower than the rotation rates of actual M dwarfs in PCEBs. Furthermore, the model of [Lanza \(2020\)](#), in which the star is not tidally locked and where the different components of the quadrupole tensor contribute, could provide an alternative explanation without requiring large fluctuations of  $Q_{xx}$ .

## Chapter 6

### Summary and discussion

In this thesis three-dimensional MHD simulations of fully convective M dwarf stars were performed using the "star-in-a-box" model by Käpylä (2021).

We obtained different dynamo solutions in the parameter regime explored here, namely the magnetic Prandtl number with values between 0.1 to 10 and the rotation period between 43 to 90 days. This is the largest parameter space studied so far in simulations modeling the entire star.

The set of simulations with the rotation period of 43 days presents mainly two solutions of the toroidal magnetic field. At  $\text{Pr}_M \leq 2$ , the magnetic field presents quasi-periodic cycles, where cycles become longer with increasing the magnetic Prandtl number. At  $\text{Pr}_M \geq 5$  the cycle no longer exist and the toroidal magnetic field shows irregular reversals.

In simulations with lower rotation the toroidal magnetic fields do not show cyclic reversals. At  $P_{\text{rot}}=61$  days the reversals are mainly irregular with no clear pattern. In the case with  $P_{\text{rot}} = 90$  days, the toroidal magnetic field is mainly dipolar for  $\text{Pr}_M \leq 5$ . In the higher  $\text{Pr}_M$  case, the structures of the toroidal magnetic field are less ordered and smaller than in the lower- $\text{Pr}_M$  cases. Besides, the toroidal magnetic field shows a quasi-stationary solution from mid-latitudes to the poles.

We found that the large-scale structures of the toroidal magnetic field also change with depth. At  $\text{Pr}_M \leq 2$  the change is more subtle, keeping the main features, while at  $\text{Pr}_M \geq 5$ , the large-scale structures disappear from the

surface to 70% of the stellar radius. In a similar way, the radial magnetic field near the surface shows smaller and more intense structures with larger magnetic Prandtl numbers than in the lower ones. Additionally, the field is more concentrated near the equator with increasing  $\text{Pr}_M$ .

The large-scale flows were also studied. For all the simulations presented here, the rotation rate is solar-like, which was analysed radially and latitudinally. The amplitude of the radial differential rotation decreases with increasing  $\text{Pr}_M$ . The decrease or slight quenching of differential rotation at high magnetic Reynolds numbers (magnetic Prandtl numbers) was shown earlier via simulations, e.g., [Käpylä et al. \(2017\)](#) and [Schrunner et al. \(2012\)](#). The latter showed that the quenching was associated with a transition from an oscillatory multipolar large-scale field configurations to quasi-stationary dipole-dominated dynamos as a function of the magnetic Reynolds number. A mainly dipolar large-scale field is present in simulations of set C, which have a reduced amount of radial differential rotation. Furthermore, the strong decrease of the differential rotation frequently coincides with the appearance of a small-scale dynamo ([Käpylä et al., 2017](#)).

The kinetic helicity is negative (positive) in the northern (southern) hemisphere, together with a positive gradient of  $\bar{\Omega}$ , is associated with a poleward propagating dynamo wave ([Parker, 1955](#); [Yoshimura, 1975](#)).

In terms of the energy density, there is no systematic change in the total magnetic energy density in the parameter regime explored here. Nevertheless, the toroidal magnetic energy decreases with increasing magnetic Prandtl number, and the kinetic energy density also decrease with decreasing  $\text{Pr}_M$ . A spherical harmonic decomposition ([Viviani et al., 2018](#); [Navarrete et al., 2021](#)) was performed to measure the magnetic energy density present in each mode. The  $m = 0$  mode is dominant in all the simulations presented here, this means that the axisymmetric component dominates. The energy contained in the higher modes, which correspond to the energy of the smaller structures, are one or two orders of magnitude lower than the energy of the  $m = 0$  mode.

We have studied the nature of  $Q_{xx}$  with 3-dimensional magneto-hydrodynamical simulations to probe the feasibility of the Applegate mechanism ([Applegate, 1992](#)) to explain the ETVs in PCEBs. This mechanisms

assumes that the axisymmetric part of the magnetic field is the one that contributes to the variations of the quadrupole moment. In the simulations presented here, the axisymmetric part or the  $m = 0$  mode of the magnetic field contributes the most according to the spherical harmonic decomposition performed.

Since the quadrupole moment depends on the density, it also changes with the magnetic Prandtl number, showing a decrease with increasing  $\text{Pr}_M$ , and a further decrease at lower rotation rates. The strong dependence of  $\Delta Q_{xx}$  on stellar rotation has been demonstrated by [Navarrete \(2019\)](#).

Furthermore, using the Pearson correlation coefficient, correlation between  $Q_{xx}$  and the total magnetic energy was found for magnetic Prandtl numbers smaller than 5, while for higher values of  $\text{Pr}_M$  an anticorrelation was found.

$\Delta P/P$  and the O - C values were calculated on basis of the Applegate model ([Applegate, 1992](#)) from our simulations considering four different binary separations. Since  $\Delta P/P$  depends inverse square of the binary separation, its values are larger for smaller binary separation, and vice versa.

When comparing with real PCEBs, the difference in the amplitude of the orbital period modulation from simulations and observations is mainly explained because the rotation rate in our simulations is significantly lower than in real systems. [Völschow et al. \(2016\)](#) reported amplitudes of the period variations for PCEBs with secondary fully convective stars that present values of the order of  $10^{-6}$  and  $10^{-7}$ . If the variations of the quadrupole moment from simulations of fully convective stars reach  $10^{40}$  [kg m<sup>2</sup>], the O - C diagram could be explained with this mechanism. To reach variations of  $Q_{xx}$  of that order, a logical next step will be to perform simulations with higher rotation rates.

More complex models have been proposed by some authors to explain the eclipsing time variations in PCEBs through the variation of the quadrupole moment. The most recent one is the model by [Lanza \(2020\)](#). In that model the star is not tidally locked like in the Applegate mechanism ([Applegate, 1992](#)) and the different components of the quadrupole tensor contribute, not only  $Q_{xx}$ . This model has been already applied to simulations of solar-like stars by [Navarrete et al. \(2021\)](#).

---

The star-in-a-box setup (Käpylä, 2021) used here can also be used in the future to study magnetic fields in partially convective stars and giant stars.



## Bibliography

- Andersen, J. M. and Korhonen, H. (2015). Stellar activity as noise in exoplanet detection – II. Application to M dwarfs. *Monthly Notices of the Royal Astronomical Society*, 448(4):3053–3069.
- Applegate, J. H. (1992). A Mechanism for Orbital Period Modulation in Close Binaries. , 385:621.
- Astudillo-Defru, Delfosse, X., Bonfils, X., Forveille, T., Lovis, C., and Rameau, J. (2017). Magnetic activity in the harps m dwarf sample - the rotation-activity relationship for very low-mass stars through r'hk. *A&A*, 600:A13.
- Babcock, H. (1961). The topology of the sun's magnetic field and the 22-year cycle. *The Astrophysical Journal*, 133:572.
- Baliunas, S. L., Donahue, R. A., Soon, W. H., Horne, J. H., Frazer, J., Woodard-Eklund, L., Bradford, M., Rao, L. M., Wilson, O. C., Zhang, Q., Bennett, W., Briggs, J., Carroll, S. M., Duncan, D. K., Figueroa, D., Lanning, H. H., Misch, T., Mueller, J., Noyes, R. W., Poppe, D., Porter, A. C., Robinson, C. R., Russell, J., Shelton, J. C., Soyumer, T., Vaughan, A. H., and Whitney, J. H. (1995). Chromospheric Variations in Main-Sequence Stars. II. , 438:269.
- Beuermann, K., Dreizler, S., Hessman, F. V., Backhaus, U., Boesch, A., Husser, T.-O., Nortmann, L., Schmelev, A., and Springer, R. (2013). The eclipsing post-common envelope binary css21055: a white dwarf with a probable brown-dwarf companion. *Astronomy & Astrophysics*, 558:A96.
- Biermann, L. (1943). Über die chemische Zusammensetzung der sonne. *Zeitschrift für Astrophysik*, 22:244.
- Boro Saikia, S., Jeffers, S. V., Petit, P., Marsden, S., Morin, J., and Folsom, C. P. (2015). Variable magnetic field geometry of the young sun hn pegasi (hd 206860). *A&A*, 573:A17.
- Borrero, J., Jafarzadeh, S., Schüssler, M., and Solanki, S. (2017). Solar magnetoconvection and small-scale dynamo. *Space Science Reviews*, 210(1):275–316.
- Bours, M. C. P., Marsh, T. R., Parsons, S. G., Dhillon, V. S., Ashley, R. P., Bento, J. P., Breedt, E., Butterley, T., Caceres, C., Chote, P., Copperwheat, C. M., Hardy, L. K., Hermes, J. J., Irawati, P., Kerry, P., Kilkenney, D., Littlefair,

- S. P., McAllister, M. J., Rattanasoon, S., Sahman, D. I., Vučković, M., and Wilson, R. W. (2016). Long-term eclipse timing of white dwarf binaries: an observational hint of a magnetic mechanism at work. , 460(4):3873–3887.
- Brandenburg, A. (2005). The case for a distributed solar dynamo shaped by near-surface shear. *The Astrophysical Journal*, 625(1):539.
- Brandenburg, A. and Subramanian, K. (2005). Astrophysical magnetic fields and nonlinear dynamo theory. *Physics Reports*, 417(1-4):1–209.
- Brown, B. P., Oishi, J. S., Vasil, G. M., Lecoanet, D., and Burns, K. J. (2020). Single-hemisphere dynamos in m-dwarf stars. *The Astrophysical Journal Letters*, 902(1):L3.
- Browning, M. K. (2008). Simulations of dynamo action in fully convective stars. *The Astrophysical Journal*, 676(2):1262–1280.
- Bulik, T. (2007). Black holes go extragalactic. *Nature*, 449(7164):799–801.
- Chabrier, G. and Baraffe, I. (1997). Structure and evolution of low-mass stars. *Astronomy Astrophysics*, 327:1039–1053.
- Charbonneau, P. (2013). Stellar dynamos. In *Solar and Stellar Dynamos*, pages 187–214. Springer.
- Charbonneau, P. (2014). Solar dynamo theory. *Annual Review of Astronomy and Astrophysics*, 52(1):251–290.
- Charbonneau, P. (2020). Dynamo models of the solar cycle. *Living Reviews in Solar Physics*, 17(1):4.
- Charbonneau, P. (2020). Dynamo models of the solar cycle. vol. 17. *Living Rev Sol Phys*, page 4.
- Choudhuri, A. R. (2021). The meridional circulation of the sun: Observations, theory and connections with the solar dynamo. *SCIENCE CHINA Physics, Mechanics & Astronomy*, 64(3):1–27.
- Choudhuri, A. R., Schussler, M., and Dikpati, M. (1995). The solar dynamo with meridional circulation. , 303:L29.
- Cole, E., Käpylä, P. J., Mantere, M. J., and Brandenburg, A. (2013). An azimuthal dynamo wave in spherical shell convection. *The Astrophysical Journal Letters*, 780(2):L22.
- Cowling, T. G. (1933). The magnetic field of sunspots. , 94:39–48.
- Dobler, W., Stix, M., and Brandenburg, A. (2006). Magnetic field generation in fully convective rotating spheres. *The Astrophysical Journal*, 638(1):336.
- Federrath, C., Schober, J., Bovino, S., and Schleicher, D. R. (2014). The turbulent dynamo in highly compressible supersonic plasmas. *The Astrophysical Journal Letters*, 797(2):L19.

- Gastine, T., Morin, J., Duarte, L., Reiners, A., Christensen, U. R., and Wicht, J. (2013). What controls the magnetic geometry of m dwarfs? *A&A*, 549:L5.
- Hale, G. E. (1908). On the Probable Existence of a Magnetic Field in Sun-Spots. *The Astrophysical Journal*, 28:315.
- Hale, G. E., Ellerman, F., Nicholson, S. B., and Joy, A. H. (1919). The magnetic polarity of sun-spots. *The Astrophysical Journal*, 49:153.
- Johns-Krull, C. M. (2007). The magnetic fields of classical t tauri stars. *The Astrophysical Journal*, 664(2):975–985.
- Johns-Krull, C. M. and Valenti, J. A. (1996). Detection of strong magnetic fields on m dwarfs. *The Astrophysical Journal Letters*, 459(2):L95.
- Johns-Krull, C. M., Valenti, J. A., and Koresko, C. (1999). Measuring the magnetic field on the classical t tauri star bp tauri. *The Astrophysical Journal*, 516(2):900.
- Käpylä, Käpylä, M. J., Olsper, N., Warnecke, J., and Brandenburg, A. (2017). Convection-driven spherical shell dynamos at varying prandtl numbers. *A&A*, 599:A4.
- Käpylä, P., Korpi, M., and Tuominen, I. (2006). Solar dynamo models with  $\alpha$ -effect and turbulent pumping from local 3d convection calculations. *Astronomische Nachrichten: Astronomical Notes*, 327(9):884–894.
- Käpylä, P. J. (2021). Star-in-a-box simulations of fully convective stars. *Astronomy & Astrophysics*, 651:A66.
- Käpylä, P. J., Gent, F. A., Olsper, N., Käpylä, M. J., and Brandenburg, A. (2020). Sensitivity to luminosity, centrifugal force, and boundary conditions in spherical shell convection. *Geophysical and Astrophysical Fluid Dynamics*, 114(1-2):8–34.
- Käpylä, P. J., Mantere, M. J., Cole, E., Warnecke, J., and Brandenburg, A. (2013). Effects of enhanced stratification on equatorward dynamo wave propagation. *The Astrophysical Journal*, 778(1):41.
- Klein, B., Donati, J.-F., Hébrard, É. M., Zaire, B., Folsom, C. P., Morin, J., Delfosse, X., and Bonfils, X. (2021). The large-scale magnetic field of proxima centauri near activity maximum. *Monthly Notices of the Royal Astronomical Society*, 500(2):1844–1850.
- Kochukhov, O. (2021). Magnetic fields of m dwarfs. *The Astronomy and Astrophysics Review*, 29(1):1–61.
- Kochukhov, O. and Lavail, A. (2017). The Global and Small-scale Magnetic Fields of Fully Convective, Rapidly Spinning M Dwarf Pair GJ65 A and B. , 835(1):L4.

- Kraft, R. P. (1967). Studies of Stellar Rotation. V. The Dependence of Rotation on Age among Solar-Type Stars. , 150:551.
- Kraus, A. L., Ireland, M. J., Hillenbrand, L. A., and Martinache, F. (2011). The role of multiplicity in disk evolution and planet formation. *The Astrophysical Journal*, 745(1):19.
- Krause, F. and Rädler, K. H. (1980). *Mean-field magnetohydrodynamics and dynamo theory*.
- Lanza, A. F. (2020). Internal magnetic fields, spin-orbit coupling, and orbital period modulation in close binary systems. *Monthly Notices of the Royal Astronomical Society*, 491(2):1820–1831.
- Leighton, R. B. (1969). A magneto-kinematic model of the solar cycle. *The Astrophysical Journal*, 156:1.
- Martínez Pillet, V. (2013). Solar Surface and Atmospheric Dynamics. The Photosphere. , 178(2-4):141–162.
- Navarrete (2019). Campos magnéticos en binarias cercanas= magnetic fields in close binaries.
- Navarrete, F., Schleicher, D., Fuentealba, J. Z., and Völschow, M. (2018). Applegate mechanism in post-common-envelope binaries: Investigating the role of rotation. *Astronomy & Astrophysics*, 615:A81.
- Navarrete, F. H., Käpylä, P. J., Schleicher, D. R., Ortiz, C. A., and Banerjee, R. (2021). Origin of eclipsing time variations: contributions of different modes of the dynamo-generated magnetic field. *arXiv preprint arXiv:2102.11110*.
- Navarrete, F. H., Schleicher, D. R., Käpylä, P. J., Schober, J., Völschow, M., and Mennickent, R. E. (2020). Magnetohydrodynamical origin of eclipsing time variations in post-common-envelope binaries for solar mass secondaries. *Monthly Notices of the Royal Astronomical Society*, 491(1):1043–1056.
- Noyes, R. W., Hartmann, L. W., Baliunas, S. L., Duncan, D. K., and Vaughan, A. H. (1984). Rotation, convection, and magnetic activity in lower main-sequence stars. , 279:763–777.
- Paczynski, B., Eggleton, P., Mitton, S., and Whelan, J. (1976). Structure and evolution of close binary systems. In *IAU Symp*, volume 73, page 75.
- Parker, E. N. (1955). Hydromagnetic Dynamo Models. , 122:293.
- Paxton, B., Bildsten, L., Dotter, A., Herwig, F., Lesaffre, P., and Timmes, F. (2010). Modules for experiments in stellar astrophysics (mesa). *The Astrophysical Journal Supplement Series*, 192(1):3.
- Pencil Code Collaboration, Brandenburg, A., Johansen, A., Bourdin, P., Dobler, W., Lyra, W., Rheinhardt, M., Bingert, S., Haugen, N., Mee, A., Gent, F., Babkovskaia, N., Yang, C.-C., Heinemann, T., Dintrans, B., Mitra, D.,

- Candelaresi, S., Warnecke, J., Käpylä, P., Schreiber, A., Chatterjee, P., Käpylä, M., Li, X.-Y., Krüger, J., Aarnes, J., Sarson, G., Oishi, J., Schober, J., Plasson, R., Sandin, C., Karchniwy, E., Rodrigues, L., Hubbard, A., Guerrero, G., Snodin, A., Losada, I., Pekkilä, J., and Qian, C. (2021). The Pencil Code, a modular MPI code for partial differential equations and particles: multipurpose and multiuser-maintained. *The Journal of Open Source Software*, 6(58):2807.
- Pizzolato, Maggio, A., Micela, G., Sciortino, S., and Ventura, P. (2003). The stellar activity-rotation relationship revisited: Dependence of saturated and non-saturated x-ray emission regimes on stellar mass for late-type dwarfs \*. *A&A*, 397(1):147–157.
- Prandtl, L. (1925). 7. bericht über untersuchungen zur ausgebildeten turbulenz. *ZAMM-Journal of Applied Mathematics and Mechanics/Zeitschrift für Angewandte Mathematik und Mechanik*, 5(2):136–139.
- Reeves, E., Van Helden, A., and Miller, D. M. (2012). On sunspots: Galileo galilei and christoph scheiner. *Aestimatio: Critical Reviews in the History of Science*, 9:97–102.
- Rincon, F. (2019). Dynamo theories. *Journal of Plasma Physics*, 85(4).
- Rossby, C.-G. (1939). Relation between variations in the intensity of the zonal circulation of the atmosphere and the displacements of the semi-permanent centers of action. *J. mar. Res.*, 2:38–55.
- Rüdiger, G. (1989). *Differential rotation and stellar convection: Sun and solar-type stars*, volume 5. Taylor & Francis.
- Sabin, L., Wade, G. A., and Lèbre, A. (2014). First detection of surface magnetic fields in post-AGB stars: the cases of U Monocerotis and R Scuti. *Monthly Notices of the Royal Astronomical Society*, 446(2):1988–1997.
- Schekochihin, A., Iskakov, A., Cowley, S., McWilliams, J., Proctor, M., and Yousef, T. (2007). Fluctuation dynamo and turbulent induction at low magnetic prandtl numbers. *New Journal of Physics*, 9(8):300.
- Schleicher, D. R. and Dreizler, S. (2014). Planet formation from the ejecta of common envelopes. *Astronomy & Astrophysics*, 563:A61.
- Schmidt, W. (1917). *Der Massenaustausch bei der ungeordneten Strömung in freier Luft und seine Folgen*. Hölder in Komm.
- Schou, J., Antia, H., Basu, S., Bogart, R., Bush, R., Chitre, S., Christensen-Dalsgaard, J., Di Mauro, M., Dziembowski, W., Eff-Darwich, A., et al. (1998). Helioseismic studies of differential rotation in the solar envelope by the solar oscillations investigation using the michelson doppler imager. *The Astrophysical Journal*, 505(1):390.
- Schrinner, M., Petitdemange, L., and Dormy, E. (2012). Dipole Collapse and Dynamo Waves in Global Direct Numerical Simulations. , 752(2):121.

- Solanki, S. K. (1993). Smallscale Solar Magnetic Fields - an Overview. , 63(1-2):1–188.
- Spiegel, E. and Zahn, J.-P. (1992). The solar tachocline. *Astronomy and Astrophysics*, 265:106–114.
- Steenbeck, M., Krause, F., and Rädler, K.-H. (1966). Berechnung der mittleren lorentz-feldstärke für ein elektrisch leitendes medium in turbulenter, durch coriolis-kräfte beeinflusster bewegung. *Zeitschrift für Naturforschung A*, 21(4):369–376.
- Suárez Mascareño, A., Rebolo, R., and González Hernández, J. I. (2016). Magnetic cycles and rotation periods of late-type stars from photometric time series. , 595:A12.
- Taylor, G. I. (1915). Eddy motion in the atmosphere. *Philosophical Transactions of the Royal Society of London. Series A, Containing Papers of a Mathematical or Physical Character*, 215:1–26.
- Viviani, Warnecke, J., Käpylä, M. J., Käpylä, P. J., Olsper, N., Cole-Kodikara, E. M., Lehtinen, J. J., and Brandenburg, A. (2018). Transition from axi- to nonaxisymmetric dynamo modes in spherical convection models of solar-like stars. *A&A*, 616:A160.
- Völschow, M., Schleicher, D., Banerjee, R., and Schmitt, J. (2018). Physics of the applegate mechanism: Eclipsing time variations from magnetic activity. *Astronomy & Astrophysics*, 620:A42.
- Völschow, M., Schleicher, D. R. G., Perdelwitz, V., and Banerjee, R. (2016). Eclipsing time variations in close binary systems: Planetary hypothesis vs. Applegate mechanism. , 587:A34.
- Wargelin, B. J., Saar, S. H., Pojmański, G., Drake, J. J., and Kashyap, V. L. (2017). Optical, UV, and X-ray evidence for a 7-yr stellar cycle in Proxima Centauri. , 464(3):3281–3296.
- Winters, J. G., Henry, T. J., Jao, W.-C., Subasavage, J. P., Chatelain, J. P., Slatten, K., Riedel, A. R., Silverstein, M. L., and Payne, M. J. (2019). The solar neighborhood. xlv. the stellar multiplicity rate of m dwarfs within 25 pc. *The Astronomical Journal*, 157(6):216.
- Wittenmyer, R. A., Horner, J., Marshall, J. P., Butters, O., and Tinney, C. (2012). Revisiting the proposed planetary system orbiting the eclipsing polar hu aquarii. *Monthly Notices of the Royal Astronomical Society*, 419(4):3258–3267.
- Wright, N. J. and Drake, J. J. (2016). Solar-type dynamo behaviour in fully convective stars without a tachocline. *Nature*, 535(7613):526–528.
- Yadav, R. K., Christensen, U. R., Morin, J., Gastine, T., Reiners, A., Poppenhaeger, K., and Wolk, S. J. (2015). Explaining the coexistence of

large-scale and small-scale magnetic fields in fully convective stars. *The Astrophysical Journal Letters*, 813(2):L31.

Yadav, R. K., Christensen, U. R., Wolk, S. J., and Poppenhaeger, K. (2016). Magnetic cycles in a dynamo simulation of fully convective m-star proxima centauri. *The Astrophysical Journal Letters*, 833(2):L28.

Yau, K. and Stephenson, F. (1988). A revised catalogue of far eastern observations of sunspots (165 bc to ad 1918). *Quarterly Journal of the Royal Astronomical Society*, 29:175–197.

Yoshimura, H. (1975). Solar-cycle dynamo wave propagation. , 201:740–748.

Zorotovic, M. and Schreiber, M. R. (2013). Origin of apparent period variations in eclipsing post-common-envelope binaries. , 549:A95.

